
Electronic Thesis and Dissertation Repository

8-18-2021 10:00 AM

Heat Flow in the Core of Ganymede: High Pressure-Temperature Electrical Resistivity Measurements of Solid and Liquid Ag and Fe-S Alloys

Joshua A.H. Littleton, *The University of Western Ontario*

Supervisor: Secco, Richard A., *The University of Western Ontario*

A thesis submitted in partial fulfillment of the requirements for the Doctor of Philosophy degree in Geophysics

© Joshua A.H. Littleton 2021

Follow this and additional works at: <https://ir.lib.uwo.ca/etd>

 Part of the [Condensed Matter Physics Commons](#), and the [Mineral Physics Commons](#)

Recommended Citation

Littleton, Joshua A.H., "Heat Flow in the Core of Ganymede: High Pressure-Temperature Electrical Resistivity Measurements of Solid and Liquid Ag and Fe-S Alloys" (2021). *Electronic Thesis and Dissertation Repository*. 8030.
<https://ir.lib.uwo.ca/etd/8030>

This Dissertation/Thesis is brought to you for free and open access by Scholarship@Western. It has been accepted for inclusion in Electronic Thesis and Dissertation Repository by an authorized administrator of Scholarship@Western. For more information, please contact wlsadmin@uwo.ca.

Abstract

Experimental investigations of materials at high pressures (P) and temperatures (T) provide insight into the properties and behaviours expected within the inaccessible interiors of planetary bodies. Using a four-wire electrical resistance technique, the electrical resistivity (ρ) of *4d* transition metal (Ag) and *3d* transition metal alloys (Fe-S) were measured in the solid and molten states at high P. The thermal conductivity (κ) of these materials is inversely proportional to ρ , as described by the Wiedemann-Franz Law. When applied to planetary cores, κ is an important parameter that regulates heat transport mechanisms and magnetic field production.

A hypothesis of ‘resistivity invariance’ suggested that for pure *d*-band filled metals the magnitude of ρ along the P- and T-dependent melting boundary is constant. This implied that investigations at low P can provide a singular constraint value of ρ and κ at more extreme P and T conditions expected for planetary cores, such as the inner-outer core boundary of Earth which is a solidification boundary. The ρ of silver (Ag) was measured at P up to 5 GPa and T up to ~ 1650 K. The results showed a decrease in ρ along the P-dependent melting boundary, contrary to prediction, and were discussed in terms of increasing energy separation between the Fermi level and *4d*-band as a function of increasing P.

The ρ of solid and molten iron sulfide (FeS) and Fe-FeS were measured at T up to ~ 1750 K and ~ 1350 K, respectively, and P up to 5 GPa. These material compositions are relevant to the sulphur (S)-rich core of Ganymede, with the experimental P and T approximating the conditions at the top, or outer-most portion, of the core. The dipolar magnetic field of Ganymede may be generated by an internal dynamo, implying a molten core that may transport heat by thermal convection. The κ and adiabatic conductive heat flow for molten FeS and Fe-FeS core models of Ganymede were calculated from the measured ρ . The results showed that heat transport by thermal convection is permissible in the core models and may act as an energy source to power a dynamo-produced magnetic field.

Keywords

High Pressure, High Temperature, Electrical Resistivity, Thermal Conductivity, Thermal Convection, Silver, Iron Sulfides, Planetary Cores, Ganymede

Summary for Lay Audience

The cores of planetary bodies are inaccessible to direct measurement of their transport properties because of extreme pressure (P) and temperature (T) conditions and kilometers-thick surrounding rock. However, laboratory experiments at high P and T are capable of replicating interior conditions and the results of these investigations can be used to estimate the properties and behaviours of the cores of these bodies. Electrical resistivity (ρ) and thermal conductivity (κ) are important transport properties to estimate for planetary cores because they affect thermal evolution and production of magnetic fields. For metals and alloys, ρ and κ are related by the Wiedemann-Franz Law, where one transport property can be calculated if the other property is known.

It was hypothesized that ρ of pure metals will have the same value at the melting T at any P. This implied that laboratory measurements at low P and high T could be used to indirectly determine ρ at significantly higher P and T conditions expected for large planetary cores, such as Earth. The ρ of silver (Ag) was measured at P up to 5 GPa and T up to ~1650 K. The results showed a decrease in ρ along the melting boundary, contrary to prediction, and were discussed in terms of effects on electron energy states with increasing P.

Ganymede, a moon of Jupiter, is known to have a magnetic field and is expected to have a core made predominantly of iron (Fe) with some sulphur (S). The ρ of solid and molten iron sulfide (FeS) and Fe-FeS were measured at T up to ~1750 K and ~1350 K, respectively, and P up to 5 GPa. These experimental P and T approximate the conditions at the top, or outermost portion, of the core. The κ and adiabatic conductive heat flow for molten FeS and Fe-FeS core models of Ganymede were calculated from the measured ρ . The results showed that a molten core could transport heat by thermal convection. If the molten core is thermally convecting, this may act as an energy source to power and generate the magnetic field of Ganymede.

Co-Authorship Statement

Main body chapters of this dissertation are comprised of three manuscripts:

1. **Chapter 3:** Littleton, J.A.H., Secco, R.A. and Yong, W. 2018. Decreasing electrical resistivity of silver along the melting boundary up to 5 GPa. *High Pressure Research*. 38(2): 99-106. DOI: 10.1080/08957959.2018.1435786
2. **Chapter 4:** Littleton, J.A.H., Secco, R.A. and Yong, W. 2021. Electrical resistivity of FeS at High Pressures and Temperatures: Implications of Thermal Transport in the Core of Ganymede. *Journal of Geophysical Research: Planets*. 126(5): e2020JE006793. DOI: 10.1029/2020JE006793
3. **Chapter 5:** Littleton, J.A.H., Secco, R.A. and Yong, W. 2021. Thermal Convection in the Core of Ganymede Inferred from Liquid Fe-FeS Electrical Resistivity at High Pressures. *Crystals*. 11(8): 875. DOI: 10.3390/cryst11080875

In each of the preceding works, my contributions included: i) pressure cell design; ii) fabrications of experimental components; iii) conducting high pressure-temperature experiments in a 1000-ton cubic anvil press; iv) post-experiment sample macro-analyses (i.e. sample sectioning and microscopy); v) data analysis and interpretation; and vi) writing and subsequent revisions of manuscripts. Dr. Richard A. Secco's contributions included: i) project concept; ii) funding for instrumentation, materials, and laboratory facilities; iii) discussions related to data interpretation; and iv) feedback and revisions of written manuscripts. Dr. Wenjun Yong's contributions included: i) conducting high pressure-temperature experiments in a 1000-ton cubic anvil press; ii) discussions related to data interpretation; and iii) feedback and revisions of written manuscripts.

Acknowledgments

First and foremost, I would like to express my sincerest gratitude to my supervisor, Dr. Richard A. Secco, whose guidance and support, confidence, and patience have helped me achieve success and mature as a scientist and academic. The feedback and ‘word-smithing’ during writing of manuscripts was remarkable and helped create exceptional prose of high-pressure research. Thank you to my Advisory Committee members, Dr. Sean R. Shieh and Dr. Roberta L. Flemming, for their advice and suggestions. I would like to thank past and present colleagues Dr. Reynold Silber, Dr. Tim Officer, Dr. Innocent Ezenwa and Dr. Wenjun Yong for their insight and support, especially during my earliest of years as an undergraduate research assistant in the lab, and for being fun and interesting people to whom I’ve had the great pleasure of knowing. I want to thank Mr. Jonathan L. Jacobs for his incredible machining expertise that allowed my experimental designs to be more than just pencil sketches on paper.

Thank you to my parents, Henry and Cristine Littleton, for their undying support and understanding through my entire university career. Thank you to my friends, Paul Milliken, Mingzhen Deng, Mauritz van Zyl, Justin Rumney, and Elisa Dong, for their inspiration, motivation, and support during my time as a graduate student.

Table of Contents

Abstract.....	ii
Co-Authorship Statement.....	v
Acknowledgments.....	vi
Table of Contents.....	vii
List of Figures.....	x
List of Tables.....	xiii
List of Appendices.....	xiv
List of Symbols.....	xv
Chapter 1.....	1
1 Introduction.....	1
1.1 General Background.....	1
1.2 Wiedemann-Franz Law: Relating ρ and κ	2
1.3 Stacey’s Electrical Resistivity Hypotheses.....	3
1.4 Importance of Core Thermal Conductivity.....	4
1.5 Ganymede.....	5
1.6 Aim of this Thesis.....	5
1.7 References.....	6
2 Experimental Design and Methodology.....	10
2.1 General Experimental Details.....	10
2.2 References.....	13
Chapter 3.....	14
3 Decreasing Electrical Resistivity of Silver Along the Melting Boundary up to 5 GPa.....	14
3.1 Introduction.....	14
3.2 Experimental Details.....	15

3.3 Results.....	16
3.4 Discussion.....	20
3.5 Conclusion	24
3.6 References.....	25
Chapter 4.....	29
4 Electrical Resistivity of FeS at High Pressures and Temperatures: Implications of Thermal Transport in the Core of Ganymede	29
4.1 Introduction.....	29
4.2 Materials and Methods.....	36
4.3 Results.....	39
4.4 Discussion	45
4.5 Conclusion	54
4.6 References.....	54
Chapter 5.....	61
5 Thermal Convection in the Core of Ganymede Inferred from Liquid Eutectic Fe-FeS Electrical Resistivity at High Pressures	66
5.1 Introduction.....	66
5.2 Materials and Methods.....	67
5.3 Results and Discussion	68
5.4 Conclusion	78
5.5 References.....	78
Chapter 6.....	79
6 Conclusion	84
6.1 Silver.....	84
6.2 Iron Sulphides.....	85
6.3 Suggested Future Works.....	85
6.4 References.....	87

Appendices.....	89
Copyright Permission.....	119
Curriculum Vitae	127

List of Figures

Figure 2.1: Photo of the 1000-ton cubic multi-anvil press	11
Figure 2.2: A fully assembled three-section cubic P cell resting on an axial anvil	12
Figure 3.1: Cross-sectional view of the Ag wire sample recovered from an experiment.....	17
Figure 3.2: Measured electrical resistivity of Ag at pressures of 2-5 GPa	18
Figure 3.3: The natural logarithm of electrical resistivity along the liquid side of the melting boundary	19
Figure 3.4: Melting temperature of Ag as a function of pressure	21
Figure 3.5: Electronic component of thermal conductivity of Ag at pressure 2-5 GPa.....	22
Figure 4.1: Illustration of the cross-section of the cubic pressure cell	37
Figure 4.2: Measured electrical resistivity of FeS at pressures of 2 – 5 GPa	40
Figure 4.3: Cross-sectional view of the post-experiment 4 GPa pressure cell	44
Figure 4.4: Measured electrical resistivity of FeS from this study are compared	46
Figure 4.5: Calculated adiabatic heat flow at the core-mantle boundary	52
Figure 5.1: Measured electrical resistivity of Fe-FeS at pressures of 2-5 GPa.....	70
Figure 5.2: Cross-sectional view of the post-experiment 4 GPa pressure cell	72
Figure 5.3: Experimentally determined eutectic temperatures of the Fe-FeS system	74
Figure 5.4: Calculated adiabatic heat flow at the core-mantle boundary	76
Figure A.1: Back-scattered electron image of the post-experiment 2 GPa pressure cell	92
Figure A.2: Back-scattered electron image of the post-experiment 3 GPa pressure cell	92
Figure A.3: Back-scattered electron image of the post-experiment 5 GPa pressure cell	93

Figure A.4: Electrical Resistivity Interpolation of 5 GPa Data: 1600-1700 K.....	94
Figure B.1: Electrical Resistivity Interpolation of 5 GPa Data: 1250-1450 K.....	95
Figure C.1: Cross-section of an assembled cube using the first cell design.....	96
Figure C.2: Post-experiment view of a pressure cell.....	97
Figure C.3: Cross-section of a recovered 4 GPa experiment (~1600 K).....	98
Figure C.4: Electrical resistivity of Ag as a function of temperature at pressures of 1, 2, 3 and 4 GPa utilizing the first cubic cell design.....	99
Figure C.5: Plot of melting temperatures of Ag as a function of pressure using the first cubic cell design.....	100
Figure C.6: Cross-section of an assembled cube using the second cell design.....	101
Figure C.7: Cross-section of a recovered 2 GPa experiment (~1383 K).....	102
Figure C.8: Electrical resistivity of Ag as a function of temperature at pressures of 2, 3, 4 and 5 GPa utilizing the second cubic cell design.....	103
Figure C.9: Plot of melting temperatures of Ag as a function of pressure using the second cubic cell design.....	104
Figure C.10: Image of recovered experiments prepared in epoxy disks for EPMA.....	105
Figure C.11: Backscattered electron image of a recovered experiment from 4 GPa.....	106
Figure C.12: Second backscattered electron image of a recovered experiment from 4 GPa.....	107
Figure C.13: Illustration of the cross-section of the first cubic pressure cell used in iron sulphide (FeS) experiments.....	108
Figure C.14: Cross-section of a sample and disks recovered from a 2 GPa experiment.....	109
Figure C.15: Electrical resistivity of FeS as a function of temperature at 2 GPa utilizing the cell design.....	110

Figure C.16: Comparison of the resistivity of FeS at 2 GPa in Fig. C.14 to Pommier (2018)	111
Figure C.17: Cross-section of a recovered 2 GPa experiment (~1671 K) using a modified cell design	112
Figure C.18: Comparison of the electrical resistivity of FeS at 2 GPa (~1671 K)	113
Figure C.19: Backscattered electron images of the recovered experiment.....	114
Figure C.20: Back-scattered electron image of the post-experiment 2 GPa (~1671 K)	115
Figure C.21: Illustration of the cross-section of a multi-anvil octahedral pressure cell used for FeS experiments.....	116
Figure C.22: Cross-section of a recovered 4 GPa experiment (~1772 K)	117
Figure C.23: Electrical resistivity of FeS using the multi-anvil cell design	118

List of Tables

Table 5.1: Values of targeted eutectic Fe-FeS sample compositions and post-experiment analysis results of sample compositions for each pressure in this study	68
---	----

List of Appendices

Appendix A: Supporting Information for Chapter 3.....	89
Appendix B: Supporting Information for Chapter 4.....	95
Appendix C: Selected Prior Cell Designs and Unsuccessful Results	96

List of Symbols

A	Sample cross-sectional area
CMB	Core-Mantle Boundary
c_p	Isobaric heat capacity
D	Sample diameter
E_{Fd}	Energy gap between Fermi level and upper-most d -band electrons
g	Gravitational acceleration
I	Electrical current
L	Lorenz number
L_0	Sommerfeld value of Lorenz number
l	Sample length
P	Pressure
Q_a	Adiabatic (conductive) heat flow
r	Core radius
R	Electrical resistance
$s \rightarrow d$	Transition of s -electron to d -state
$s \rightarrow s$	Transition of s -electron to s -state
T	Temperature
T_D	Debye Temperature
T_M	Melting boundary temperature

V	Voltage
α	Thermal Expansion
κ	Thermal conductivity
κ_e	Electronic component of thermal conductivity
κ_{ph}	Phonon component of thermal conductivity
ρ	Electrical resistivity
ρ_L	Liquid state electrical resistivity

Chapter 1

1 Introduction

In science one tries to tell people, in such a way as to be understood by everyone, something that no one ever knew before. But in the case of poetry, it's the exact opposite.

- Paul Dirac

1.1 General Background

The majority of the interior of terrestrial bodies, including the core, are inaccessible to direct measurements of physical properties. Laboratory methods can replicate the high pressure (P) and temperature (T) conditions of the interior while also allowing experimental investigations of physical properties. These experimental results provide insight into how the interior behaves and may provide trends expected for interiors with more or less extreme P-T conditions. The physical property investigated in this work is electrical resistivity (ρ). For metallic materials, which generally constitute terrestrial cores, ρ is related to thermal conductivity (κ). Both ρ and κ are important parameters to investigate since they influence the thermal state and magnetic field generation (i.e. dynamo process) of terrestrial cores. As core conditions become more extreme (i.e. increasing P and T with depth), the experimental challenges of direct measurements of ρ and κ also increase. For this reason, reports of these properties of relevant core materials at Earth-like conditions (>125 GPa; >2500 K) are scarce; however, experimental methodology and instrumentation are improving and results are reported with slightly more frequency in recent time. The physical conditions this work focused on is the low-end (2 – 5 GPa) of the scale of planetary interior P and a relatively large range of T from ~ 293 K up to ~ 1800 K. Experimental results of the low-end P provides two valuable contributions: i) anchor points for higher P experiments and theoretical frameworks; and ii) information directly relevant to the cores of smaller terrestrial bodies, such as Jupiter's moon Ganymede.

1.2 Wiedemann-Franz Law: Relating ρ and κ

Understanding the relationship between ρ and κ in the context of the free electron model requires numerous derivations and introduction of many additional concepts in condensed matter physics (e.g. Omar, 1993). For brevity, the following details a simplified qualitative description of the Wiedemann-Franz Law (WFL).

In solids, heat is transferred or carried by lattice vibrations (phonons) and electrons. The contribution by each heat carrier is dependent on the material. Thus, κ can be expressed as the sum of the two contributions, as shown below:

$$\kappa = \kappa_{\text{ph}} + \kappa_e \quad (1.1)$$

where κ_{ph} is the phonon contribution and κ_e is the electronic contribution to the thermal conductivity. In good conductors, such as metals and metallic compounds/alloys, there are a significant number of conducting electrons (electrons near the Fermi surface; free electrons) and thus are the dominant carriers. In metals, κ_e is often more than a magnitude larger than κ_{ph} (Klemens and Williams, 1986) and, as a result, it is reasonable to assume that $\kappa \approx \kappa_e$. As a metal is heated, the free electrons absorb thermal energy and are excited. The net diffusive motion of the electronic heat carriers is towards a cooler location. Since electrons are intrinsically negatively charged, heat and charge are transferred simultaneously. This results in a non-zero net electric current in the direction opposite of the electrons and establishes a direct connection to ρ . It was realized in the late 19th century that the product value of $\kappa \cdot \rho$ was approximately the same value for different metals, as well as for different metals at different T (Franz and Wiedemann, 1853). These observations when combined with a free electron model gave rise to the WFL, as follows:

$$\frac{LT}{\rho} = \kappa \approx \kappa_e \quad (1.2)$$

where L is the Lorenz number and has a theoretical value, called the Sommerfeld value L_0 , of $2.44(5) \cdot 10^{-8} \text{ W} \cdot \Omega \cdot \text{K}^{-2}$ (Omar, 1993). Obtaining values of κ by direct measurement at high P and T is challenging as it requires a well-controlled temperature gradient to cause heat-carrying electrons to flow. Since the materials investigated in this work are

metallic, we exploit the WFL as shown in Eqn. (1.2) to determine the dominant component κ_e from the experimental measurements of ρ as a function of T at high P .

1.3 Stacey's Electrical Resistivity Hypotheses

Stacey and Anderson (2001) derived a semi-theoretical expression using a thermodynamical framework based on Debye frequencies of lattice vibrations that indicated that along the P -dependent melting boundary of a pure metal the ρ is constant. If shown to be valid, this hypothesis would offer a highly significant and practical approach for laboratory studies to assess ρ at core conditions. Consider a terrestrial core that consists of a solid inner core and liquid outer core, such as Earth. For simplicity, we will assume the core is entirely Fe. Since the boundary of the inner and outer core is a melting (equivalently, and in reality, a solidification) boundary of Fe, laboratory measurements of ρ of Fe under any P would serve as a proxy for ρ at the melting boundary under core P and T . In other words, experimental investigations of ρ at the melting boundary confined to the low-end of the high P scale (e.g., 2 GPa) would provide useful information of ρ at the melting boundary at much higher P conditions. Moreover, if the proxy value of ρ and T of the core melting boundary are known, then Eqn. (1.2) can be exploited to obtain a corresponding value of κ . Since terrestrial cores are generally suggested to contain other elements, the hypothesis reduces understanding core resistivity effects due to impurities which are expected to increase ρ and decrease κ . In this example, the proxy values of ρ and κ for pure Fe at Earth's inner-outer core/melting boundary would represent a lower- and upper-bound anchor points, respectively. Shortly thereafter, Stacey and Loper (2007) suggested that invariance of ρ along the melting boundary should only be observed for pure metals that have filled d -bands with only electrons belonging to the energetically upper-most s -band participating in electrical conduction. This revision was due to recognition of innate differences of electronic configuration and band structures among metals and, in particular, to account for metals that have an unfilled or partially filled d -band. The significance of this, which was briefly noted by Stacey and Anderson (2001) but not employed in the initial derivation, is that empty electronic states in the d -band may be occupied by conducting s -electrons via $s \rightarrow d$ scattering (Mott, 1964). The effect of this scattering mechanism increases ρ since the s -

electrons scattered into d -states are less mobile due to experiencing a higher d -state effective mass.

1.4 Importance of Core Thermal Conductivity

Heat is continually transported through cores of terrestrial bodies outward toward the surface of the body. The quantity of heat transported is dependent on the composition and physical states of the core. For example, solid Fe has a different κ than liquid Fe or solid Fe alloyed with Si (e.g. Silber et al., 2018, 2019; Yong et al., 2019; Berrada et al., 2020). Surrounding the core is the mantle, a silicate shell that continually accepts or removes heat from the core. The κ of a silicate is typically only 10-20% of the κ of Fe (Hofmeister, 1999; Goncharov et al., 2009). Similarly, the quantity of heat removed by the mantle at the core-mantle boundary (CMB) is dependent on composition and physical states of the mantle. The heat removed from the core at the CMB controls the rate of cooling and on-going processes of the core (Buffett, 2007) and has similar effects on the mantle (Olson, 2016).

All cores transfer heat by thermal conduction, which is directly proportional to κ . However, if a core is entirely liquid or contains a liquid component, heat may also be transferred by thermal convection. If thermal convection of a predominantly Fe liquid core occurs, it is possible to generate a magnetic field via dynamo action, such as Earth's geodynamo. The amount of heat extracted on the mantle-side of the CMB must be supplied by the core either entirely by conduction in the core if κ is large enough, or by conduction and thermal convection in the core. If the heat removed from the core through the CMB is greater than the amount of heat that can be conducted to the top of the core just below the CMB, thermal convection is required as an additional process to meet the additional heat extraction by the mantle. Otherwise, if thermal conduction alone can satisfy the heat transfer requirement of the core, thermal convection will not occur (Buffett, 2007). Thus, it is crucial to obtain values of κ of molten core materials – either by direct measurement of κ , direct measurements of ρ and use of Eqn. (1.2), or via Stacey's hypothesis – to provide information on conducted heat so that comparison can be made to estimates of heat flow out of the core through the CMB. This comparison will determine the style(s) of thermal transport occurring within the core.

There are additional ways in which a liquid core can undergo convection. Since the core is continually cooling, portions of the liquid component will eventually solidify. Provided it does not occur at the top of the core, solidification or precipitation of these core constituents is exothermic and could thermally-drive convection. Additionally, a density contrast may exist between the solid and liquid components. The contrast would initiate a chemical- or buoyancy-driven style of convection as the less dense material moves outwards and the denser material sinks inwards. Buoyancy- and thermally-driven convection may occur in tandem in cores of terrestrial bodies and understanding them is dependent on knowing values of κ of core constituents (Buffett, 2003, 2007; Christensen, 2015; Rückriemen et al., 2015; 2018).

1.5 Ganymede

Ganymede is the largest and densest satellite in the solar system with an average radius of ~ 2632 km and density of 1940 kg/m^3 (Spohn, 2015). The satellite is considered to have a fully differentiated interior, with a dense metallic core immediately surrounded by a rocky mantle that is overlain by a subsurface ocean between layers of ice (Hussmann et al., 2015). Spectral analyses of the surface of Ganymede suggest the presence of a variety of sulphur (S) bearing molecules, such as sulphur dioxide, hydrogen sulphate, magnesium sulphate, and sodium sulphate (McCord et al., 1998; Showman and Malhotra, 1999; McCord et al., 2001). Sulphur has also been suggested to be a prominent impurity element in the Fe core, and is compatible with internal structure calculations based on moment of inertia observations from the Galileo spacecraft (Anderson et al., 1996; Sohl et al., 2002). Similar to Earth, Ganymede too has a dipolar magnetic field and it is thought to be likely powered by thermally- and buoyancy-driven convection of a liquid or partially molten core (Connery, 2007; Busse and Simitev, 2015).

1.6 Aim of this Thesis

The overarching goal of this thesis was to constrain better the transport properties of the cores of small terrestrial-like planetary bodies, such as the S-rich metallic core of Ganymede with a particular focus on heat transport. An experimental approach of measuring the electrical resistivity at high pressures and into the liquid state was used.

There were two main objectives of this thesis. The first objective was to test the validity of the proposed invariance of ρ at the melting boundary for pure silver (Ag), a transition metal with filled d -bands. According to either hypothesis (Stacey and Anderson, 2001; Stacey and Loper, 2007), this invariance behaviour is expected to be observed for Ag. By measuring ρ directly in both solid and liquid states between 2-5 GPa, the value of ρ along the P-dependent melting boundary could be observed and compared to the expectation of invariance.

The second objective was to determine whether thermally-driven convection is possible in a liquid S-bearing Fe-rich core of Ganymede, which can act as a power source for dynamo action. Two possible core compositions were studied: i) FeS core; and ii) eutectic Fe-FeS core. Since our knowledge of ρ of Fe-S is very limited based on scarce data, ρ of FeS and Fe-FeS was measured directly in both the solid and liquid states between 2-5 GPa. Using the WFL, κ can be calculated from the measured electrical resistivity and used to determine the amount of heat carried by conduction to the CMB on the core-side. These values may be compared to estimates of heat extracted from the core on the mantle-side of the CMB.

1.7 References

- Anderson, J.D., Lau, E.L., Sjogren, W.L., Schubert, G. and Moore, W.B. 1996. Gravitational constraints on the internal structure of Ganymede. *Nature*. 384(6609): 541-543. DOI: 10.1038/384541a0
- Berrada, M., Secco, R.A., Yong, W. and Littleton, J.A.H. 2020. Electrical resistivity measurements of Fe-Si with implications for the early lunar dynamo. *Journal of Geophysical Research: Planets*. 125(7): e2020JE006380. DOI: 10.1029/2020JE006380
- Buffett, B. 2003. The thermal state of Earth's core. *Science*, 299(5613): 1675-1677. DOI: 10.1126/science.1081518
- Buffett, B. 2007. Core-mantle interactions. *In* *Treatise on Geophysics*, Vol. 8. *Edited by* Peter Olson and Gerald Schubert. Elsevier Ltd., Waltham, Mass. pp. 345-358.

Busse, F.H. and Simitev, R.D. 2015. Planetary Dynamos. *In* Treatise on Geophysics, Vol. 10., 2nd Ed. *Edited by* Gerald Schubert. Elsevier Ltd., Waltham, Mass. pp. 239-254.

Christensen, U.R. 2015. Iron snow dynamo models for Ganymede. *Icarus*. 247: 248-259. DOI: 10.1016/j.icarus.2014.10.024

Connerney, J.E.P. 2007. Planetary Magnetism. *In* Treatise on Geophysics, Vol. 10. Edited by Tilman Spohn and Gerald Schubert. Elsevier Ltd., Waltham, Mass. pp. 243-280.

Franz, R. and Wiedemann, G. 1853. Ueber die Wärme-Leitungsfähigkeit der Metalle. *Annalen der Physik*. 165(8): 497-531. DOI: 10.1002/andp.18531650802

Goncharov, A.F., Beck, P., Struzhkin, V.V., Haugen, B.D. and Jacobsen, S.D. 2009. Thermal conductivity of lower-mantle minerals. *Physics of the Earth and Planetary Interiors*. 174(1-4): 24-32. DOI: 10.1016/j.pepi.2008.07.033

Hofmeister, A.M. 1999. Mantle values of thermal conductivity and the geotherm from phonon lifetimes. *Science*. 283(5408): 1699-1706. DOI: 10.1126/science.283.5408.1699

Hussmann, H., Sotin, C. and Lunine, J.I. 2015. Interiors and Evolution of Icy Satellites. *In* Treatise on Geophysics, Vol. 10., 2nd Ed. *Edited by* Gerald Schubert. Elsevier Ltd., Waltham, Mass. pp. 605-635.

Klemens, P.G. and Williams, R.K. 1986. Thermal conductivity of metals and alloys. *International Metals Reviews*. 31(5): 197-215. DOI: 10.1179/imtr.1986.31.1.197

McCord, T.B., Hansen, G.B., Clark, R.N., Martin, P.D., Hibbitts, C.A., Fanale, F.P., Granahan, J.C., Segura, M., Matson, D.L., Johnson, T.V., Carlson, R.W., Smythe, W.D. and Danielson, G.E. 1998. Non-water-ice constituents in the surface material of the icy Galilean satellites from the Galileo near-infrared mapping spectrometer investigation. *Journal of Geophysical Research: Planets*. 103(E4): 8603-8626. DOI: 10.1029/98JE00788

McCord, T.B., Hansen, G.B. and Hibbitts, C.A. 2001. Hydrated salt minerals on Ganymede's surface: Evidence of an ocean below. *Science*. 292(5521): 1523-1525. DOI: 10.1126/science.1059916

Mott, N.F. 1964. Electrons in transition metals. *Advances in Physics*. 13(51): 325-422. DOI: 10.1080/00018736400101041

Olson, P. 2016. Mantle control of the geodynamo: Consequences of top-down regulation. *Geochemistry, Geophysics, Geosystems*. 17(5): 1935-1956. DOI: 10.1002/2016GC006334

Omar, M. 1993. *Elementary Solid State Physics: Principles and Applications*. Edited by D. Lazarus. Addison-Wesley Publishing Company, Inc., Boston, M.A.

Rückriemen, T., Breuer, D. and Spohn, T. 2015. The Fe snow regime in Ganymede's core: A deep-seated dynamo below a stable snow zone. *Journal of Geophysical Research: Planets*. 120(6): 1095-1118. DOI: 10.1002/2014JE004781

Rückriemen, T., Breuer, D. and Spohn, T. 2018. Top-down freezing in a Fe-FeS core and Ganymede's present-day magnetic field. *Icarus*. 307: 172-196. DOI: 10.1016/j.icarus.2018.02.021

Showman, A.P. and Malhotra, R. 1999. The Galilean Satellites. *Science*. 286(5437): 77-84. DOI: 10.1126/science.286.5437.77

Silber, R.E., Secco, R.A., Yong, W. and Littleton, J.A.H. 2018. Electrical resistivity of liquid Fe to 12 GPa: Implications for heat flow in core of terrestrial bodies. *Scientific Reports*. 8(1): 1-9. DOI: 10.1038/s41598-018-28921-w

Silber, R.E., Secco, R.A., Yong, W. and Littleton, J.A.H. 2019. Heat flow in Earth's core from invariant electrical resistivity of Fe-Si on the melting boundary to 9 GPa: Do light elements matter?. *Journal of Geophysical Research: Solid Earth*. 124(6): 5521-5543. DOI: 10.1029/2019JB017375

- Sohl, F., Spohn, T., Breuer, D. and Nagel, K. 2002. Implications from Galileo observations on the interior structure and chemistry of the Galilean satellites. *Icarus*. 157(1): 104-119. DOI: 10.1006/icar.2002.6828
- Spohn, R. 2015. Physics of terrestrial planets and moons: An introduction and overview. *In Treatise on Geophysics, Vol. 10., 2nd Ed. Edited by Gerald Schubert. Elsevier Ltd., Waltham, Mass. pp. 1-22.*
- Stacey, F.D. and Anderson, O.L. 2001. Electrical and thermal conductivities of Fe-Ni-Si alloy under core conditions. *Physics of the Earth and Planetary Interior*. 124(3): 153-162. DOI: 10.1016/S0031-9201(01)00186-8
- Stacey, F.D. and Loper, D.E. 2007. A revised estimate of the conductivity of iron alloy at high pressure and implications for the core energy balance. *Physics of the Earth and Planetary Interior*. 161(1): 13-18. DOI: 10.1016/j.pepi.2006.12.001
- Yong, W., Secco, R.A., Littleton, J.A.H. and Silber, R.E. 2019. The Iron Invariance: Implications for Thermal Convection in Earth's Core. *Geophysical Research Letters*. 46(20): 11065-11070. DOI: 10.1029/2019GL084485

Chapter 2

2 Experimental Design and Methodology

No amount of experimentation can ever prove me right; a single experiment can prove me wrong.

- Albert Einstein

2.1 General Experimental Details

Only general details common to all of the experimental works of this thesis will be discussed in this section. Specifications of experimental methods can be found in the subsequent Chapters 3-5, as well as the Appendices.

As shown in Figure 2.1a, a 1000-ton cubic anvil press was used to achieve quasi-hydrostatic pressure by application of an approximately equal magnitude of force directed inwards to the center of the sample-containing medium along each face. The thrusting of the anvils to the center generates high pressure in that region. There are six identical anvils along three opposite directions perpendicular to each other. The shape of the anvils is that of a frustum on the top of a cylinder. Each anvil is backed by a hydraulic ram that is fixed to a steel frame along the three principle directions. The rams move independently and the motion is regulated by oil pressure in a pumping system. The anvils are made of fine-grained tungsten-carbide with 6 wt.% cobalt, which is used as a binder. Pyrophyllite was used as the material for the cubic pressure-transmitting medium. When being compressed, the pyrophyllite flows and forms a gasket between the anvils (Figure 2.2b).

The cubic pressure cell was sectioned into three layers that when stacked form a 3.175 cm edge length cube (Fig. 2.2a). The middle section contained two thermocouples (TC) in contact at opposing ends of a wire or powder sample, establishing a four-wire resistance technique, enclosed in boron nitride (BN). The voltage switch operated two modes: i) temperature mode; and ii) resistance mode. In temperature mode,

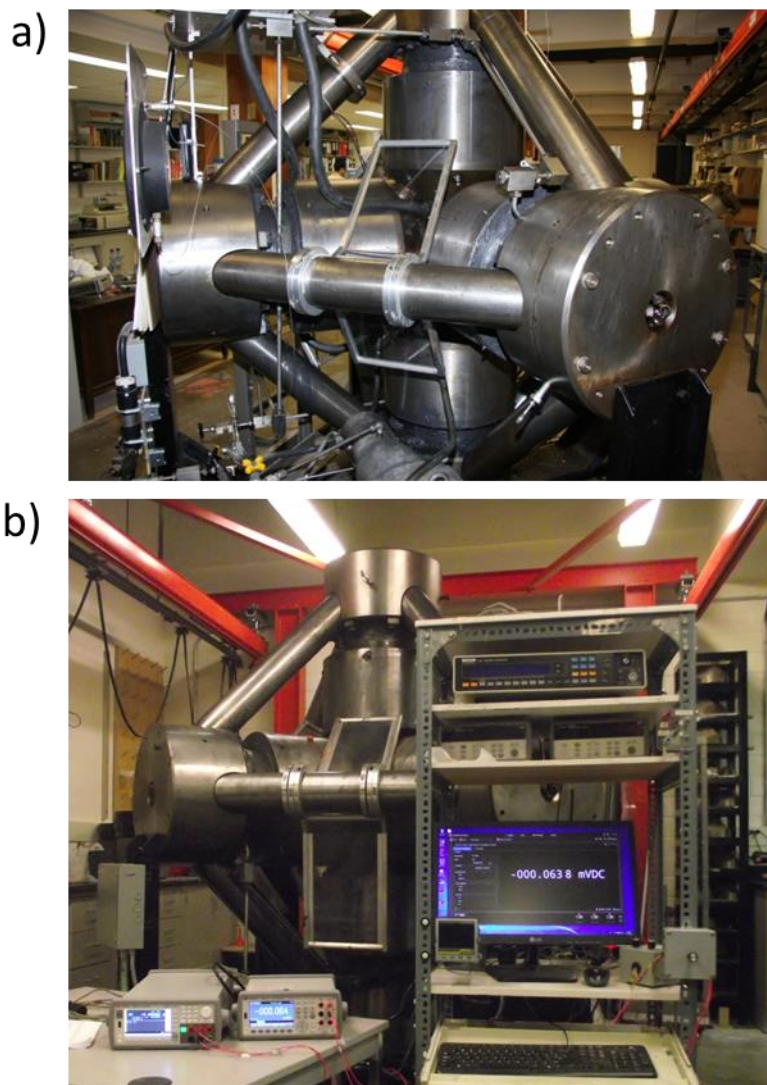


Figure 2.1: (a) Photo of the 1000-ton cubic multi-anvil press. 4 of the 6 hydraulic rams are shown. A portion of the pumping system appears at the bottom left. (b) On the table is a Keysight B2961A Power Source (left box) to provide a constant direct current and Keysight 34470A Multi-meter (right box) to measure DC voltages and computer to take meter readings. Attached to the left frame of the computer desk is a Eurotherm temperature controller and to the right frame is a voltage (Resistance/Temperature modes) and current polarity switch.

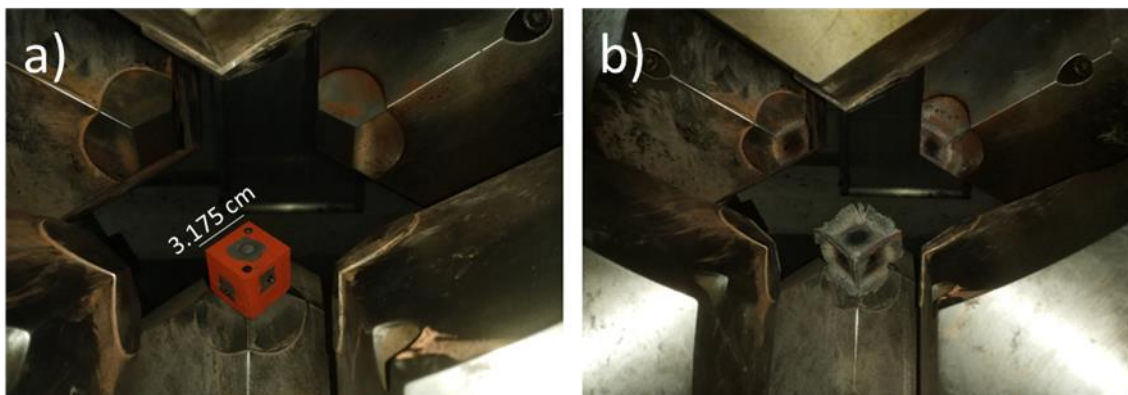


Figure 2.2: (a) A fully assembled three-section cubic P cell resting on an axial anvil of a 1000-ton cubic press. The bright red coating is iron (III) oxide. The top square face perpendicular to the direction of the upper axial anvil displays one end of the graphite furnace ring and two smaller non-coated circles. The latter are faces of pyrophyllite pin rods that are inserted through all three component sections of the cube to maintain alignment during compression. Within the non-coated square regions of the two shown lateral faces are small circular copper foil disks that enhance contact between the extruding thermocouple wire arms and the anvils. (b) The same cubic pressure cell after an experiment was conducted. During compression, the edges of the pyrophyllite cubic pressure cell flows into the unoccupied space between the anvils, creating wing-like gaskets.

measurements of the electromotive force across the thermocouples were taken to determine sample T. In resistance mode, measurements of the voltage across the sample between the thermocouples were taken. A Keysight B2961A power source (Fig. 2.1b) provided a constant current (I) through one pair of opposing TC arms while a Keysight 34470A data acquisition meter operating at 20 Hz with 1 μ V resolution measured the sample voltage (V). A current polarity switch was used such that each sample voltage measurement involved averaging a minimum of 20 V measurements for current passing in two opposing directions at any given T. A high alternating current was passed through a segmented graphite cylinder (one cylindrical segment per cubic cell section) to generate high T. A cylindrical annulus of zirconia was assembled around the central graphite cylinder and two zirconia disks were placed adjacent to the ends of the BN for thermal

insulation. The electrical resistance, R , was calculated using Ohm's law (Eqn. 2.1; middle equality). Pouillet's law (Eqn. 2.1; right-most equality) relates the geometry and electrical resistivity of a resistive or conductive material to the resistance as expressed in the following:

$$R = \frac{V}{I} = \rho \frac{l}{A} \quad (2.1)$$

where ρ is electrical resistivity, A is uniform cross-section of the material, and l is length of the material. Once recovered from the cubic press and ground down into a cross section, the post-experimental sample length and diameter were measured using a Nikon SMZ800 microscope under 40 \times magnification. Because the materials contributing to the resistance are cylinders, the cross-sectional area A is the area of a circle. With R , l , and A determined, Eqn. 2.1 was rearranged to solve for ρ .

Errors on ρ (and κ) were assessed from the measured post-experimental sample geometries and averaged voltage measurements using standard error propagation methods (e.g., Bevington and Robinson, 2003). Voltage measurements of the samples were conducted up to P of 5 GPa and T up to \sim 1800 K. Chemical compositions of the recovered and sectioned samples were analyzed via electron microprobe analysis (EMPA) using a JEOL JXA-8530F field-emission microprobe operating with a 20 kV accelerating voltage, a 50 nA probe current, and a variable 100 nm – 10 μ m spot-size beam.

2.2 References

Bevington, P.R. and Robinson, D.K. 2003. *Data Reduction and Error Analysis for the Physical Sciences*, 3rd Ed. McGraw-Hill Education, New York, N.Y.

Chapter 3

3 Decreasing Electrical Resistivity of Silver Along the Melting Boundary up to 5 GPa

There are many hypotheses in science that are wrong. That's perfectly alright; it's the aperture to finding out what's right. Science is a self-correcting process.

- Carl Sagan

A version of this chapter has been published as:

Littleton, J.A.H., Secco, R.A. and Yong, W. 2018. Decreasing electrical resistivity of silver along the melting boundary up to 5 GPa. *High Pressure Research*. 38(2): 99-106. DOI: 10.1080/08957959.2018.1435786

3.1 Introduction

Stacey and Anderson (2001) derived a semi-theoretical expression which indicated that along the pressure- and temperature-dependent melting boundary of a pure metal, the electrical resistivity is constant. If shown to be correct, this could be a practical approach for laboratory studies since the electrical resistivity at the melting boundary under any achievable pressure would serve as a proxy for the resistivity along the melting boundary under any high pressure and associated melting temperature. In an area of application where pressure and temperature conditions present obstacles to resistivity measurements, and especially in planetary core physics, the simple expression below derived by Stacey and Anderson (2001), could prove very useful:

$$\left(\frac{\partial \ln \rho}{\partial P}\right)_{T_M} = 0 \quad (3.1)$$

where ρ is electrical resistivity, P is pressure, and T_M is melting temperature.

Stacey and Loper (2007) recognized the electronic configuration and the related electron band structure were not appropriately accounted for by Stacey and Anderson (2001) and expressed concern about the significance of the innate difference in those two properties

among other metals. After revising the previous work, Stacey and Loper (2007) concluded that only for simple metals (i.e. metals with conduction electron states of the same type, e.g. *s*-electrons) should the resistivity remain constant along the melting boundary. The majority of transition metals, such as iron, have partially filled *d*-bands. Empty electron states within the *d*-band allow for the occupancy of conducting *s*-electrons via *s*→*d* scattering. The scattered *s*-electrons into these states experience a higher effective mass and consequently are less mobile leading to higher electrical resistivity.

The purpose of this work is to test the validity of Stacey's hypothesis against silver (Ag), a simple metal following the definition of Stacey and Loper (2007). Resistivity measurements of Ag are known at 1 atm up to temperatures of ~1600 K (Matula, 1979).

3.2 Experimental Details

All experiments were conducted in a 1000-ton cubic anvil press described by Secco (1995). A cubic pressure cell design implementing a four-wire resistance measurement technique was used. Resistive heating via passage of a high alternating current through a cylindrical annulus of graphite generated high-temperatures in the enclosed Ag wire sample encapsulated in boron nitride (BN). A cylindrical sleeve and two disks of zirconia effectively confined and thermally insulated the Ag wire sample and the central portion of the graphite heater. A more comprehensive description and detailed figure of the cubic cell design and experimental methodology is given by Ezenwa and Secco (2017).

The initial dimensions of the Ag wire sample (99.9985%, Alfa Aesar) were 0.51 mm in diameter and 1.78 mm in length. In direct contact with the ends of the Ag wire were two Type C (W5%Re-W26%Re) thermocouple junctions (i.e. four wires) to pass current and measure voltage across the sample, in addition to measure temperature via thermal voltage. A Keysight B2961 power source provided a constant direct current of 0.2 A and voltages were measured using a Keysight 34470A data acquisition meter operating at 20 Hz with 1 μ V resolution. A current polarity switch was used so that each four-wire resistance measurement at a particular temperature involved averaging the voltages for current passing in two opposing directions. Post-experiment cross-sectional length and

diameter of the recovered samples after sectioning and grinding were measured using a Nikon SMZ2800 microscope. Errors on resistivity were assessed from sample geometry measurements and averaged voltage measurements using standard error propagation methods. JEOL JXA-8530F field-emission electron microprobe, operating with a 20 kV accelerating voltage, 50 nA probe current, and 100 nm spot-size beam, was used to determine the composition of the recovered sample and thermocouples.

3.3 Results

Successful containment of the liquid sample was important for sample geometry preservation so that the recovered sample could be approximated as having maintained the shape of a cylinder as shown in Figure 3.1A. Averages of several cross-sectional measurements of length and diameter of the recovered Ag sample, as illustrated in Figure 3.1A, were used to calculate the electrical resistivity. As displayed in Figure 3.1B, microprobe analyses after high P,T exposure showed no contamination of the Ag sample by thermocouple materials, and vice versa, as well as no contamination by the encapsulating BN. This is consistent with expected behavior of the Ag-W and Ag-Re binary systems in which no solid phase compounds are known and liquid Ag has no known chemical interaction with solid W and Re (Vijayakumar et al., 1988; Karakaya and Thompson, 1988; Predel, 2006; SGTE, 2007).

The electrical resistivity of Ag at pressures of 2-5 GPa as a function of temperature up to ~300 K above the observed melting temperatures is shown in Figure 3.2. The electrical resistivity of Ag at 1 atm from a collection of many previous studies as reported in Matula (1979) is also shown for comparison. As expected, increasing pressure was observed to decrease the electrical resistivity in the solid and liquid phases, while increasing temperature was observed to increase the electrical resistivity in the solid and liquid phases. These are well known effects on resistivity of metals due to pressure and temperature (Secco and Schloessin, 1989; Ezenwa and Secco, 2017). The discontinuity in resistivity at high-temperature indicates the phase change from solid to liquid Ag. Figure 3.3 shows the natural logarithm of resistivity at the melting boundary as a function of pressure, from which the slope of the best-fitted line or the T-coefficient of resistivity along the melting boundary, $(\partial \ln \rho / \partial P)_{T_M}$, is $-0.031 \pm 0.003 \text{ GPa}^{-1}$.

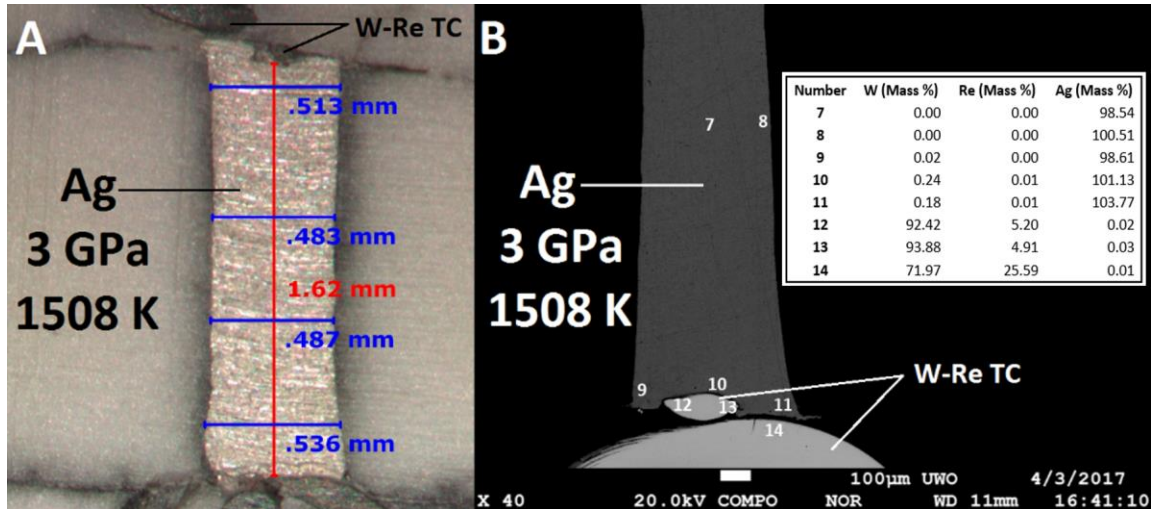


Figure 3.1: (A) Cross-sectional view of the Ag wire sample recovered from an experiment at 3 GPa and 1508 K. Type C (W5%Re-W26%Re) thermocouples (TC) were used to measure temperature. TC junctions were in direct contact with the end of the Ag wire to act also as electrodes and measure the voltage drop across the sample. Example lengths and diameter measurements are shown at several locations along the Ag wire sample. Apparent surface lineations of the Ag wire sample and surrounding BN are due to sanding and lighting. (B) Back-scattered electron image of the sample from (A). Tabulated electron microprobe results of eight locations correspond to labeled sites on the image.

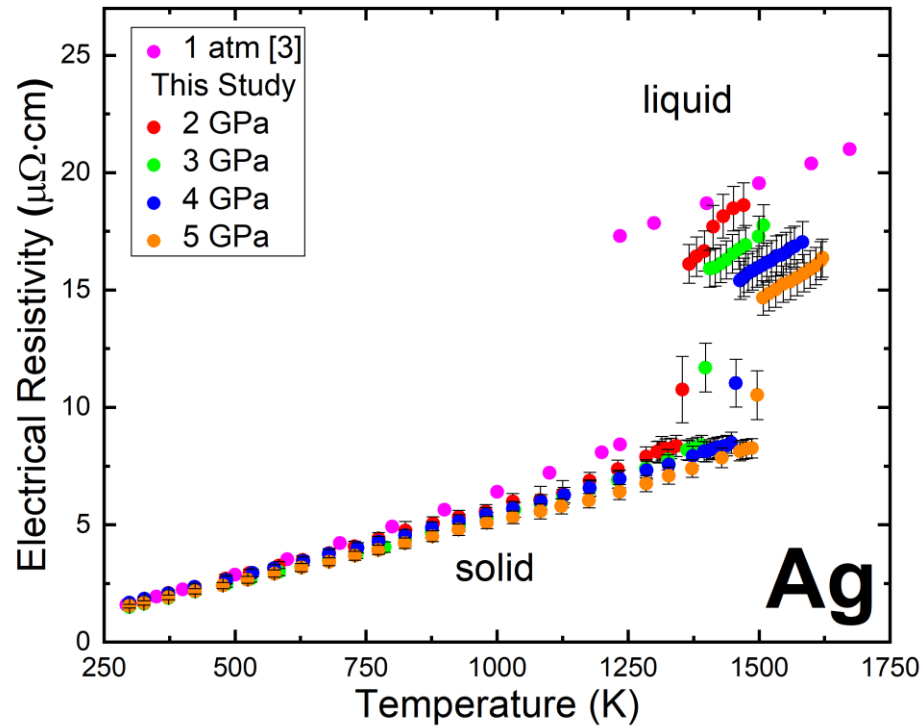


Figure 3.2: Measured electrical resistivity of Ag at pressures of 2-5 GPa as a function of temperature. For comparison, 1 atm data (Matula, 1979 as [3]) are shown.

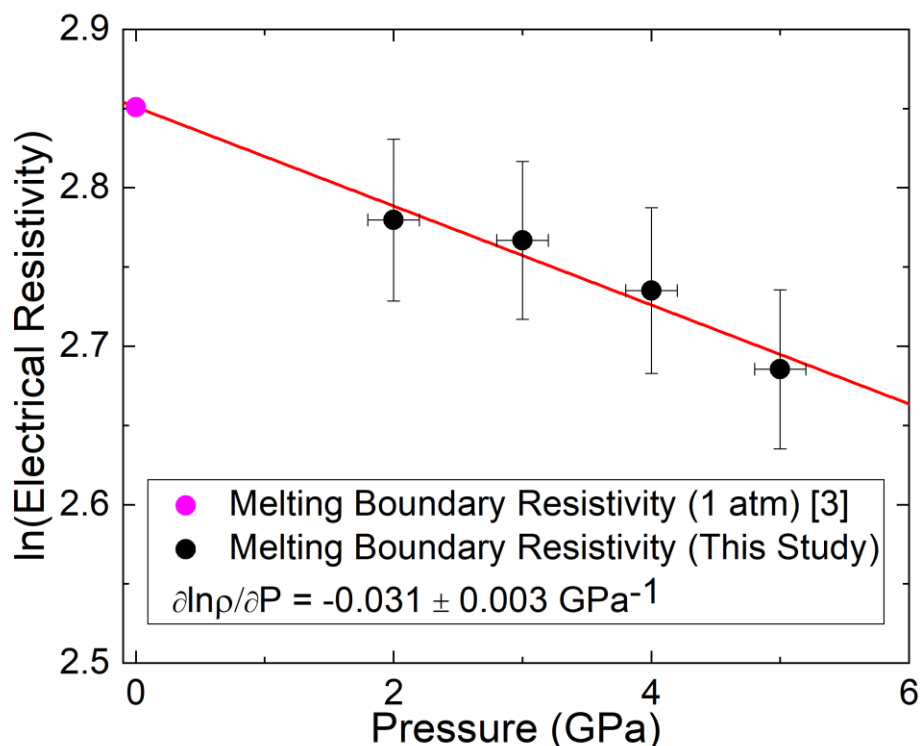


Figure 3.3: The natural logarithm of electrical resistivity along the liquid side of the melting boundary as a function of pressure (Matula, 1979 as [3]). The best-fitted line along the melting boundary is shown was observed to decrease with increasing pressure.

The melting temperature at each pressure was calculated as the average of temperatures of the onset and completion of melting, each of which defines the lower and upper limits, respectively, of the temperature error. Errors on pressure (± 0.25) reflect the error associated with pressure calibration of the press and the thermal pressure during high-temperature experiment, which was indicated by the slight increase in the oil pressure on the pressure gauge. As shown in Figure 3.4, our experimental melting temperatures at 2-5 GPa agree well with many other experimental and theoretical studies (Mitra et al., 1967; Akella and Kennedy, 1971; Mirwald and Kennedy, 1979; Errandonea, 2010; Pham et al., 2010; Hieu and Ha, 2013).

At high pressure and temperatures, it is a challenge to establish a well-controlled temperature gradient which makes thermal conductivity a difficult property to measure. Fortunately, the electronic component of the thermal conductivity of metals, which is the dominant component, can be calculated from the electrical resistivity. The electrical resistivity of a pure metal is inversely proportional to thermal conductivity and is related as such by the Wiedemann-Franz law:

$$\frac{LT}{\rho} = \kappa_e \quad (3.2)$$

where L is the Lorenz number, whose theoretical Sommerfeld value is $2.44 \cdot 10^{-8} \text{ W} \cdot \Omega \cdot \text{K}^{-2}$, T is absolute temperature, and κ_e is the electronic thermal conductivity. Calculated electronic thermal conductivity of Ag at pressures of 2-5 GPa as a function of temperature up to ~ 300 K above the observed melting temperatures is shown in Figure 3.5. The electronic thermal conductivity of Ag at 1 atm calculated from electrical resistivity (Matula, 1979) is also shown for comparison. As expected from their effects on reciprocal resistivity, increasing pressure increases the thermal conductivity in the solid and liquid phases, while increasing temperature decreases the thermal conductivity in the solid phase. In the liquid phase, the thermal conductivity decreased on increasing temperature, which is a clear and unexpected contrast to thermal conductivity at 1 atm. The increase in T-dependence of the resistivity of the liquid at high pressure compared to 1 atm dominates over the increase in T which results in a net negative dependence of thermal conductivity on T as given by Equation (3.2).

3.4 Discussion

The Fermi surfaces of the noble metals have been well investigated and in general they have a nearly spherical shape with multiply connected necks in contact with the (111) hexagonal faces of the first Brillouin zone boundary (Shoenberg, 1960; 1962; Ziman, 1961; 1967; Roaf, 1962; Mott, 1964; Halse, 1969). The electronic configuration of Ag can be written in condensed notation form as $[\text{Kr}]4d^{10}5s^1$. Filled bands up to the 4d-band comprise the core and valence bands below the Fermi level, while a partially filled 5s-band comprises the conduction band. While the filled 4d-band lies below the Fermi level, it interacts with the 5s-band by screening the electrostatic ion core potential and thus

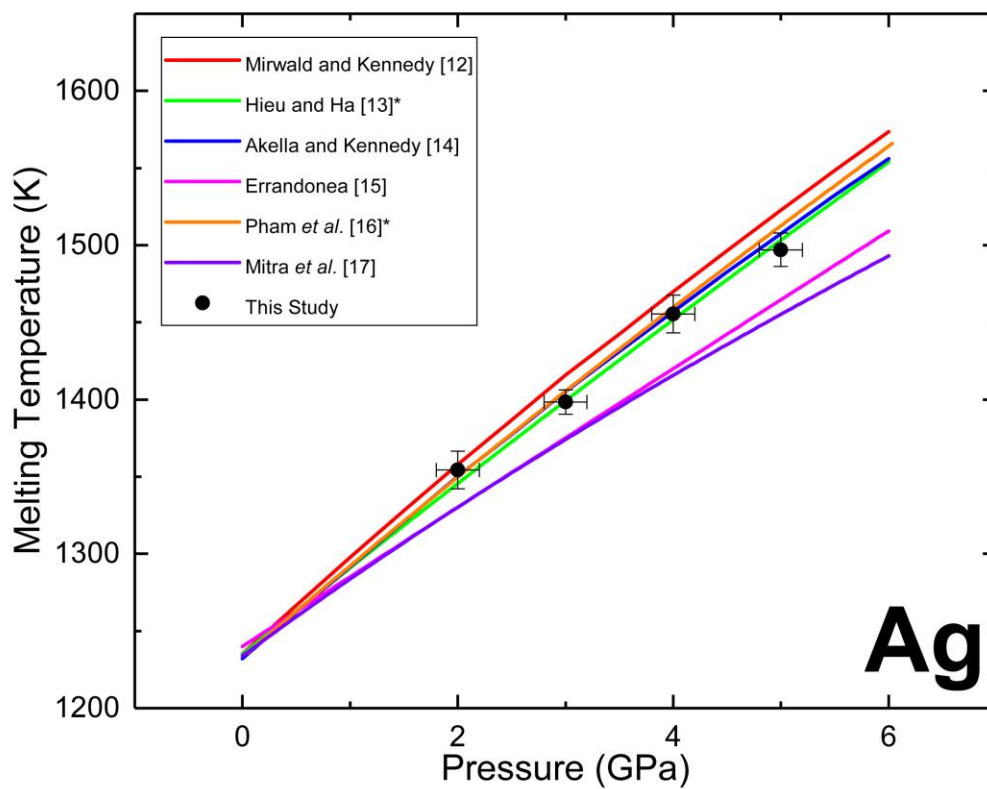


Figure 3.4: Melting temperature of Ag as a function of pressure. Melting temperatures at each pressure for this study were calculated as the average temperatures related to the onset and completion of melting. Prior studies are shown for comparison (* indicates theoretical study; others are experimental studies).

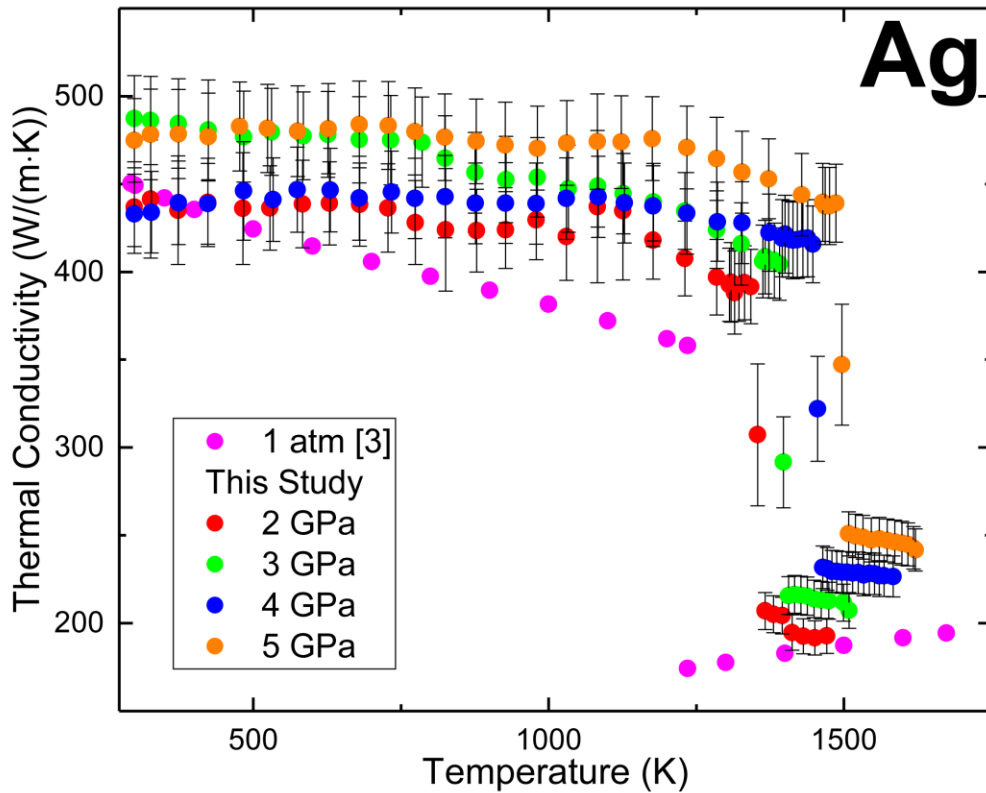


Figure 3.5: Electronic component of thermal conductivity of Ag at pressure 2-5 GPa as a function of temperature calculated from electrical resistivity data in Figure 2.2 and from the resistivity reported at 1 atm (Matula 1979 as [3]) using the Wiedemann-Franz law and the Sommerfeld value ($2.44 \cdot 10^{-8} \text{ W} \cdot \Omega \cdot \text{K}^{-2}$) of the Lorenz number.

increases mobility of electrons in the $5s$ -band. Interaction of the upper-most states of the $4d$ -band with the $5s$ -band contributes to the neck and body distortion of the Fermi surface via hybridization. In pure non-magnetic transition metals with a partially filled d -band, $s \rightarrow d$ scattering arises from interactions with phonons and, to a lesser extent, other electrons. Comparatively, $s \rightarrow d$ scattering has a higher probability of occurrence than $s \rightarrow s$ scattering because the d -band density of states is higher. Because the d -band is fully

occupied in Ag, $s \rightarrow d$ scattering does not occur, leaving only $s \rightarrow s$ scattering in the conduction band occurring dominantly as a result of electron-phonon interactions. This accounts for the lower resistivity of the noble metals compared to all other transition metals (Mott, 1964).

Increasing pressure decreases the volume of the crystal lattice and dampens the amplitudes of propagating thermal phonons, resulting in an increased electron mean free path and lower electrical resistivity. Based on optical property investigations, the energy separation between the Fermi level and 4*d*-band (E_{Fd}) increases with increasing pressure. This results in a decrease of the degree of hybridization and an increase in screening of the ion cores by the *d*-band, which contributes a further decrease of resistivity (Zallen, 1966). These effects are opposed by another pressure-induced effect which is an increase in size and distortion of the Fermi surface. The necks in contact with the Brillouin zone boundary increase, which increases zone boundary scattering and electrical resistivity. However, the pressure effects resulting in a net decrease in resistivity dominate and this trend was observed in both solid and liquid phases (Figure 3.2). Temperature effects on the resistivity are proportional to the collision rates of electrons with thermal phonons and electrons. The collision rate of electrons with thermal phonons increases with temperature. The collision rate itself is proportional to the number of thermal phonons. A simple Bloch theory approximation predicts that the number of thermal phonons is proportional to temperature above the Debye temperature (T_D). Consequently, the electrical resistivity is proportional to temperature for all temperatures above T_D . The T_D of Ag is approximately 228 K (Matula, 1973), and so a near linear trend of the electrical resistivity as a function of temperature was observed in all experiments in the solid and liquid phases (Figure 3.2).

Resistivity in the liquid phase is larger than that of the solid phase due to the increased degree of disorder of ion cores and their electrostatic potential (i.e. short-range atomic order and ionic core potentials with increased mobility) (Cusack, 1963). The Fermi surface in the liquid phase can be approximated as spherical in shape, approximating a free electron model, with a volume large enough to contain all valence electrons. For metals in general, the resistivity in the solid phase increases more quickly with

temperature than in the liquid phase (Cusack, 1963). The opposite was observed at high pressure for Ag. However, given the experimental uncertainty, it is possible to ascertain a trend in the liquid phase that is less steep than that observed in the solid phase. The slopes $(\partial\rho_L/\partial T)_P$, where ρ_L is resistivity in the liquid phase for 2-5 GPa were internally consistent, similar to a recent study on Cu (Ezenwa et al., 2017). The most important result of our study is the decrease of electrical resistivity along the pressure-dependent melting boundary, $(\partial\ln\rho/\partial P)_{T_M}$. This result, alongside a similar observation for Cu, calls into question Stacey's hypothesis that predicts invariance of resistivity of a simple metal along its melting boundary. Despite the change in the structure of the Fermi surface from neck and body distorted shape to a spherical shape, the increase of E_{Fd} as a function of pressure continues into the liquid phase and is enough to offset the aforementioned contributions that increase scattering, resulting in a net decrease of resistivity. We note, however, that $(\partial\ln\rho/\partial P)_T$ on the solid side of the melting boundary is nearly zero within uncertainty.

The trend of increasing electronic thermal conductivity in both solid and liquid phases as a function of pressure is expected from the combined effects of pressure on electron screening and scattering as explained in the previous section. The decrease of electronic thermal conductivity in both solid and liquid phases as a function of temperature is consistent with expected increased scattering of electrons by thermal phonons (Klemens and Williams, 1986). In terms of the Wiedemann-Franz law, thermal conductivity decrease with temperature in the liquid phase can be explained by a rate of increase of resistivity that is larger than the rate of temperature increase while the Lorenz number is constant. We recognize that use of the Sommerfeld value of the Lorenz number at variable temperature and pressure may not be a valid assumption, since the Lorenz number for solid Ag varies not only with temperature and is larger than the Sommerfeld value (Cusack, 1963; Zallen, 1966), but to our knowledge, no literature data exists for the Lorenz number of liquid Ag.

3.5 Conclusion

The temperature-dependence of the electrical resistivity of high-purity Ag has been experimentally determined at high pressures up to 5 GPa and at temperatures of ~300 K

above melting. The results showed a decrease of resistivity along the pressure-dependent melting boundary, contrary to a prediction of resistivity invariance, and are interpreted in terms of competing pressure and temperature effects on the electronic structure of liquid Ag. Linear trends as a function of temperature were observed at each pressure in both the solid and liquid phases. The electronic component of the thermal conductivity was calculated via the Wiedemann-Franz law using the Sommerfeld value of the Lorenz number. Thermal conductivity increased as a function of pressure in both the solid and liquid phases. As a function of temperature, electronic thermal conductivity decreased in both the solid and liquid phases. Within experimental uncertainty, the high pressure melting temperatures agree well with previous experimental and theoretical studies.

3.6 References

- Akella, J. and Kennedy, G.C. 1971. Melting of Gold, Silver, and Copper – Proposal for a New High-Pressure Calibration Scale. *Journal of Geophysical Research*. 76(20): 4969-4977. DOI: 10.1029/JB076i020p04969
- Cusack, N.E. 1963. The Electronic Properties of Liquid Metals. *Reports on Progress in Physics*. 26(1): 361-409. DOI: 10.1088/0034-4885/26/1/310
- Errandonea, D. 2010. The melting curve of ten metals up to 12 GPa and 1600 K. *Journal of Applied Physics*. 108(3): 033517. DOI: 10.1063/1.3468149
- Ezenwa, I.C. and Secco, R.A. 2017. Constant electrical resistivity of Zn along the melting boundary up to 5 GPa. *High Pressure Research*. 37(3): 319-333. DOI: 10.1080/08957959.2017.1340473
- Ezenwa, I.C. and Secco, R.A. 2017. Electronic transition in solid Nb at high pressure and temperature. *Journal of Applied Physics*. 121(22): 225903. DOI: 10.1063/1.4985548
- Ezenwa, I.C., Secco, R.A., Yong, W., Pozzo, M. and Alfè, D. 2017. Electrical resistivity of solid and liquid Cu up to 5 GPa: Decrease along the melting boundary. *Journal of Physics and Chemistry of Solids*. 110: 386-393. DOI: 10.1016/j.jpcs.2017.06.030

- Halse, M.R. 1969. The Fermi Surfaces of the Noble Metals. *Philosophical Transactions of the Royal Society of London A: Mathematical, Physical and Engineering Sciences*. 265(1167): 507-532.
- Hieu, H.K. and Ha, N.N. 2013. High pressure melting curves of silver, gold and copper. *AIP Advances*. 3(11): 112125. DOI: 10.1063/1.4834437
- Karakaya, I. and Thompson, W.T. 1988. The Ag-Re (Silver-Rhenium) system. *Bulletin of Alloy Phase Diagrams*. 9(3): 243-244.
- Klemens, P.G. and Williams, R.K. 1986. Thermal conductivity of metals and alloys. *International Metal Reviews*. 31(5): 197-215. DOI: 10.1179/imtr.1986.31.1.197
- Matula, R.A. 1979. Electrical Resistivity of Copper, Gold, Palladium, and Silver. *Journal of Physical and Chemical Reference Data*. 8(4): 1147-1298. DOI: 10.1063/1.555614
- Mirwald, P.W. and Kennedy, G.C. 1979. The Melting Curve of Gold, Silver, and Copper to 60-kbar Pressure: A Reinvestigation. *Journal of Geophysical Research*. 84(B12): 6750-6756. DOI: 10.1029/JB084iB12p06750
- Mitra, N.R., Decker, D.L. and Vanfleet, H.B. 1967. Melting Curves of Copper, Silver, Gold, and Platinum to 70 kbar. *Physical Review*. 161(3): 613-617. DOI: 10.1103/PhysRev.161.613
- Mott, N.F. 1964. Electrons in transition metals. *Advances in Physics*. 13(51): 325-422. DOI: 10.1080/00018736400101041
- Pham, D.T., Pham, D.T., Nguyen, Q.H. and Phung, D.P. 2010. Melting of Metals Copper, Silver and Gold Under Pressure. *In Proceedings of the 35th National Conference of Theoretical Physics; Aug 2-6; Ho Chi Minh, VT. Hanoi (VT): Institute of Physics (VVL). pp. 148-152.*
- Predel, B. 2006. Ag-Re (Silver – Rhenium). *In Ac-Ag–Au-Zr. Subvolume A, Volume 5 Phase Equilibria, Crystallographic and Thermodynamic Data of Binary Alloys. Springer-Verlag Berlin Heidelberg, Berlin (GER). pp. 1.*

- Roaf, D.J. 1962. The Fermi Surfaces of Copper, Silver and Gold II. Calculation of the Fermi Surfaces. *Philosophical Transactions of the Royal Society of London A: Mathematical, Physical and Engineering Sciences*. 255(1052): 135-152. DOI: 10.1098/rsta.1962.0012
- Scientific Group Thermodata Europe (SGTE). 2007. Ag-W (Silver-Tungsten). *In Binary Systems. Part 5: Binary Systems Supplement 1. Edited by P. Franke and Dieter Neuschütz*. Springer-Verlag Berlin Heidelberg, Berlin (GER). pp. 48-49.
- Secco, R.A. 1995. High p,T physical property studies of Earth's interior: Thermoelectric power of solid and liquid Fe up to 6.4 GPa. *Canadian Journal of Physics*. 73(5-6): 287-294. DOI: 10.1139/p95-040
- Secco, R.A. and Schloessin, H.H. 1989. The electrical resistivity of solid and liquid Fe at pressures up to 7 GPa. *Journal of Geophysical Research: Solid Earth*. 94(B5): 5887-5894. DOI: 10.1029/JB094iB05p05887
- Shoenberg, D. 1960. The de Hass-van Alphen effect in copper, silver and gold. *Philosophical Magazine*. 5(50): 105-110. DOI: 10.1080/14786436008243292
- Shoenberg, D. 1962. The Fermi Surfaces of Copper, Silver and Gold I. The de Haas-van Alphen Effect. *Philosophical Transactions of the Royal Society of London A: Mathematical, Physical and Engineering Sciences*. 255(1052): 85-133. DOI: 10.1098/rsta.1962.0011
- Stacey, F.D. and Anderson, O.L. 2001. Electrical and thermal conductivities of Fe-Ni-Si alloy under core conditions. *Physics of the Earth and Planetary Interior*. 124(3): 153-162. DOI: 10.1016/S0031-9201(01)00186-8
- Stacey, F.D. and Loper, D.E. 2007. A revised estimate of the conductivity of iron alloy at high pressure and implications for the core energy balance. *Physics of the Earth and Planetary Interior*. 161(1): 13-18. DOI: 10.1016/j.pepi.2006.12.001

Vijayakumar, M., Sriramamurthy, A.M. and Naidu, S.V.N. 1988. Calculated Phase Diagrams of Cu-W, Ag-W and Au-W Binary Systems. *Calphad*. 12(2): 177-184. DOI: 10.1016/0364-5916(88)90019-3

Zallen, R. 1966. The Effect of Pressure on Optical Properties of the Noble Metals. *In* Optical Properties and Electronic Structure of Metals and Alloys: Proceedings of the International Colloquium. *Edited by* F. Abelés. 1965 Sept 13-16; Paris, FRA. North-Holland Publishing, Amsterdam (NL). pp. 164-174.

Ziman, J. 1961. The Ordinary Transport Properties of the Noble Metals. *Advances in Physics*. 10(37): 1-56. DOI: 10.1080/00018736100101251

Ziman, J. 1967. The electron transport properties of liquid metals. *Advances in Physics*. 16(64): 551-580. DOI: 10.1080/00018736700101665

Chapter 4

4 Electrical Resistivity of FeS at High Pressures and Temperatures: Implications of Thermal Transport in the Core of Ganymede

The electron is a theory we use; it is so useful in understanding the way nature works that we can almost call it real.

- Richard Feynman

A version of this chapter has been published as:

Littleton, J.A.H., Secco, R.A. and Yong, W. 2021. Electrical resistivity of FeS at High Pressures and Temperatures: Implications of Thermal Transport in the Core of Ganymede. *Journal of Geophysical Research: Planets*. 126(5): e2020JE006793. DOI: 10.1029/2020JE006793

4.1 Introduction

4.1.1 Outer Core Light Elements and the Case for S in Terrestrial-like Cores

Terrestrial planets and some differentiated moons in our solar system are believed to have cores predominantly composed of iron-nickel (Fe-Ni) alloys with some lighter alloying or impurity elements, such as sulphur (S), oxygen (O), silicon (Si), hydrogen, and carbon. It is generally accepted that there is more than one alloying element present; however, the total content and exact proportions of each element in core composition models are not well constrained and subject to considerable debate (Poirier, 1994; Allègre et al., 1995; Li and Fei, 2003; McDonough, 2003; Rubie et al., 2007; Sohl and Schubert, 2007; Vočadlo, 2007). A better understanding of core light elements in planets and moons is critical because of the constraints that core composition places on interior temperature (T) and pressure (P)-dependent phase structures (e.g. solid and liquid portions of the core), heat transport mechanisms and related thermal evolution, and magnetic field generation (Buffett, 2003; 2007; Labrosse and Macouin, 2003; Sohl and Schubert, 2007; Nimmo, 2015; Lay et al., 2008).

Si and O are considered a somewhat controversial pair of coexisting light alloying elements in cores from studies that have suggested they are nearly mutually exclusive based on arguments of oxygen fugacity during differentiation and core formation (Rubie et al., 2007). S has been indicated as a light alloying element that may accompany either Si or O because of its larger and increasing siderophilic tendency over a wide range of high P (Li and Agee, 1996; Hirose et al., 2013). S is also expected in Fe-Ni cores because of its presence in solar system composition models and in iron meteorites (Li and Fei, 2003; McDonough, 2003; McSween and Huss, 2010). Chemically balancing the mass required in the bulk silicate Earth to the chondritic whole Earth composition constrains the S content of the core to ~1-2 wt.% or less (McDonough, 2003; Rubie et al., 2007; Wood et al., 2006; Hirose et al., 2013). While theoretical studies investigating binary and ternary systems involving Fe and S have predicted S contents up to approximately 14 wt.% in the core (Helffrich and Kaneshima, 2004; Hirose et al., 2013). However, core S content estimates ≥ 10 wt.% are largely contested as they would produce a significant discrepancy of S overabundance compared to the overall volatility trend once the whole Earth composition has been corrected (McDonough, 2003). In tandem with geochemical arguments, seismological observations of core density deficits and density contrasts between Earth's liquid outer core and solid inner core places geophysical constraints on light element abundance (Alfè et al., 2002; Badro et al., 2014) that must be adhered to.

Estimates of the core S content of other terrestrial bodies and differentiated moons are as ill-constrained as that of the Earth, albeit they rely more heavily on theoretical models due to fewer observational data. Estimates for the core S content in Mars generally range between ~10-20 wt.% (Sanloup et al., 1999; Khan and Connolly, 2008; Khan et al., 2018; Wang and Becker, 2017), although a recent estimate suggests 6.6 wt.% S (Yoshizaki and McDonough, 2020). In comparison, estimates for Mercury are lower and generally range between ~2-6 wt.% (Schubert et al., 1988; Rivoldini et al., 2009; Rivoldini and Van Hoolst, 2013). In contrast to the cores of terrestrial planets, estimates of the S content of Ganymede are less certain. Under specific thermal history and secular cooling conditions, the core of Ganymede may contain S contents between ~3-32 wt.% on the basis of magnetic field generation. Additionally, some models have also predicted solid portions

of Ganymede's core to consist of 36.5 wt.% S, the stoichiometric proportion of FeS (Hauck et al., 2006; Bland et al., 2008; Kimura et al., 2009).

4.1.2 Effect of S on the Fe-S Phase Diagram and Aspects of Core Convection

Light elements can have considerable effects on the physico-chemical properties of Fe alloys and therefore the dynamics of planetary cores. Investigations on the Fe-rich side of the Fe-S binary system at ambient P have shown liquidus T to decrease with increasing S content, with a eutectic T and composition of ~1260 K and 31 wt.% S. A similar trend was also observed at high P (Li and Fei, 2003). However, the effect of increasing P on the liquidus T as a function of S content is nonlinear and shifts the eutectic composition in the Fe-rich direction (Brett and Bell, 1969; Li and Fei, 2003; Chen et al., 2008a; 2008b; Buono and Walker, 2011; Saxena and Eriksson, 2015; Mori et al., 2017; Pommier et al., 2018).

The importance of freezing point depression by S of an Fe-S core is related to the presence and initial nucleation of a solid inner core. The observed nonlinear behaviour of the liquidus T has sparked a growing acknowledgement of thermally stratified S-rich layers and precipitation of Fe, also called Fe-snowing, in the cooler outer-most regions of the outer core of such planetary bodies as Mercury, Mars, and Ganymede. Snow zones provide additional density-driven contributions to convective motions in the outer core and to power dynamo action that offset hindering effects by the release of latent heat caused by precipitation of snow (Hauck et al., 2006; Chen et al., 2008b; Williams, 2009; Buono and Walker, 2011; Morard et al., 2011; Zhan and Schubert, 2012; Christensen, 2015; Rückriemen et al., 2015; 2018; Davies and Pommier, 2018; Pommier, 2018; Pommier et al., 2018). Thus, our knowledge of the thermo-dynamical relationships between the core and mantle and between the outer and inner core is especially vital for our understanding not only of the sources that power and sustain the planetary dynamos that produce the persistent magnetic fields in Earth, Mercury and Ganymede (Schubert et al., 1988; Labrosse and Macouin, 2003; Buffet, 2003; 2007; Hauck et al., 2006; Nimmo, 2015; Bland et al., 2008; Lay et al., 2008; Rivoldini et al., 2009; Kimura et al., 2009;

Zhan and Schubert, 2012; Christensen, 2015; Rückriemen et al., 2015; 2018;), but also of times during which these sources were active and dominant.

The flow of heat through the core-mantle boundary (CMB) controls the cooling of the core. Thus, it controls the rate of inner core and snow zone growth and intensity of both thermal convection, arising from super-adiabatic heat flow in the outer core, and compositional convection, arising from the growth of the inner core and snow zones (Hauck et al., 2006; Olson, 2016). The convective motions of electrically conductive Fe-rich liquid outer cores are thought to generate the observed magnetic fields. Estimates of the quantity of heat extracted from the core through the CMB rely on a number of modelled physical parameters, such as temperature, chemical composition, material properties of mineral phases in the lower mantle and D'' region, and dynamics, of the core and lower-most mantle. In the case of Earth, Mercury, and Ganymede, a major constraint is the presence of a persistent dynamo (Buffett, 2003; 2007; Labrosse and Macouin, 2003; Nimmo, 2015; Lay et al., 2008).

Reported estimates of the heat flux out of the core and through the CMB of Ganymede range from $\sim 1\text{-}6$ mW/m² (Hauck et al., 2006; Kimura et al., 2009; Rückriemen et al., 2015; 2018), whereas estimates of the adiabatic heat flux at the top of the core range from $\sim 4\text{-}12$ mW/m² (Bland et al., 2008; Rückriemen et al., 2015; 2018). Poorly constrained parameters can propagate large uncertainty such that actual heat fluxes across the CMB may be much lower or higher than the heat transported down the core adiabat. If the former, excess heat would accumulate in a thermally stratified layer at the top of the outer core and obviate the need for thermal convection from below. This would restrict the type of convection in the outer core to compositional convection derived from the buoyancy of exsolved lighter alloying elements from inner core growth and/or snow production and subsequent snow re-melting. If the latter, a much colder and denser boundary at the top of the core would develop and thermal convection would be partially driven from the top down, in addition to compositional convection (Buffett, 2003; 2007; Rückriemen et al., 2015). Along with the heat flow through the CMB, evaluating the adiabatic heat flow in the outer core is thus a critical step in assessing the style(s) of convection in a liquid outer core.

The uncertainty of core P and T conditions and S content of Ganymede's core and non-linearity of the Fe-FeS eutectic system have led to a number of physico-chemical evolution pathways of Ganymede's core as it cools. Consequently, these may allow for different types of composition convection to contribute to thermal transport and dynamo power sources (Hauck et al., 2006; Breuer et al., 2015). We will highlight three general categories: i) At low S contents (i.e. a few weight percent), it is possible to have an Earth-like scenario with crystallization of an Fe core surrounded by a molten Fe-FeS outer core. Release of latent heat and the lighter element S would aid in convective motions of the outer core by thermal and chemical buoyancy; ii) At higher S contents on the Fe-rich side of the eutectic, Fe-snowing is permissible to drive convection motions from the top-down and settle to form an Fe inner core since solid Fe is expected to be denser than the residual liquid. Fe snowing in Ganymede's core has received significant attention in recent years due to on-going debate as to whether or not thermally driven convection is a likely driving force to power a dynamo. The chemically-induced convection of a liquid core brought on by snowing layers is an efficient power source and can reliably reproduce the magnetic observations of a dipolar field (Christensen, 2015; Rückriemen et al., 2015; 2018); iii) On the FeS-rich side of the eutectic, FeS can be precipitated and is thought to be less dense than the surrounding residual liquid. As a result, the FeS migrates upwards through the core and can drive convective motions from the bottom-up and act as a driving force for a dynamo (Rückriemen et al., 2018). It is possible for the precipitate to accumulate and form a solid shell of FeS around a molten core.

4.1.3 Electrical Resistivity, Thermal Conductivity, and the Wiedemann-Franz Law

The close resemblance of material properties among Ni, Fe and Fe-10 wt.% Ni content as expected in terrestrial cores suggests core properties could be adequately approximated through investigations of pure Fe (e.g. Jephcoat et al., 1986; Mao et al., 1990; Zhang and Guo, 2000; Lin et al., 2002; 2003; Mao et al., 2006; Sakai et al., 2011; Martorell et al., 2013; 2015; Gomi and Hirose, 2015; Wakamatsu et al., 2018). Regarding electron transport properties, the effect due to Ni content weakens as a function of increasing P and T (Gomi and Hirose, 2015). However, the presence of a light element such as S, a non-metallic and volatile element, is expected to have a non-negligible effect on the

electron transport properties of Fe. For example, the end members of the Fe-FeS system are classified as an electrical conductor and semiconductor, respectively.

Investigations of the electrical resistivity (ρ) of the Fe-FeS system are relatively few (e.g. Argyriades et al., 1959; Karunakaran et al., 1980; Kobayashi et al., 2001; 2005), with a small surge of studies in recent time (Suehiro et al., 2017; Pommier, 2018; Gomi and Yoshino, 2018; Wagle et al., 2018; 2019; Manthilake et al., 2019). The majority of recent studies are based on the theory of electrical properties at P and T conditions of cores of larger planetary bodies, such as Earth and Mars. For instance, Wagle et al. (2018; 2019) showed for liquid Fe-S (~16 wt.% S) at P and T conditions corresponding to Earth's core that the criterion for resistivity saturation effects is met and the T-coefficient of ρ changes from positive to negative with increasing P. While the presence of S does increase ρ compared to that of pure Fe at identical conditions, their results indicated a non-linear behaviour with increasing T, as would otherwise be predicted by the Bloch-Grüneisen approximation, and places vital constraints on the effect of S as a core light element. However, theoretical extrapolations are limited given the lack of available experimental data and the capability for comparisons thereof. A large contribution to available experimental results was produced by Pommier (2018) who reported direct measurement values of ρ of solid and liquid Fe, Fe-5wt.%S, Fe-20wt.%S and FeS at P up to 8 GPa and T up to ~2123 K. The results showed that ρ increased as a function of increasing S content and increasing T, decreased as a function of increasing P, and exhibited an abrupt, large increase in magnitude at T above the eutectic and exceeding the liquidus. These are typical behaviours for metals and metallic alloys at high P and T, along with the observed impurity content effects and the effect of structural disorder upon melting (Faber, 1972; Rossiter, 1987; Poirier, 2000; Mizutani, 2004). Although the P-T conditions (Pommier, 2018) are far from the conditions of Earth's core, these measurements are important because the results provide a foundation to which theoretical frameworks must be anchored.

The relevance of ρ to core thermal properties and dynamics is established by use of the Wiedemann-Franz Law (WFL):

$$\frac{LT}{\rho} = \kappa \quad (4.1)$$

where κ is thermal conductivity and L is the Lorenz number that normally takes a value equal to the Sommerfeld value ($2.44 \cdot 10^{-8} \text{ W} \cdot \Omega \cdot \text{K}^{-2}$). The WFL is a semi-empirical statement which relates ρ to κ , and this approximation has been shown to be valid for a number of metal and metallic alloys (Franz and Wiedemann, 1853; Klemens and Williams, 1986). It should be noted that Eqn. (4.1) only calculates an estimate of the electronic contribution to κ and does not account for the additive contribution by lattice vibrations or phonons to the total thermal conductivity. This is in part why the WFL holds relatively well for metals and metallic alloys because the electronic contribution is the dominant contributor to κ in those materials (Klemens and Williams, 1986). The Sommerfeld value of L is a theoretical value based on the free-electron model of metals. Not only is such a model not entirely valid for transition metals such as Fe, the Lorenz number also has been shown to exhibit both composition (Secco, 2017) as well as P- and T-dependence (Kumar et al., 1993). Thus, the value of L is expected to deviate from the Sommerfeld value and, if uncorrected, can lead to either an over- or underprediction of κ when compared to measured values. However, it has been demonstrated that the Sommerfeld value can be applied to pure Fe at relatively low P (<6 GPa) and T up to 2100 K (Secco, 2017).

Manthilake et al. (2019) performed similar measurements of ρ of Fe-FeS alloys at a P of 8 GPa and T up to 1700 K. Their reported values were significantly larger than values by Pommier (2018) by approximately two orders of magnitude, and suggest that the lower values of ρ were due to conductive impurities present in the sample and/or partial reactions forming more Fe-rich shunt regions within their Fe-S alloys. Calculated κ of FeS using the WFL reported by Pommier (2018) showed a span of $\sim 3\text{-}5 \text{ W/m} \cdot \text{K}$ over a P range of 4.5 to 8 GPa and increasing T in the solid state. In the liquid state at 4.5 GPa, κ decreased from ~ 2 to $\sim 1 \text{ W/m} \cdot \text{K}$ with increasing T. In contrast, Manthilake et al. (2019) reported a value of κ of $\sim 10^{-2} \text{ W/m} \cdot \text{K}$ at 8 GPa and 1300 K using Eqn. (4.1) along with the Sommerfeld value of L . After estimating a correction for the phonon contribution, their reported total κ was $\sim 4 \text{ W/m} \cdot \text{K}$, comparable to values by Pommier (2018). The results are not reconciled because the κ values reported by Pommier (2018) represented a

lower bound estimate, acknowledging the need for a further phonon contribution correction that would produce larger total κ values. The conflicting results of these two studies highlight the need to have reliable values of ρ to calculate κ of Fe-FeS alloys.

In this study, we developed an experimental design to measure directly and produce robust results of ρ of solid (powder) and liquid FeS at high P and discuss the implications for adiabatic thermal transport in the S-bearing cores of Ganymede.

4.2 Materials and Methods

FeS powder was purchased from Alfa Aesar (99.98% purity). Initial attempts were made to replicate the in-house powder-to-wire sample preparation method as detailed by Berrada et al. (2020) for Fe-Si powders of varying Si contents. Unlike their work, this procedure was complicated by the non-negligible T range between the solidus and liquidus and volatility of a partially and fully molten FeS sample. However, this served as the motivating factor for creating a high P cell design to measure directly the electrical resistivity of a powder sample using a 4-wire resistance technique. An illustration of the cross-section of the cubic P cell design used for all experiments in this work is shown in Figure 4.1. Similar three sectioned cubic P cells have been successfully implemented with a 4-wire resistance technique to measure the electrical resistivity of solid and liquid transition metals and transition metal alloys (Ezenwa and Secco, 2017a; 2017b; 2017c; Ezenwa et al., 2017; Littleton et al., 2018; 2019; Berrada et al., 2018; 2020). All experiments were conducted in a 1000-ton cubic anvil press, as described by Secco (1995), to generate high quasi-hydrostatic P. Thorough descriptions of the P cell design are found in the appendices (Appendix A).

4.2.1 High Pressure-Temperature Electrical Technique

Each pair of platinum (Pt) and platinum-rhodium alloy (Pt-Rh) wires housed in the two four-hole alumina tubes creates two Type-S thermocouples (TCs) that were used to monitor the temperature of the center of the P cell, or the sample temperature. The mechanical contact between the FeS powder sample, tungsten (W) disks, and TCs (Figure 4.1) allows each TC to additionally serve as electrodes. A constant direct current was

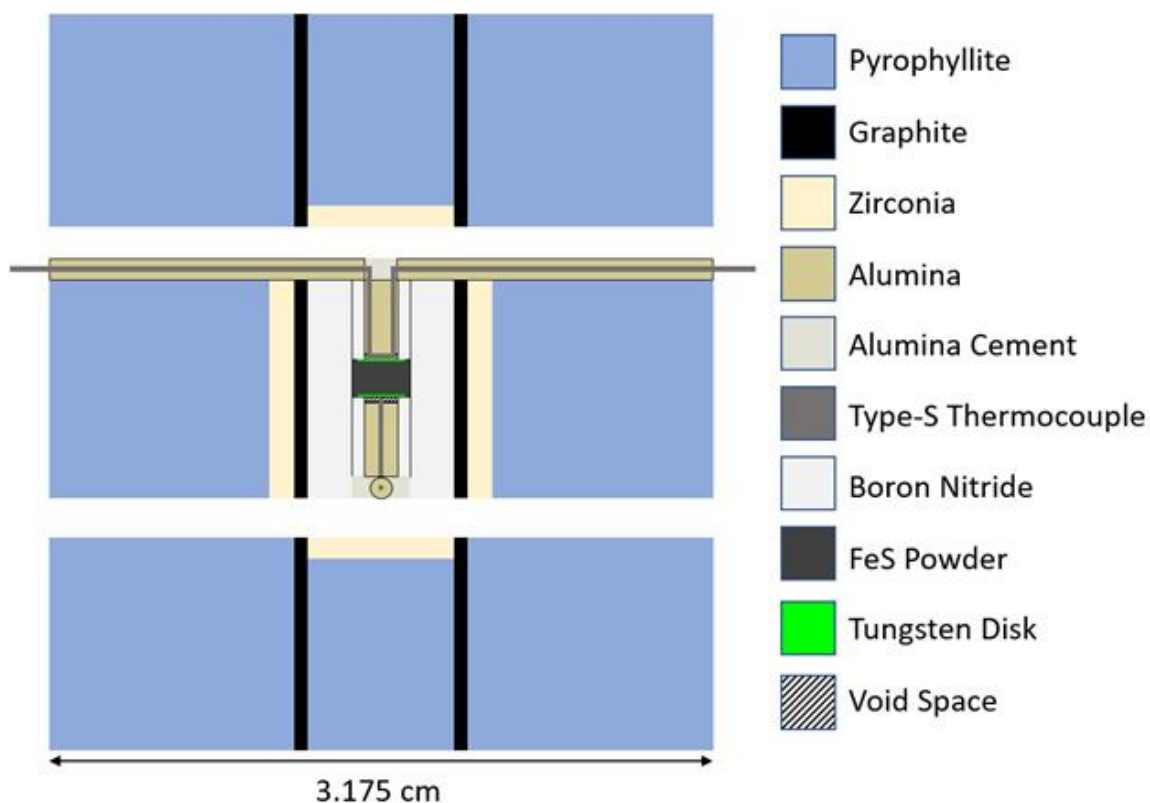


Figure 4.1: Illustration of the cross-section of the cubic pressure cell used in all experiments.

passed through lateral anvils to the Pt arms of the TCs while the voltage across the sample was measured using the Pt-Rh arms – thus employing a 4-wire resistance technique. A mechanical switch was employed to enable alternating between a measurement of the sample T and voltage drop for resistance measurement. The additional use of a polarity switch, while in resistance measurement mode, to sample voltage measurements ensured removal of thermoelectric and other parasitic voltage effects. Since boron nitride is an electrical insulator (ρ of $\sim 10^{11} \Omega \cdot \text{cm}$), the contribution to the measured sample voltage by the surrounding boron nitride is negligible and can be ignored.

The measured sample voltage (V) and the provided constant direct current (I) were used to calculate the sample resistance (R) via Ohm's Law:

$$R = V/I \quad (4.2)$$

Pouillet's Law relates the geometry and electrical resistivity (ρ) of a material to the resistance:

$$R = (\rho \cdot l)/A \quad (4.3)$$

where l is the length of the sample and A is the cross-sectional area of the cylindrical sample. Thus, the equation for ρ of the sample is:

$$\rho = R \cdot \pi \cdot D^2 / 4l \quad (4.4)$$

where D is the diameter of the sample.

4.2.2 FeS Electrical Resistivity: Experimental Specifications

The ρ of solid (powder) and liquid FeS were measured at P from 2 to 5 GPa and T up to approximately 1785 K. A high alternating current with a typical amplitude of 350 A was passed through the segmented graphite sleeve to generate high T . All samples were pre-heated to and maintained at a T of ~ 900 K for approximately 10 minutes before quenching prior to acquiring voltage measurements for all experiments. Sample voltages were measured using a Keysight 34470A data acquisition meter operating at 20 Hz with 1 μ V resolution with a constant direct current of 0.2 A provided by a Keysight B2961 power source. A minimum of 10 sample T measurements was made immediately before and after each sample voltage measurement, which itself consisted of a minimum of 5 measurements per current polarity. Each data point of ρ reported in this work consists of averages of both sample T and voltage measurements. Voltages measured by the Type-S TCs were corrected for P effects (Getting and Kennedy, 1970). Calculated P - and T -dependent contributions to the measured voltages by the W disks were less than 2% (Littleton et al., 2019) and were ignored.

A Nikon SMZ800 microscope operating at 40x magnification was used to measure the post-experimental sample D and l after removal from the press and subsequent grinding and polishing. The determined sample voltage and geometries were employed to calculate ρ via Eqns. (4.2) and (4.4). Errors of ρ arising from geometry uncertainty (0.013 mm), obtained from calibration of the microscope and integrated software, and sample

voltage fluctuations were assessed using standard error propagation methods. Standard error propagation methods were used to determine error of T, along with a fixed ± 10 K additional contribution to account for the thermal gradient established by the distance from a TC to the sample center (Schloessin and Lenson, 1989). A JEOL JXA-8530F field-emission electron microprobe operating with a 20 kV accelerating voltage, 50 nA probe current, and 100 nm spot-size beam was used to determine the composition of the recovered sample, W disks, and TCs and the extent of chemical interaction between the three components.

4.3 Results

4.3.1 Electrical Resistivity and Electronic Thermal Conductivity

Figure 4.2a shows measured values of ρ of FeS up to 5 GPa and 1785 K from this study, while Figure 4.2b shows the same results with several annotations to aid data visualization and interpretation. The values of ρ close to room T (~ 300 K) at 2 and 3 GPa are the largest values of solid state FeS and are associated with the troilite (FeS I) phase. The largest decrease of ρ within a 50-degree interval was observed between ~ 325 K and ~ 375 K and is interpreted as the phase transition from FeS I to the hexagonal (FeS IV) phase. T estimates of this phase boundary by Fei et al. (1995) are shown in Figure 4.2b and are in good agreement; however, our inferred results indicate that the phase boundary T at 2 and 3 GPa are slightly lower than the shown estimates. Ambient P investigations of the magnetic properties of FeS have indicated a transition where the orientation of anti-ferromagnetic alignment changes from parallel to perpendicular to the c-axis (α -transition) that coincides with the FeS I-IV transition (Wang and Salveson, 2005). Any effect on ρ due to this transition cannot be confidently recognized or at least separated from the effects due to the structural transition based on our measurements.

At 4 and 5 GPa, the room T measurements of ρ are noticeably lower than lower P values and show a reduction in magnitude of nearly 25%. At these conditions, the sample is no longer in the FeS I phase and is either in the MnP-type (FeS II) phase or FeS IV phase (King and Prewitt, 1982; Kusaba et al., 1998; Urakawa et al., 2004). In studies investigating phase relationships of FeS, the FeS II phase has not been consistently

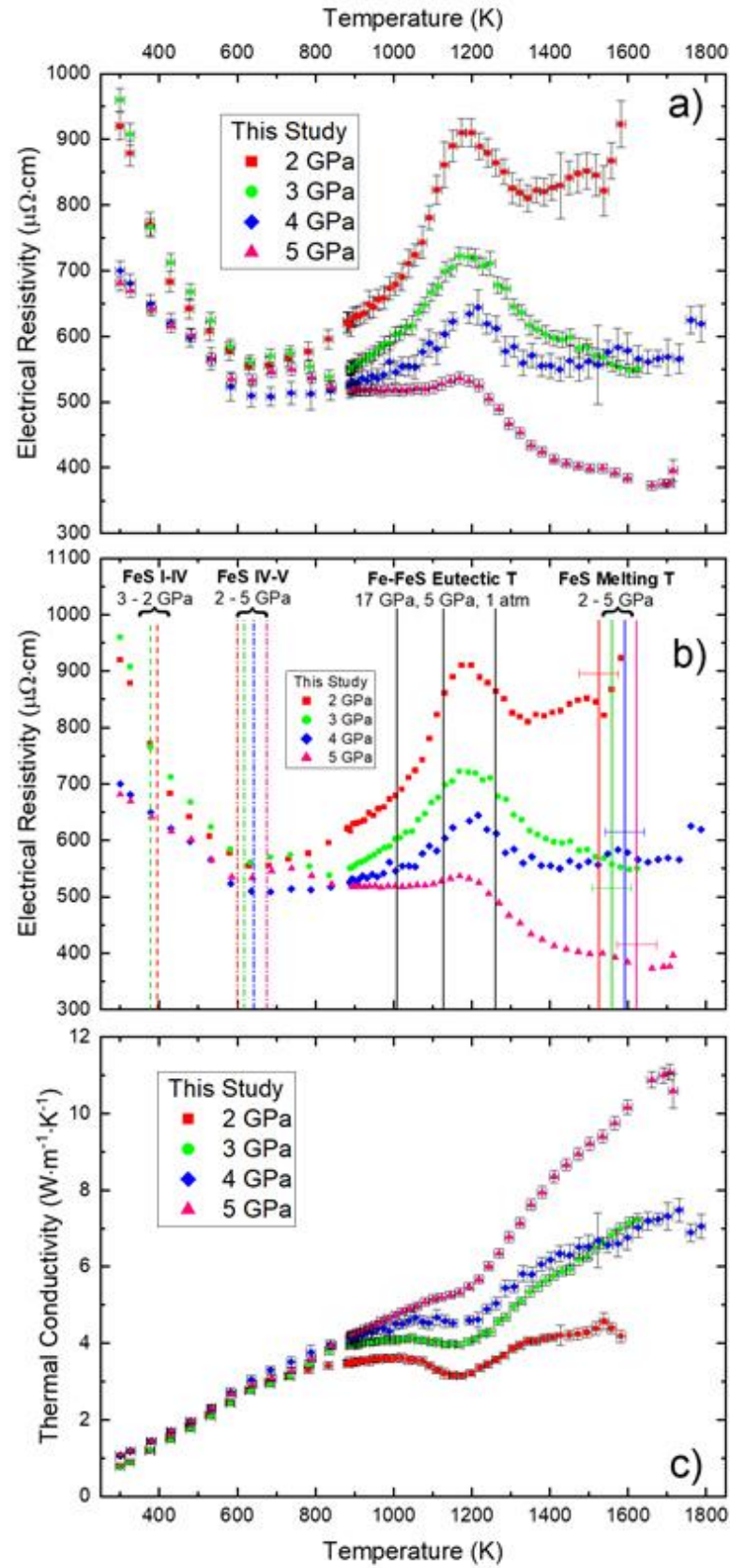


Figure 4.2: (a) Measured electrical resistivity of FeS at pressures of 2 – 5 GPa as a function of temperature; b) Annotated interpretation of phase transitions (solid state and melting) and incongruent melting from measured electrical resistivity. Temperature estimates of the FeS I-IV and FeS IV-V solid state phase transition were taken from Fei et al. (1995). Estimates of the FeS melting boundary were taken from Boehler (1992) with an uncertainty of ± 50 K. Estimates of eutectic temperatures for the Fe-FeS binary system were taken from Morard et al. (2007); c) Calculated electronic component of thermal conductivity of FeS at pressures of 2 – 5 GPa as a function of temperature from the measured electrical resistivity using the Wiedemann-Franz law and the Sommerfeld value of the Lorenz number.

identified (Kusaba et al., 1998; Urakawa et al., 2004). Since there is not a clear indicator shown in the results of ρ , we cannot confidently infer a FeS II \rightarrow FeS IV around room T at 4 and 5 GPa. However, the results indicate either: i) FeS II has indistinguishable or similar ρ and T-coefficient of ρ as FeS IV; or ii) the sample is in the FeS IV phase at room T. Previous high P investigations at low and ambient T have shown that FeS II is a more electrically conductive phase than FeS I (Karunakaran, 1980; Kobayashi et al., 2001; 2005). At ambient P and high T, the FeS I-IV transition was also indicated by an increase in electrical conductivity (Karunakaran, 1980). Regardless of the specific room T phase of the FeS sample at 4 and 5 GPa in our experiments, the distinctly lower value of ρ at these conditions compared to 2 and 3 GPa are supported by these works.

The T-dependence of ρ of FeS at all experimental P up to ~ 600 K is negative, indicating these phases exhibit semiconductor behaviour. FeS II has been shown to exhibit metallic behaviour at low T (< 100 K), characterized by a positive quadratic T-dependence (Kobayashi et al., 2001; 2005). If FeS II is the starting phase at 4 and 5 GPa at ambient T, this confines a metal-semiconductor transition between 100 K to 300 K based on our measurements. The T-dependence underwent an abrupt change in sign to an increase with increasing T around 600 K for all P, observations that are interpreted as the phase transition from FeS IV to the simple NiAs-type (FeS V) phase. T estimates of this phase boundary by Fei et al. (1995) are shown in Figure 4.2b and are in good agreement. The T-dependence shows metallic behaviour with increasing T after this transition, with the

effect of increasing P strongly diminishing or flattening the observed behaviour. The FeS IV \rightarrow FeS V transition coincides with a second magnetic transition from anti-ferromagnetic to paramagnetic (β -transition) (Wang and Salveson, 2005). As with the previous magnetic transition, it remains unclear the magnitude of the individual effects on ρ by the structural and magnetic transitions. The ρ of FeS at all P continued to increase until a high T peak value around 1200 K, where after there is a sudden decrease in the magnitude of ρ . There are no further magnetic transitions expected beyond the β -transition nor structural phase transitions in the solid state. We are doubtful that this represents a change in electronic state, such as a high T reversion to a semiconducting solid state. Instead, we interpret it to be the presence of non-stoichiometric variants of FeS of the entire sample.

The T values of these ρ peaks are noteworthy because they fit within the P-T confines of the Fe-FeS eutectic T. High P estimates of the eutectic T by Morard et al. (2007) are displayed in Figure 4.2b. It has been shown that the eutectic T and eutectic S content of the Fe-FeS system both decrease with increasing P up to approximately 17 GPa (Kubaschewski, 1982; Fei et al., 1997; Li and Fei, 2003; Morard et al., 2007). While some Fe-S phase diagrams (e.g. Kubaschewski, 1982) at ambient P indicate a small high T solidus-liquidus region at 36.5 wt.%S, P-T diagrams of FeS do not indicate this and instead report FeS V as stable until melting (e.g. Urakawa et al., 2004). The presence of non-stoichiometric proportions with S contents slightly below 36.5wt.% would initiate incongruent melting above eutectic T, hundreds of degrees below the expected melting T of FeS. The melt produced would be enriched in Fe and more electrically conductive, resulting in a noticeable decrease in ρ . S content within the melt is expected to increase with continued heating, which reduced the negative T-dependence of ρ after the peak T. Melting T estimates of FeS by Boehler (1992) are extrapolated to P of this study and shown in Figure 4.2b. A distinct feature attributed to melting/liquidus T as in numerous previous works (e.g. Silber et al., 2017; 2018; 2019; Ezenwa and Secco, 2017b; 2017c; Ezenwa et al., 2017; Littleton et al., 2018; Berrada et al., 2018; 2020) is masked given the gradual production of melt over a relatively large T range. The observed P-dependency appears to have a larger effect in the partially molten and fully molten states compared to

the solid state. Lastly, the effect of increasing T of a fully molten FeS sample decreased ρ , indicative of semiconductor-like behaviour.

The sample voltage measurement rate was increased at ~ 900 K in each experiment in order to reduce the amount of time measurements were made in the partially and fully molten state. The heating mechanism in these experiments requires some time before heating accelerates. As a result, the measurements appear dense around 900 K, but spread out more with increased heating despite the measurement rate remaining the same. For context, the time duration for all measurements at 4 GPa from ~ 888 K to ~ 1785 K was ~ 2 minutes. While in the molten state, chemical contamination (e.g. between sample and electrodes) and liquid confinement become complications that can severely burden or ruin an experiment. For instance, the last high T values of ρ at 2, 4, and 5 GPa that increase abruptly relative to the preceding trends are usual experimental indicators of one or both of these obstacles. While contamination and confinement are functions of both T and time, we found the latter to be dominant effect and one that is more easily controlled in our experimental set up. A fast heating rate that reduces control of T is compensated by a reduced measurement time of the sample in the molten states.

Figure 4.2c shows calculated values of κ of FeS up to 5 GPa and 1785 K from this study using the WFL as shown in Eqn (4.1) and the Sommerfeld value of L . The general P and T effects are clear: the electronic κ of FeS increased with increasing P and T at all T in the FeS V , partially molten and fully molten states. Since these values only represent the electronic contribution, the results shown represent a lower bound of the total κ using an invariant Lorenz number.

4.3.2 Post-Experiment Sample Analyses

Figure 4.3a shows an image of the cross-section of the 4 GPa pressure cell centered on the sample after an experiment and Figure 4.3b shows a back-scattered electron image of the same sample. Tabulated electron microprobe results of 20 locations correspond to labeled sites on the Figure 4.3b image. The analyses showed noticeable contamination of the sample limited to a thin portion of the boundary with the W disks that may indicate formation of WS_2 and $Fe_{1-x}S$ (Štemprok, 1971). The bulk of the sample retained an Fe-S

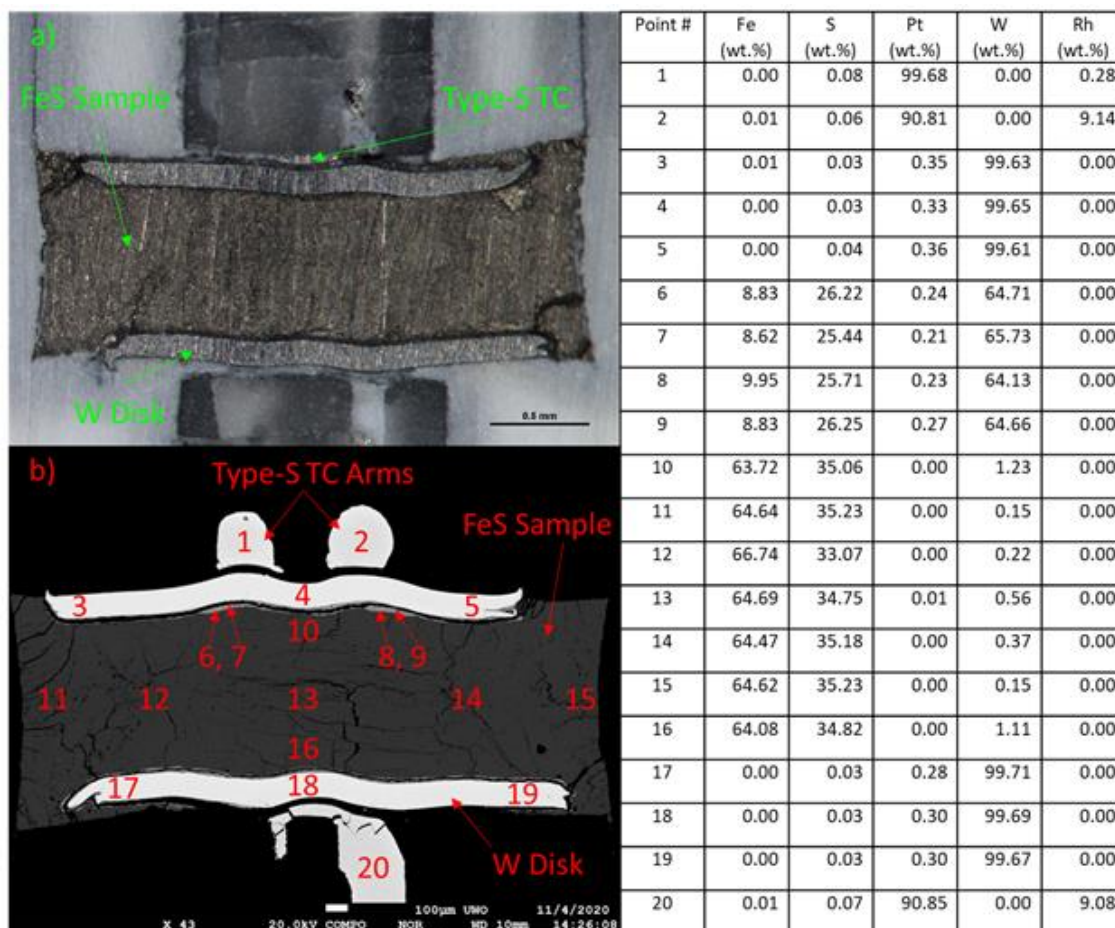


Figure 4.3: (a) Cross-sectional view of the post-experiment 4 GPa pressure cell. Apparent surface lineations of the sample, W disks, and surrounding BN are due to sanding and lighting. (b) Back-scattered electron image of the sample from a) at a different depth due to additional grinding and polishing required for pre-analysis sample preparation. Results of the microprobe have been tabulated and normalized.

Instances of negative normalized values have been set to 0.00 wt.%.

composition and the results confirmed a non-stoichiometric composition with S contents less than 36.5 wt.%. The bulk of the W disks and arms of the Type-S TC wires retained high chemical purity. Additional post-experiment back-scattered images and tabulated microprobe results for the 2, 3, and 5 GPa experiments are found in the Supporting Information section. Since the sample is slightly more Fe-rich than anticipated, which implies a more electrically conductive sample than FeS, the measured values of ρ and calculated values of κ represent a lower- and higher-bound, respectively, of FeS transport

properties at all experimental P and T conditions of this study. However, since there is no evidence of Fe phase contiguity which would provide conductive pathways, we suggest that any effect on resistivity is small.

4.4 Discussion

4.4.1 Comparison to Prior Studies

Figure 4.4a shows measured values of ρ of FeS up to 5 GPa and 1785 K from this study compared to previous studies (Argyriades et al., 1959; Pommier, 2018). Comparison to Manthilake et al. (2019) is not shown due to scaling (ρ exceeds $10^4 \mu\Omega\cdot\text{cm}$). Our measured values of ρ consistently indicate FeS is more electrically conductive compared to measurements by Pommier (2018) at similar P and T conditions. Both results clearly showed that ρ decreased with increasing P. Without complete datasets, comparisons of inferred structural and related magnetic transitions at low T are not possible.

Measurements in the T range of 650 K to 1200 K show similar trends, namely that ρ increased with increasing T. Thus, both studies observed a metallic-like behaviour of FeS within this T range. The T-dependent trend of ρ at 4.5 GPa up to ~ 1630 K closely resemble our observations at 4 GPa. Namely, there is an increase in ρ until a peak T that marks the onset of a more conductive Fe-rich melt being produced. As more melt is produced and S content increases, the decreasing trend of ρ gradually tails off. A peak cannot be easily identified at 8 GPa; however, this is consistent with our observation that increasing P diminishes or flattens the ρ peaks.

The most apparent differences are the values of ρ within the perceived melt regions as our results do not show an increase of ρ upon melting, let alone values of ρ that are of magnitudes comparable to 3.2 and 4.5 GPa. Pommier (2018) defined the observed abrupt increases as a transition from a solid- to liquid-dominated regime and noted that the transition T occurs slightly higher than the eutectic T of the Fe-FeS system or to the liquidus. Similar to the final measurements of our 2, 3 and 5 GPa results, we attribute the abrupt increases Pommier (2018) observed to chemical contamination and apparent incomplete liquid confinement. In this context, apparent incomplete liquid confinement

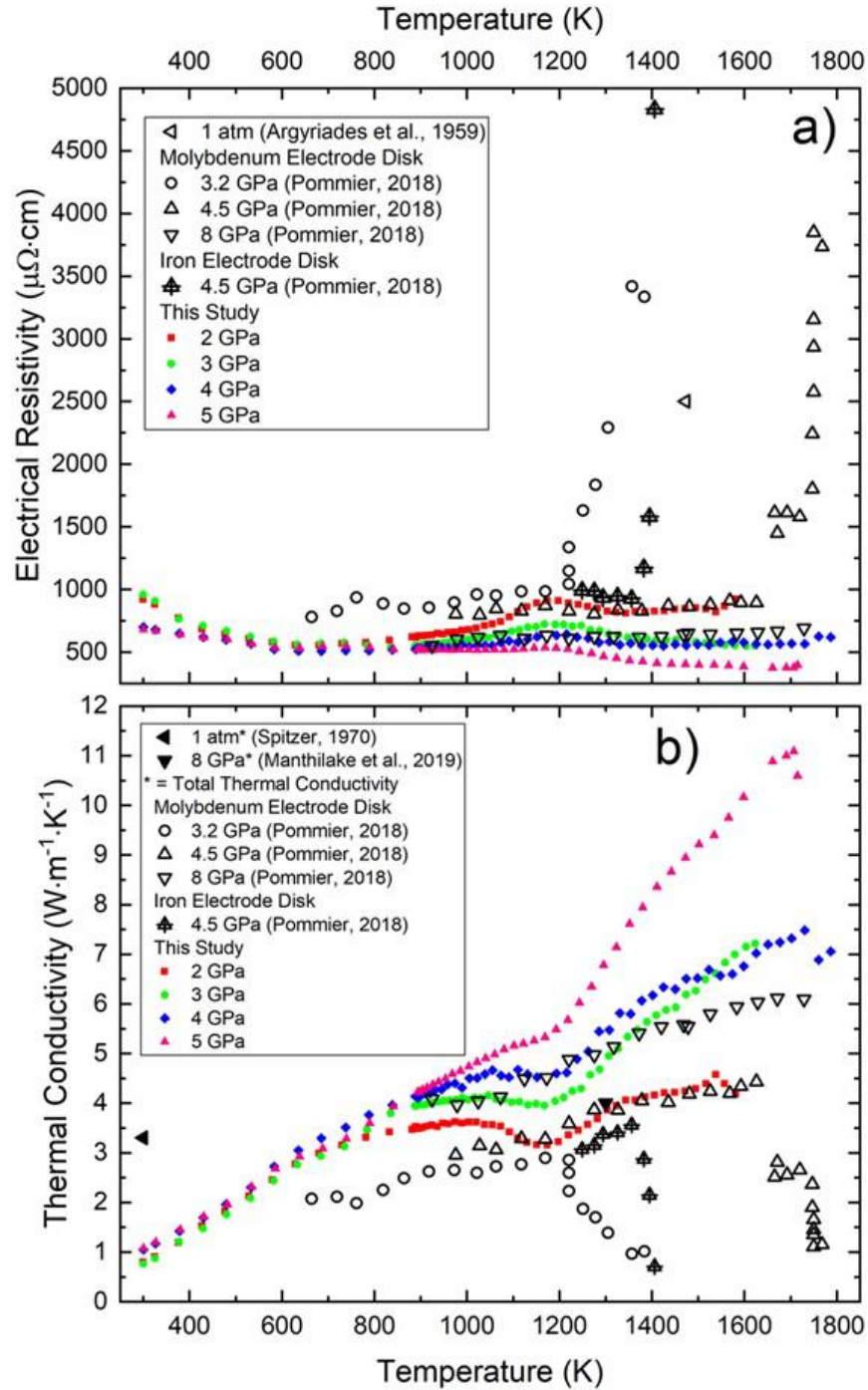


Figure 4.4: (a) Measured electrical resistivity of FeS from this study are compared to two previous studies. The data point by Argyriades et al. (1959) is a measurement of FeS in the liquid state. The abrupt increasing trend of values measured by Pommier (2018) was reported to be indicative of transitions from a ‘solid- to liquid-

dominated regime'. Data by Manthilake et al. (2019) are not shown for scaling purposes ($>10^4 \mu\Omega\cdot\text{cm}$); (b) Calculated electronic components of thermal conductivity of FeS from this study are compared to previous three previous studies. The data point by Spitzer (1970) is an unpublished report of a measurement of the total thermal conductivity, while the data point by Manthilake et al. (2019) is an estimated value of the total thermal conductivity.

refers to the ability of a molten sample to displace outwards from sample container and typically move in the direction of the TCs. This can happen by liquid seeping around the electrode or diffusing through and mixing with the electrodes. The molten samples are then capable of contaminating and mixing with the TCs, which can result in measured voltages larger than expected.

Pommier (2018) made measurements of ρ at ~ 1620 K at 4.5 GPa and ~ 1730 K at 8 GPa. Estimates of the melting T of FeS extrapolated to 4.5 GPa and 8 GPa is ~ 1600 K and 1700 K, respectively (Boehler, 1992). If the sample is interpreted as being entirely molten, these measurements and those preceding them at lower T indicate no distinct features of ρ upon melting – in agreement with our observations. Instead of W electrode disks used in this study, Pommier (2018) used molybdenum (Mo) electrodes for these two measurements because the contamination effects on the sample, which act to increase electrical resistance, are small. This is supported by sample analyses of the 8 GPa experiment that showed electrode contamination of ~ 20 wt.% with no perceptible influence on the T-dependent trend of ρ . Since contamination effects are small, then liquid confinement can explain this discrepancy. Contamination by the TCs in the 4.5 GPa and 8 GPa experiments were ~ 3 and 0.4 wt.%, respectively. The larger TC contamination may be indicative of reduced TC integrity, which can explain the large measurements of ρ at 4.5 GPa but not at 8 GPa.

While post-experiment analyses of the sample were not reported, liquid confinement could also explain the measurements at 3.2 GPa that show a very similar increase. The estimated melting T at 3.2 GPa is ~ 1565 K (Boehler, 1992) and is noticeably higher than T range of the large values of ρ (~ 1220 K to 1390 K). If this region represents a transition

from a solid- to liquid-dominated regime, it fits within our interpretation that this is incongruent melting due to the presence of non-stoichiometric compositions. Moreover, if partial melting occurred within this T region, the explanation of liquid confinement becomes plausible. A similar trend was reported for a second experiment at 4.5 GPa using Fe electrode disks, with an abrupt increase of ρ at ~ 1380 K. The few measurements prior to this T appear in good agreement with the 4.5 GPa experiment using Mo electrode disks; however, there is ~ 300 K difference in the solid-liquid regime transition T that was not addressed.

Manthilake et al. (2019) suggested that the discrepancy between their measured results and the results by Pommier (2018) could be explained by the presence of impurities or from reactions forming Fe-S alloys with higher Fe contents. Manthilake et al. (2019) also reported a melting T between 1400 K and 1500 K at 8 GPa, which is approximately 200-300 degrees below the estimate based on FeS phase diagram they cited (Urakawa et al., 2004). This T is well above estimates of the P-dependent eutectic T (Kubaschewski, 1982; Fei et al., 1997; Li and Fei, 2003; Morard et al., 2007), which suggests that Fe-FeS eutectic-related partial melting may not be responsible. If the FeS sample is exceptionally consistent with respect to stoichiometry, the observed melting may instead indicate the small solidus-liquidus region reported in some binary Fe-S phase diagrams (e.g. Kubaschewski, 1982). Alternatively, presence of other impurities could lower the melting T. Manthilake et al. (2019) noted their compressed FeS sample oxidized during heating based on the emergence of magnetite x-ray diffraction peaks. It is unclear about the total extent of reaction on the sample and compound formation, which could affect the melting T and transport properties.

Figure 4.4b shows calculated values of κ of FeS up to 5 GPa and 1785 K from this study compared to previous studies (Spitzer, 1970; Pommier, 2018; Manthilake et al., 2019). The P- and T-dependent trend in the solid state of values calculated by Pommier (2018) agree with our observations: κ increased with increasing P and T. However, the magnitude of κ at 3.2 GPa and 4.5 GPa decrease abruptly because of the corresponding increase of ρ as explained previously (Figure 4.4a). The value of κ shown by Manthilake et al. (2019) is after the addition of their estimate of the phonon contribution and thus

represents total κ . Without the additional contribution, the value of electronic κ at 1300 K is on the order of $\sim 10^{-2} \text{ W}\cdot\text{m}^{-1}\cdot\text{K}^{-1}$. Spitzer (1970) reported a measured value of $3.3 \text{ W}\cdot\text{m}^{-1}\cdot\text{K}^{-1}$ of total κ of FeS at ambient P and T. With the value of ρ of FeS exceeding $10^4 \mu\Omega\cdot\text{cm}$ (Kobayashi et al., 2001), the electronic κ is a minor contribution ($\kappa < 0.07 \text{ W}\cdot\text{m}^{-1}\cdot\text{K}^{-1}$ via (4.1)) to the total κ at the conditions. However, as both Pommier (2018) and our results show, the contribution by the electronic κ increased by as much as two orders of magnitude as a result of increasing P and T and implies thermal transport becomes significantly more reliant on the electronic component.

The approach taken by Manthilake et al. (2019) provided a comparable estimate to the values by Spitzer (1970) and Pommier (2018), although the differences in P and T conditions are significant (Figure 4.4b). Calculation of the contribution by phonon interactions to the total κ requires knowing the scattering strengths and probabilities of phonon-phonon, phonon-electron, and phonon-lattice defects (Klemens and Williams, 1986). These P- and T-dependent variables may not be adequately estimated through their fitting parameters of total κ end-members (Fe, conductor – S₂, insulator) and stoichiometric compounds (FeS and FeS₂, semiconductors) of the Fe-S system simply because those detailed interactions are unknown. The approach by Manthilake et al. (2019) assumed no P-dependency and applied a T-dependency that has shown reasonably good fits for alloys that retain a metallic character (Klemens and Williams, 1986). It is unclear whether the same T-dependency holds for FeS and FeS₂ that have semiconducting behaviour and stronger covalent bonding. While total κ is expected to increase with decreasing S content, which is consistent with their approach, we question how reliant the estimate by Manthilake et al. (2019) is given the variability of the electrical and thermal behaviour of the Fe-S system.

The ideal situation is for measurements of total κ of FeS to be made at high P and T up to and in the liquid state; however, these measurements are more difficult to perform than measurements of ρ because of the necessity for stable thermal gradients. If made, the measurements would allow for calculation of the phonon contribution to κ , as well as the P- and T-dependencies. These measurements may also help constrain the value of L in Eqn (4.1) for solid and liquid FeS. For instance, if measurements of total κ are exceeded

by calculated estimates of electronic κ , then the Sommerfeld value of L overestimates the electronic contribution.

4.4.2 Implications for Heat Flow in the Core of Ganymede

Despite the inherent non-uniqueness of solutions, interior structure models using density, moment-of-inertia factor and magnetic field measurements as major constraints have suggested that Ganymede is differentiated, possessing an Fe-FeS core surrounded by a silicate mantle and outer-most layer of ice (Sohl et al., 2002). With assumed internal dynamo action in Ganymede, focus is given to the lower mantle and core. Heat flow at the CMB and adiabatic heat flow in the core of planetary bodies are dependent on temperature, composition, and material properties models of the interiors, all of which are prone to large uncertainties (Lay et al., 2008). The mineral phases, grain sizes, water abundance, and viscosity of the overlying mantle are not well known nor is the T distribution of Ganymede's interior in the past or present. Similarly, distribution and abundance of radiogenic heat sources on either side of the CMB is uncertain because the bulk composition of Ganymede is not precisely known (e.g. Hauck et al., 2006; Rückriemen et al., 2018).

Equations of state are used to predict the state of materials under core-like conditions, which are useful when specific P-T conditions are imposed that do not have reliable measurements. The parameters involved often are taken as values at ambient conditions that are then extrapolated. This may lead to over- or under-estimates of the state of a material in the absence of reliable measurements, especially for materials that exhibit high P-T atomic structural, electronic, and magnetic transitions (e.g. FeS). This uncertainty is further complicated since material composition of either side of the CMB is not well known. Thermal transport properties of materials expected to be at the CMB are strongly dependent on the P-T state conditions, thus affecting the heat flux out of the core. Adiabatic conductive heat flow inside the core is dependent on core composition. In Ganymede, the composition of the core will affect crucial parameters of the adiabatic heat flow, such as the core radius, density, thermal conductivity, thermal expansivity, heat capacity, compressibility, and gravitational acceleration.

The P conditions of Ganymede's core are ~5-11 GPa from the CMB to the center of the satellite, with estimates of the T of the core ranging from ~1250 K up to ~2100 K at the CMB (Sohl et al., 2002; Hauck et al., 2006; Bland et al., 2008; Kimura et al., 2009; Rückriemen et al., 2018). The radius of Ganymede's core (~700 – 1200 km) is dependent on S content, with increasing S content associated with larger core radii (Anderson et al., 1996; Sohl et al., 2002; Rückriemen et al., 2018). We calculated the adiabatic conductive heat flow (Q_a) on the core side of the CMB for a range of core radii (r) and a narrow span of T using Eqn. (4.5) below:

$$Q_a = -4\pi r^2 \kappa \left(\frac{\partial T}{\partial r} \right)_a \quad (4.5)$$

where $(\partial T/\partial r)_a$ is the adiabatic thermal gradient adopted from Breuer et al. (2015). As shown in the Supporting Information section, values of ρ were interpolated from our measurements at 5 GPa (Figure 4.2a) for the T range and used to calculate κ via Eqn. (4.1). The interpolated values of κ were then substituted in Eqn. (4.5).

We recognize there are uncertainties on each parameter used to calculate $(\partial T/\partial r)_a = \alpha g T / c_p$, where α is the coefficient of thermal expansion, g is gravitational acceleration, and c_p is isobaric heat capacity, in the core as well as on estimates of the heat flow through the CMB. But if we accept values for α , g , T and c_p commonly used in the literature and as reported in Breuer et al. (2015) to calculate the adiabatic thermal gradient, we show in Figure 4.5 Q_a for an entirely molten FeS core with a radius between 700 and 1200 km and a CMB T from 1600 and 1700 K and P of 5 GPa. The T range for our calculations was selected because it allows for a liquid FeS core and is based on values of ρ contained within our measurements. Lower T calculations are viable for compositions near the Fe-FeS eutectic since it will allow for a liquid core instead of a solid one as would be the case for pure FeS. Extrapolation of our ρ at 5 GPa to higher T (~2000 K; $\Delta T = 300$ K) would be too uncertain and would decrease our confidence in those estimates. Our estimates of Q_a range from ~18 GW, for a CMB T of 1600 K and core radius of 700 km, up to ~31 GW, for a CMB T of 1700 K and core radius of 1200 km. Estimates of the heat flow through the CMB are shown for comparison. A heat flux of 1 mW/m² through the CMB is too low for thermal convection to be permissible since

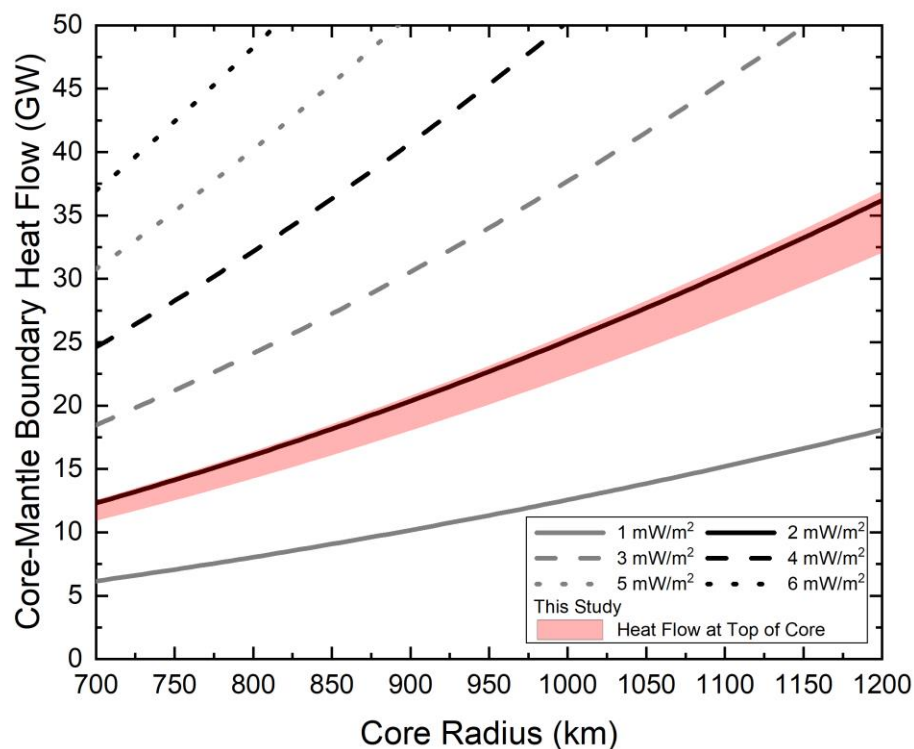


Figure 4.5: Calculated adiabatic heat flow at the core-mantle boundary (CMB) of Ganymede of a fully molten FeS core. The dashed lines represent estimates of the heat flow out of the core (Hauck et al., 2006; Kimura et al., 2009; Rückriemen et al., 2015; 2018). Dark lines represent even-numbered core heat fluxes and light lines represent odd-numbered core heat fluxes. The shaded red region represents all values of calculated heat flow values on the core-side of the CMB. The CMB temperature ranges from 1600 K at the bottom to 1700 K at the top of the shaded region of this study. Propagated uncertainty on the calculations range from ~1-1.5% of the reported values.

conductive heat transport can carry the heat load. However, increasing the heat flux to 2 mW/m², thermal conduction alone may not be able to transport enough heat to account for what escapes the core through the CMB. Thus, for a heat flux of 2 mW/m², thermal convection is a possible active thermal transport mechanism and dynamo power source in Ganymede's core. As the heat flux through the CMB increases to 3 mW/m², the reliance

on thermal convection to transport heat out of the core also increases. In this scenario, our estimates show thermal convection could transport up to one-third of the heat that leaves the core. Estimates of the heat flux out of the core through the CMB of Ganymede range from $\sim 1\text{-}6 \text{ mW/m}^2$ (Hauck et al., 2006; Kimura et al., 2009; Rückriemen et al., 2015; 2018), suggesting that thermal convection is permissible for the majority of this range. However, we note that with respect to pressure and S contents, our estimates represent a lower bound of heat flow within the T ranges used.

At isothermal conditions with increasing P, it is expected that ρ will continue to decrease, and calculated κ and Q_a will increase. Thus, for $P > 5 \text{ GPa}$ at the CMB, thermal conduction will be a more efficient thermal transport mechanism. For thermal convection to be permissible, the heat flux through the CMB would need to tend towards the larger estimate values. Given that pure Fe is an electrical conductor and FeS an electrical semiconductor, a reasonable expectation is that ρ will decrease as the S content decreases towards the Fe-rich end of the system. This general trend was observed by Pommier (2018) for the Fe-FeS system. Since Ganymede's core is expected to have S contents below 36.5 wt.%, the same expectation of more efficient core thermal conduction and larger heat flux through the CMB is proposed.

The magnitude of an impurity effect expected for the addition of S to pure Fe (Suehiro et al., 2017) and delineation between a particular composition behaving more like an electrical conductor (Fe-rich) or semiconductor (FeS-rich) at high P and T are either uncertain or unknown. The contributions to ρ via the impurity effect due to S presence in pure Fe decreased as a function of P (Suehiro et al., 2017) and measurements of ρ of several Fe-Si alloys suggest that that impurity effect may also decrease as a function of increasing T (Silber et al., 2019; Berrada et al., 2020). Matthiessen's rule has often been used to model and predict the impurity effect on ρ for metallic alloys. The rule asserts that the impurity effect is an additive T-independent contribution to the ρ of a pure metal for all T in the solid state. However, this rule is not valid for many systems. For example, Berrada et al. (2020) recently showed for Fe-Si alloys with Si up to 17 wt.% that such an impurity contribution term is dependent on T and in general showed a negative dependence. As well, their results showed that the overall T-dependent trends of ρ

increasingly deviated from that of pure Fe with increasing Si content at all experimental P in both solid and liquid states. In other words, the Fe-FeS system may not have constant T-independent impurity effects on ρ , but may have non-linear impurity content-dependent effects. Both of these effects make interpolating the values of ρ for all S contents relevant to Ganymede's core between Fe and FeS endmembers problematic until investigated further.

4.5 Conclusion

The presence of impurity elements, such as S, in the cores of terrestrial planets and moons is of considerable interest due to their potentially significant effects on core transport properties, which have direct influence over dynamo and thermal evolution. This study provides detailed measurements of the ρ of FeS in solid and molten states at pressures from 2-5 GPa in a cubic anvil press with well-controlled sample geometry. It was observed that ρ is lower than previous works at all similar P and T conditions. The electronic κ was calculated via the Wiedemann-Franz Law using the measured values of ρ , and in turn used to evaluate the heat flow on the core-side of the CMB of Ganymede's S-rich core. The results, which represent a lower bound estimate of core heat flow, show that thermal convection may be permissible and thus act as a geodynamo energy source.

4.6 References

- Alfè, D., Gillan, M.J. and Price, G.D. 2002. Composition and temperature of the Earth's core constrained by combining ab initio calculations and seismic data. *Earth and Planetary Science Letters*. 195(1-2): 91-98. DOI: 10.1016/S0012-821X(01)00568-4
- Allègre, C., Poirier, J., Humler, E. and Hofmann, A. 1995. The chemical composition of the Earth. *Earth and Planetary Science Letters*, 134(3-4): 515-526. DOI: 10.1016/0012-821X(95)00123-T
- Anderson, J.D., Lau, E.L., Sjogren, W.L., Schubert, G. and Moore, W.B. 1996. Gravitational constraints on the internal structure of Ganymede. *Nature*. 384(6609): 541-543. DOI: 10.1038/384541a0

- Argyriades, D., Derge, G. and Pound, G.M. 1959. Electrical conductivity of molten FeS. *Transactions of the Metallurgical Society of AIME*. 215: 909-912.
- Badro, J., Côté, A.S. and Brodholt, J.P. 2014. A seismologically consistent compositional model of Earth's core. *Proceedings of the National Academy of Sciences of the United States of America*. 111(21): 7542-7545. DOI: 10.1073/pnas.1316708111
- Berrada, M., Secco, R.A. and Yong, W. 2018. Decreasing electrical resistivity of gold along the melting boundary up to 5 GPa. *High Pressure Research*. 38(4): 367-376. DOI: 10.1080/08957959.2018.1493476
- Berrada, M., Secco, R.A., Yong, W. and Littleton, J.A.H. 2020. Electrical resistivity measurements of Fe-Si with implications for the early lunar dynamo. *Journal of Geophysical Research – Planets*. 125(7): e2020JE006380. DOI: 10.1029/2020JE006380
- Bland, M.T., Showman, A.P. and Tobie, B. 2008. The production of Ganymede's magnetic field. *Icarus*. 198(2): 384-399. DOI: 10.1016/j.icarus.2008.07.011
- Boehler, R. 1992. Melting of the Fe-FeO and the Fe-FeS systems at high pressure: Constraints on core temperatures. *Earth and Planetary Science Letters*. 111(2-4): 217-227. DOI: 10.1016/0012-821X(92)90180-4
- Brett, R. and Bell, P.M. 1969. Melting relations in the Fe-rich portion of the system Fe-FeS at 30 kb pressure. *Earth and Planetary Science Letters*. 6(6): 479-482. DOI: 10.1016/0012-821X(69)90119-8
- Breuer, D., Rückriemen, T. and Spohn, T. 2015. Iron snow, crystal floats, and inner-core growth: modes of core solidification and implications for dynamos in terrestrial planets and moons. *Progress in Earth and Planetary Science*. 2(39): 1-26. DOI: 10.1186/s40645-015-0069-y
- Buffett, B. 2003. The thermal state of Earth's core. *Science*, 299(5613): 1675-1677. DOI: 10.1126/science.1081518

- Buffett, B. 2007. Core-mantle interactions. *In* Treatise on Geophysics, Vol. 8. *Edited by* Peter Olson and Gerald Schubert. Elsevier Ltd., Waltham, Mass. pp. 345-358.
- Buono, A.S. and Walker, D. 2011. The Fe-rich liquidus in the Fe-FeS system from 1 bar to 10 GPa. *Geochemica et Cosmochemica Acta*. 75(8): 2072-2087. DOI: 10.1016/j.gca.2011.01.030
- Chen, B., Gao, L., Leinenweber, K., Wang, Y., Sanehira, T. and Li, J. 2008a. In situ investigation of high-pressure melting behavior in the Fe-S system using synchrotron X-ray radiography. *High Pressure Research*. 28(3): 315-326. DOI: 10.1080/08957950802318883
- Chen, B., Li, J. and Hauck II, S.A. 2008b. Non-ideal liquidus curve in the Fe-S system and Mercury's snowing core. *Geophysical Research Letters*. 35: L07201. DOI: 10.1029/2008GL033311
- Christensen, U.R. 2015. Iron snow dynamo models for Ganymede. *Icarus*. 247: 248-259. DOI: 10.1016/j.icarus.2014.10.024
- Davies, C.J. and Pommier, A. 2018. Iron snow in the Martian core?. *Earth and Planetary Science Letters*. 481(): 189-200. DOI: 10.1016/j.epsl.2017.10.026
- Ezenwa I.C. and Secco, R.A. 2017a. Electronic transition in solid Nb at high pressure and temperature. *Journal of Applied Physics*. 121: 225903. DOI: 10.1063/1.4985548
- Ezenwa I.C. and Secco, R.A. 2017b. Constant electrical resistivity of Zn along the melting boundary up to 5 GPa. *High Pressure Research*. 37(3): 319-333. DOI: 10.1080/08957959.2017.1340473
- Ezenwa I.C. and Secco, R.A. 2017c. Invariant electrical resistivity of Co along the melting boundary. *Earth and Planetary Science Letters*. 474: 120-127. DOI: 10.1016/j.epsl.2017.06.032

Ezenwa, I.C., Secco, R.A., Yong, W., Pozzo, M. and Alfé, D. 2017. Electrical resistivity of solid and liquid Cu up to 5 GPa: Decrease along the melting boundary. *Journal of Physics and Chemistry of Solids*. 110: 386-393. DOI: 10.1016/j.jpcs.2017.06.030

Faber, T. 1972. *Theory of Liquid Metals*. Cambridge University Press, Cambridge, U.K.

Fei, Y., Bertka, C.M. and Finger, L.W. 1997. High-pressure iron-sulfur compound, Fe₃S, and melting relations in the Fe-FeS system. *Science*. 275(5306): 1621-1623.

Fei, Y., Prewitt, C.T., Mao, H-K. and Bertka, C.M. 1995. Structure and density of FeS at high pressure and high temperature and the internal structure of Mars. *Science*. 268(5219): 1892-1894. DOI: 10.1126/science.268.5219.1892

Franz, R. and Wiedemann, G. 1853. Ueber die Wärme-Leitungsfähigkeit der Metalle. *Annalen der Physik*. 165(8): 497-531. DOI: 10.1002/andp.18531650802

Getting, I.C. and Kennedy, G.C. 1970. Effect of pressure on the emf of chromel-alumel and platinum-platinum 10% rhodium thermocouples. *Journal of Applied Physics*. 41(11): 4552-4562. DOI: 10.1063/1.1658495

Gomi, H. and Hirose, K. 2015. Electrical resistivity and thermal conductivity of hcp Fe-Ni alloys under high pressure: Implications for thermal convection in the Earth's core. *Physics of the Earth and Planetary Interiors*. 247: 2-10. DOI: 10.1016/j.pepi.2015.04.003

Gomi, H. and Yoshino, T. 2018. Impurity resistivity of fcc and hcp Fe-based alloys: Thermal stratification at the top of the core of super-Earths. *Frontiers in Earth Science*. 6: 217. DOI: 10.3389/feart.2018.00217

Hauck II, S.A., Aurnou, J.M. and Dombard, A.J. 2006. Sulfur's impact on core evolution and magnetic field generation on Ganymede. *Journal of Geophysical Research: Planets*. 111: E09008. DOI: 10.1029/2005JE002557

Helfrich, G. and Kaneshima, S. 2004. Seismological constraints on core composition from Fe-O-S liquid immiscibility. *Science*, 306(5705): 2239-2242. DOI: 10.1126/science.1101109

- Hirose, K., Labrosse, S. and Hernlund, J. 2013. Composition and state of the core. *Annual Review of Earth and Planetary Sciences*. 41:657-691. DOI: 10.1146/annurev-earth-050212-124007
- Jephcoat, A.P., Mao, H.K. and Bell, P.M. 1986. Static compression of iron to 78 GPa with rare gas solids as pressure-transmitting media. *Journal of Geophysical Research*. 91(B5): 4677-4684. DOI: 10.1029/JB091iB05p04677
- Karunakaran, C., Vijayakumar, V., Vaidya, S.N., Kunte, N.S. and Suryanarayana, S. 1980. Effect of pressure on electrical resistivity and thermoelectric power of FeS. *Materials Research Bulletin*. 15(2): 201-206. DOI: 10.1016/0025-5408(80)90120-8
- Khan, A. and Connolly, J.A.D. 2008. Constraining the composition and thermal state of Mars from inversion of geophysical data. *Journal of Geophysical Research: Planets*. 113: E07003. DOI: 10.1029/2007JE002996
- Khan, A., Liebske, C., Rozel, A., Rivoldini, A., Nimmo, F., Connolly, J.A.D., Plesa, A.-C. and Giardini, D. 2018. A geophysical perspective on the bulk composition of Mars. *Journal of Geophysical Research: Planets*. 123(2): 575-611. DOI: 10.1002/2017JE005371
- Kimura, J., Nakagawa, T. and Kurita, K. 2009. Size and compositional constraints of Ganymede's metallic core for driving an active dynamo. *Icarus*. 202(1): 216-224. DOI: 10.1016/j.icarus.2009.02.026
- King, H.E. and Prewitt, C.T. 1982. High-pressure and high-temperature polymorphism of iron sulfide (FeS). *Acta Crystallographica Section B: Structural Science, Crystal Engineering and Materials*. B38(7): 1877-1887. DOI: 10.1107/S0567740882007523
- Klemens, P.G. and Williams, R.K. 1986. Thermal conductivity of metals and alloys. *International Metals Reviews*. 31(5): 197-215. DOI: 10.1179/imtr.1986.31.1.197
- Kobayashi, H., Kamimura, T., Ohishi, Y., Takeshita, N. and Mōri, N. 2005. Structural and electrical properties of stoichiometric FeS compounds under higher pressure at low temperature. *Physical Review B*. 71(1): 014110. DOI: 10.1103/PhysRevB.71.014110

- Kobayashi, H., Takeshita, N., Mōri, N., Takahashi, H. and Kamimura, T. 2001. Pressure-induced semiconductor-metal-semiconductor transitions in FeS. *Physical Review B*. 63(11): 115203. DOI: 10.1103/PhysRevB.63.115203
- Kubaschewski, I. 1982. Iron-sulphur. *In IRON – Binary Phase Diagrams*. Springer-Verlag Berlin Heidelberg GmbH, Düsseldorf, Germany. pp. 125-128.
- Kumar, G., Prasad, G. and Pohl, R. 1993. Experimental determinations of the Lorenz number. *Journal of Materials Science*. 28(16): 4261-4272. DOI: 10.1007/BF01154931
- Kusaba, K., Syono, Y., Kikegawa, T. and Shimomura, O. 1998. High pressure and temperature behavior of FeS. *Journal of Physics and Chemistry of Solids*. 59(6-7): 945-950. DOI: 10.1016/S0022-3697(98)00015-8
- Labrosse, S. and Macouin, M. 2003. The inner core and the geodynamo. *Comptes Rendus Geoscience*, 335(1): 37-50. DOI: 10.1016/S1631-0713(03)00013-0
- Lay, T., Hernlund, J. and Buffett, B. 2008. Core-mantle boundary heat flow. *Nature Geoscience*, 1(1): 25-32. DOI: 10.1038/ngeo.2007.44
- Li, J. and Agee, C.B. 1996. Geochemistry of mantle-core differentiation at high pressure. *Nature*. 381(6584): 686-689. DOI: 10.1038/381686a0
- Li, J. and Fei, Y. 2003. Experimental constraints on core composition. *In Treatise on Geochemistry, Vol. 2. Edited by Robert Carlson, Heinrich Holland and Karl Turekian*. Elsevier Ltd., Waltham, Mass. pp. 521-546.
- Lin, J-F., Heinz, D.L., Campbell, A.J., Devine, J.M., Mao, W.L. and Shen, G. 2002. Iron-nickel alloy in the Earth's core. *Geophysical Research Letters*. 29(10): 109-1. DOI: 10.1029/2002GL015089
- Lin, J-F., Struzhkin, V.V., Sturhahn, W., Huang, E., Zhao, J., Hu, M.Y., Alp, E.E., Mao, H., Boctor, N. and Hemley, R.J. 2003. Sound velocities of iron-nickel and iron-silicon alloys at high pressures. *Geophysical Research Letters*. 30(21): SDE 11-1. DOI: 10.1029/2003GL018405

- Littleton, J.A.H., Secco, R.A. and Yong, W. 2018. Decreasing electrical resistivity of silver along the melting boundary up to 5 GPa. *High Pressure Research*. 38(2): 99-106. DOI: 10.1080/08957959.2018.1435786
- Littleton, J.A.H., Secco, R.A., Yong, W and Berrada, M. 2019. Electrical resistivity and thermal conductivity of W and Re up to 5 GPa and 2300 K. *Journal of Applied Physics*. 125(13): 135901. DOI: 10.1063/1.5066103
- Manthilake, G., Chantel, J., Monteux, J., Andrault, D., Bouhifd, M.A., Casanova, N.B., Boulard, E., Guignot, N., King, A. and Itie, J.P. 2019. Thermal conductivity of FeS and its implications for Mercury's long-sustaining magnetic field. *Journal of Geophysical Research: Planets*. 124(9): 2359-2368. DOI: 10.1029/2019JE005979
- Mao, H.K., Wu, Y., Chen, L.C., Shu, J.F. and Jephcoat, A.P. 1990. Static compression of iron to 300 GPa and Fe_{0.8}Ni_{0.2} alloy to 260 GPa: Implications for composition of the core. *Journal of Geophysical Research: Solid Earth*. 95(B13): 21737-21742.
- Mao, W.L., Campbell, A.J., Heinz, D.L. and Shen, G. 2006. Phase relations of Fe-Ni alloys at high pressure and temperature. *Physics of the Earth and Planetary Interiors*. 155(1-2): 146-151. DOI: 10.1016/j.pepi.2005.11.002
- Martorell, B., Brodholt, J., Wood, I.G. and Vočadlo, L. 2013. The effect of nickel on the properties of iron at the conditions of Earth's inner core: Ab initio calculations of seismic wave velocities of Fe-Ni alloys. *Earth and Planetary Science Letters*. 365: 143-151. DOI: 10.1016/j.epsl.2013.01.007
- Martorell, B., Brodholt, J., Wood, I.G. and Vočadlo, L. 2015. The elastic properties and stability of fcc-Fe and fcc-FeNi alloys at inner-core conditions. *Geophysical Journal International*. 202(1): 94-101. DOI: 10.1093/gji/ggv128
- McDonough, W. 2003. Compositional Model for the Earth's Core. *In* *Treatise on Geochemistry, Vol. 2. Edited by Robert Carlson, Heinrich Holland and Karl Turekian.* Elsevier Ltd., Waltham, Mass. pp. 547-568.

- McSween Jr, H.Y. and Huss, G. 2010. Solar system and cosmic abundances: elements and isotopes. *In Cosmochemistry*. Cambridge University Press, Cambridge, U.K. pp. 85-119.
- Mizutani, U. 2004. *Introduction to the Electron Theory of Metals*. Cambridge University Press, Cambridge, U.K.
- Morard, G., Andrault, D., Guignot, N., Siebert, J., Gaston, G. and Antonangeli, D. 2011. Melting of Fe-Ni-Si and Fe-Ni-S alloys at megabar pressures: Implications for the core-mantle boundary temperature. *Physics and Chemistry of Minerals*. 38(10): 767-776. DOI: 10.1007/s00269-011-0449-9
- Morard, G., Sanloup, C., Fiquet, G., Mezouar, M., Rey, N., Poloni, R. and Beck, P. 2007. Structure of eutectic Fe-FeS melts to pressures up to 17 GPa: Implications for planetary cores. *Earth and Planetary Science Letters*. 262(1-2): 128-139. DOI: 10.1016/j.epsl.2007.09.009
- Mori, Y., Ozawa, H., Hirose, K., Sinmyo, R., Tateno, S., Morard, G. and Ohishi, Y. 2017. Melting experiments on the Fe-Fe₃S system to 254 GPa. *Earth and Planetary Science Letters*. 464: 135-141. DOI: 10.1016/j.epsl.2017.02.021
- Nimmo, F. 2015. Energetics of Earth's core. *In Treatise on Geophysics*, Vol. 8., 2nd Ed. *Edited by Peter Olson and Gerald Schubert*. Elsevier Ltd., Waltham, Mass. pp. 27-56.
- Olson, P. 2016. Mantle control of the geodynamo: Consequences of top-down regulation. *Geochemistry, Geophysics, Geosystems*. 17(5): 1935-1956. DOI: 10.1002/2016GC006334
- Poirier, J. 1994. Light elements in the Earth's outer core: A critical review. *Physics of the Earth and Planetary Interiors*, 85(3-4): 319-337. DOI: 10.1016/0031-9201(94)90120-1
- Poirier, J. 2000. Transport properties. *In Introduction to the Physics of the Earth's Interior*, 2nd Ed. Cambridge University Press, Cambridge, U.K. pp. 156-220.

- Pommier, A. 2018. Influence of sulfur on the electrical resistivity of a crystallizing core in small terrestrial bodies. *Earth and Planetary Science Letters*. 496: 37-46. DOI: 10.1016/j.epsl.2018.05.032
- Pommier, A., Laurenz, V., Davies, C.J. and Frost, D.J. 2018. Melting phase relations in the Fe-S and Fe-S-O systems at core conditions in small terrestrial bodies. *Icarus*. 306: 150-162. DOI: 10.1016/j.icarus.2018.01.021
- Rivoldini, A. and Van Hoolst, T. 2013. The interior structure of Mercury constrained by the low-degree gravity field and the rotation of Mercury. *Earth and Planetary Science Letters*. 377-379: 62-72. DOI: 10.1016/j.epsl.2013.07.021
- Rivoldini, A., Van Hoolst, T. and Verhoeven, O. 2009. The interior structure of Mercury and its core sulfur content. *Icarus*. 201(1): 12-30. DOI: 10.1016/j.icarus.2008.12.020
- Rossiter, P.L. 1987. *The electrical resistivity of metals and alloys*. Cambridge University Press, Cambridge, U.K.
- Rubie, D., Nimmo, F. and Melosh, H. 2007. Formation of Earth's core. *In* *Treatise on Geophysics*, Vol. 9. *Edited by* David Stevenson and Gerald Schubert. Elsevier Ltd., Waltham, Mass. pp. 51-90.
- Rückriemen, T., Breuer, D. and Spohn, T. 2015. The Fe snow regime in Ganymede's core: A deep-seated dynamo below a stable snow zone. *Journal of Geophysical Research: Planets*. 120(6): 1095-1118. DOI: 10.1002/2014JE004781
- Rückriemen, T., Breuer, D. and Spohn, T. 2018. Top-down freezing in a Fe-FeS core and Ganymede's present-day magnetic field. *Icarus*. 307: 172-196. DOI: 10.1016/j.icarus.2018.02.021
- Sakai, T., Ohtani, E., Hirao, N. and Ohishi, Y. 2011. Stability field of the hcp-structure for Fe, Fe-Ni, and Fe-Ni-Si alloys up to 3 Mbar. *Geophysical Research Letters*. 38(9): L09302. DOI: 10.1029/2011GL047178

Sanloup, C., Jambon, A. and Gillet, P. 1999. A simple chondritic model of Mars. *Physics of the Earth and Planetary Interiors*. 112(1-2): 43-54. DOI: 10.1016/S0031-9201(98)00175-7

Saxena, S. and Eriksson, G. 2015. Thermodynamics of Fe-S at ultra-high pressure. *CALPHAD: Computer Coupling of Phase Diagrams and Thermochemistry*. 51: 202-205. DOI: 10.1016/j.calphad.2015.09.009

Schloessin, H. and Lenson, F. 1989. Measurement and modeling of the temperature field in high-pressure and high-temperature experiments in cubes with internal heating. *High Temperatures-High Pressures*. 2: 275-285.

Schubert, G., Ross, M.N., Stevenson, D.J. and Spohn, T. 1988. Mercury's thermal history and the generation of its magnetic field. *Mercury*. 429-460.

Secco, R.A. 1995. High p,T physical property studies of Earth's interior: Thermoelectric power of solid and liquid Fe up to 6.4 GPa. *Canadian Journal of Physics*. 73: 287-294. DOI: 10.1139/p95-040

Secco, R.A. 2017. Thermal conductivity and Seebeck coefficient of Fe and Fe-Si alloys: Implications for variable Lorenz number. *Physics of the Earth and Planetary Interiors*. 265: 23-34. DOI: 10.1016/j.pepi.2017.01.005

Silber, R.E., Secco, R.A. and Yong, W. 2017. Constant electrical resistivity of Ni along the melting boundary up to 9 GPa. *Journal of Geophysical Research: Solid Earth*. 122(7): 5064-5081. DOI: 10.1002/2017JB014259

Silber, R.E., Secco, R.A., Yong, W. and Littleton, J.A.H. 2018. Electrical resistivity of liquid Fe to 12 GPa: Implications for heat flow in core of terrestrial bodies. *Scientific Reports*. 8(1): 1-9. DOI: 10.1038/s41598-018-28921-w

Silber, R.E., Secco, R.A., Yong, W. and Littleton, J.A.H. 2019. Heat flow in Earth's core from invariant electrical resistivity of Fe-Si on the melting boundary to 9 GPa: Do light elements matter?. *Journal of Geophysical Research: Solid Earth*. 124(6): 5521-5543. DOI: 10.1029/2019JB017375

Sohl, F. and Schubert, G. 2007. Interior structure, composition, and mineralogy of the terrestrial planets. *In* *Treatise on Geophysics, Vol. 2. Edited by* Tilman Spohn and Gerald Schubert. Elsevier Ltd., Waltham, Mass. pp. 27-68.

Sohl, F., Spohn, T., Breuer, D. and Nagel, K. 2002. Implications from Galileo observations on the interior structure and chemistry of the Galilean satellites. *Icarus*. 157(1): 104-119. DOI: 10.1006/icar.2002.6828

Spitzer, D.P. 1970. Lattice thermal conductivity of semi-conductors: A chemical bond approach. *Journal of Physics and Chemistry of Solids*. 31(1): 19-40. DOI: 10.1016/0022-3697(70)90284-2

Štemprok, M. 1971. The iron-tungsten-sulphur system and its geological application. *Mineralium Deposita*. 6(4): 302-312. DOI: 10.1007/BF00201888

Suehiro, S., Ohta, K., Hirose, K., Morard, G. and Ohishi, Y. 2017. The influence of sulfur on the electrical resistivity of hcp iron: Implications for the core conductivity of Mars and Earth. *Geophysical Research Letters*. 44(16): 8254-8259. DOI: 10.1002/2017GL074021

Urakawa, S., Someya, K., Terasaki, H., Katsura, T., Yokoshi, S., Funakoshi, K., Utsuma, W., Katayama, Y., Sueda, Y. and Irifune, T. 2004. Phase relationships and equations of state for FeS at high pressures and temperatures and implications for the internal structure of Mars. *Physics of the Earth and Planetary Interiors*. 143: 469-479. DOI: 10.1016/j.pepi.2003.12.015

Vočadlo, L. 2007. Mineralogy of the Earth – The Earth's core: Iron and iron alloys. *In* *Treatise on Geophysics, Vol. 2. Edited by* G. David Price and Gerald Schubert. Elsevier Ltd., Waltham, Mass. pp. 91-120.

Wagle, F., Steinle-Neumann, G. and de Koker, N. 2018. Saturation and negative temperature coefficient of electrical resistivity in liquid iron-sulfur alloys at high densities from first-principles calculations. *Physical Review B*. 97(9): 094307. DOI: 10.1103/PhysRevB.97.094307

- Wagle, F., Steinle-Neumann, G. and de Koker, N. 2019. Resistivity saturation in liquid iron-light-element alloys at conditions of planetary cores from first principles computations. *Comptes Rendus Geoscience*. 351(2-3): 154-162. DOI: 10.1016/j.crte.2018.05.002
- Wakamatsu, T., Ohta, K., Yagi, T., Hirose, K. and Ohishi, Y. 2018. Measurements of sound velocity in iron-nickel alloys by femtosecond laser pulses in a diamond anvil cell. *Physics and Chemistry of Minerals*. 45(6): 589-595. DOI: 10.1007/s00269-018-0944-3
- Wang, H. and Salveson, I. 2005. A review on the mineral chemistry of the non-stoichiometric iron sulphide, Fe_{1-x}S ($0 \leq x \leq 0.125$): polymorphs, phase relations and transitions, electronic and magnetic structures. *Phase Transitions*. 78(7-8): 547-567. DOI: 10.1080/01411590500185542
- Wang, Z. and Becker, H. 2017. Chalcophile elements in Martian meteorites indicate low sulfur content in the Martian interior and a volatile element-depleted late veneer. *Earth and Planetary Science Letters*. 463: 56-68. DOI: 10.1016/j.epsl.2017.01.023
- Williams, Q. 2009. Bottom-up versus top-down solidification of the cores of small solar system bodies: Constraints on paradoxical cores. *Earth and Planetary Science Letters*. 284(3-4): 564-569. DOI: 10.1016/j.epsl.2009.05.019
- Wood, B., Walter, M. and Wade, J. 2006. Accretion of the Earth and segregation of its core. *Nature*, 441(7095): 825-833. DOI: 10.1038/nature04763
- Yoshizaki, T. and McDonough, W.F. 2020. The composition of Mars. *Geochimica et Cosmochimica Acta*. 273: 137-162. DOI: 10.1016/j.gca.2020.01.011
- Zhan, X. and Schubert, G. 2012. Powering Ganymede's dynamo. *Journal of Geophysical Research: Planets*. 117: E08011. DOI: 10.1029/2012JE004052
- Zhang, Y-G. and Guo, G-J. 2000. Molecular dynamics calculation of the bulk viscosity of liquid iron-nickel alloy and the mechanisms for the bulk attenuation of seismic waves in the Earth's outer core. *Physics of the Earth and Planetary Interiors*. 122(3-4): 289-298. DOI: 10.1016/S0031-9201(00)00198-9

Chapter 5

5 Thermal Convection in the Core of Ganymede Inferred from Liquid Eutectic Fe-FeS Electrical Resistivity at High Pressures

The most exciting phrase to hear in science, the one that heralds new discoveries, is not 'Eureka!', but 'That's funny... '.

- Isaac Asimov

A version of this chapter is currently under peer review:

Littleton, J.A.H., Secco, R.A. and Yong, W. 2021. Thermal Convection in the Core of Ganymede Inferred from Liquid Eutectic Fe-FeS Electrical Resistivity at High Pressures. *Crystals*. 11(8): 875. DOI: 10.3390/cryst11060705

5.1 Introduction

The dipolar magnetic field of Ganymede may be produced by internal convection of a liquid iron (Fe) outer core, similar to Earth's geodynamo (Connerney, 2007). Convective motions in liquid cores may be derived from two broad sources: i) thermal and ii) compositional (Olson, 2016). The former requires heat transfer out of the core exceeding the heat transferred by conduction of the core. The latter is related to the gradual cooling of the core and consequent inner core formation, and density contrasts between precipitated core chemical species and residual liquid (e.g. Fe snow or FeS floatation; Hauck et al., 2006; Rückriemen et al., 2015; 2018). While Ganymede is believed to have a predominantly Fe core, it has been suggested that the core is comprised of more sulphur (S) compared to other terrestrial Fe cores (Schubert et al., 1996; Sohl et al., 2001; Scott et al., 2002; Hauck et al., 2006; Bland et al., 2008; Kimura et al., 2009). A significant effect due to the presence of S as a core element is freezing-point depression. For instance, the eutectic temperature (T) in the Fe-FeS system at 1 atm is ~1260 K, approximately 600 K lower than the melting T of Fe (Kubaschewski, 1982). Impurities and more abundant elemental constituents may also affect transport properties such as electrical resistivity (ρ) and thermal conductivity (κ) (Gomi and Yoshino, 2018), which are two critical

parameters in magnetic field generation via planetary body dynamos. Experimental investigations of ρ and κ of Fe (e.g. Konôpková et al., 2016; Ohta et al., 2016; Silber et al., 2018; Pommier, 2018; Yong et al., 2019; Hsieh et al., 2020; Ezenwa and Yoshino, 2021) and FeS (Pommier, 2018; Manthilake et al., 2019; Littleton et al., 2021) at core conditions have shown varying agreement and consistency. However, typical estimates of the S content in the core of Ganymede, based on internal structure and magnetic field generation models, are adjacent to the Fe-FeS eutectic (Kuskov and Kronrod, 2001; Hauck et al., 2006; Bland et al., 2008; Kimura et al., 2009; Rückriemen et al., 2015; 2018). If core S composition is eutectic or eutectic-adjacent (i.e. within a few weight percent), this may allow the core of Ganymede to be molten and permit thermally driven convection at relatively low core T (<1400 K) that can power a dynamo-produced magnetic field. In this work, we measured ρ of eutectic-adjacent Fe-FeS in both solid and liquid states at pressures (P) up to 5 GPa. The measured results were used to delineate the P-dependent eutectic T and to calculate κ and adiabatic heat flow (Q_a) to determine if thermal convection is permissible in a molten, eutectic-adjacent S composition core of Ganymede constrained to a low core T.

5.2 Materials and Methods

Fe and FeS powders were purchased from ESPI Metals (99.95% purity) and Alfa Aesar (99.98% purity), respectively, and mixed together to attain an S content close to the eutectic composition (Table 5.1) (Buono and Walker, 2015). All experiments were conducted in a 1000-ton cubic anvil press, as described by Secco (1995). A three-sectioned cubic P cell design and four-wire electrical resistance technique using Type S (platinum (Pt) and rhodium (Rh) alloy) thermocouples for all experiments were the same as those used and described by Littleton et al. (2021). Experimental specifications remain largely the same, with two minor alterations: i) the highest T reached was ~1430 K since the liquidus T's are considerably lower for the Fe-FeS system investigated than for FeS; and ii) P- and T-dependent contributions to the measured voltage from tungsten (W) disks placed between the thermocouple junctions and powder mixture sample were accounted for (Littleton et al., 2019) since these contributions were proportionally larger and non-negligible compared to measurements of FeS under similar conditions.

Table 5.1: Values of targeted eutectic Fe-FeS sample compositions and post-experiment analysis results of sample compositions for each pressure in this study. Post-experiment sample compositions are noted to be either Fe-rich or FeS-rich relative to the target pressure-dependent eutectic composition.

Pressure (GPa)	Target Eutectic Composition (wt.% S)	Sample Composition (Post-Experiment) (wt. % S)	Relative Location Adjacent to Eutectic
2	28.0	29.56 ± 0.05	FeS-rich
3	26.5	26.17 ± 0.05	Fe-rich
4	25.1	25.68 ± 0.07	FeS-rich
5	23.8	23.76 ± 0.06	Fe-rich

5.3 Results and Discussion

Figures 5.1a and 5.1b show measured values of ρ and calculated values of κ of Fe-FeS, respectively, up to 5 GPa and ~ 1430 K from this study. Also shown are ρ and κ values of FeS (Littleton et al., 2021), Fe-FeS (20 wt.% S; Pommier, 2018) and Fe (Silber et al., 2018) from previous studies for comparison. Fe-FeS was observed to have intermediate values of ρ compared to the end-members. This result was expected since the addition of electrically conductive Fe to FeS should decrease ρ , or equivalently the addition of semi-conducting FeS to Fe should increase ρ . The Wiedemann-Franz Law (WFL), $\kappa = L \cdot T / \rho$, using a Lorenz number (L) equal to the theoretical Sommerfeld value ($2.445 \cdot 10^{-8} \text{ W} \cdot \Omega \cdot \text{K}^{-2}$) was used to calculate the electronic component of κ . Similarly, as expected, the results showed that Fe-FeS is more thermally conductive than FeS but less so than Fe.

The results of this study showed the T-coefficient of ρ , $(\partial\rho/\partial T)_P$, from room T up to a few hundred degrees increased as a function of increasing P. The T-coefficient was most negative at 2 GPa, which gradually became shallower with each P increment until 5 GPa at which a shallow positive T-coefficient was observed. The negative T-coefficient for 2-

4 GPa is consistent with the trends observed for FeS IV, the hexagonal phase of FeS, at similar conditions (Littleton et al., 2021); however, the positive T-coefficient at 5 GPa is a behaviour more comparable to a metallic electrical conductor (e.g. Pommier, 2018; 2020; Silber et al., 2018; 2019; Yong et al., 2019; Berrada et al., 2020). One interpretation is that Fe-FeS behaviour changes to become more conductor-like with increasing P at low T. Alternatively, as discussed later, this observation may be the result of the sample containing the largest proportion of Fe to account for the P-dependency of the eutectic composition (Buono and Walker, 2015). Below the eutectic T at our experimental P, the binary system exhibits a two-phase solid-state regime (Fe + FeS) (Kubaschewski, 1982; Fei et al., 1997). We doubt this observation is related to a solid-state phase transition since the reported P conditions at which other solid-state phases (e.g. Fe₃S, Fe₃S₂) have been observed well exceed ours (>10 GPa) (Fei et al., 1997; 2000; Li et al., 2001; Stewart et al., 2007; Morard et al., 2008; Kamada et al., 2010). Two sets of low T measurements of Fe-20wt.%S at 4.5 GPa reported by Pommier (2018) are more similar to our observations at 5 GPa. Those results show, however, conflicting solid state trends as one exhibits a positive T-coefficient while the other is negative. With continued heating and increasing T, the T-coefficient of ρ at all P is positive and approaches a nearly linear trend at T leading up to the transition from solid to liquid states. These T-dependencies are also consistent with the trends observed for FeS V (Pommier, 2018; Littleton et al., 2021), the Ni-As-type phase of FeS, and Fe (Ohta et al., 2016; Silber et al., 2018; Pommier, 2018; Yong et al., 2019; Ezenwa and Yoshino, 2021).

The T-dependent trends leading up to the eutectic T observed in this study are in good agreement with those measured by Pommier (2018) who also showed, in full context of that study, that ρ and κ of Fe-FeS had intermediate values of the end-members. With the expectation that 20 wt.% S is more electrically conductive than our higher S contents, as discussed later, the measured values of ρ and κ are also in good agreement within reported error ranges up to the eutectic T. At T above the eutectic, the measured values differ considerably, with high T measurements at 4.5 GPa approaching values as large as 3000 $\mu\Omega\cdot\text{cm}$ while values of ρ in this study remain nearly a magnitude less.

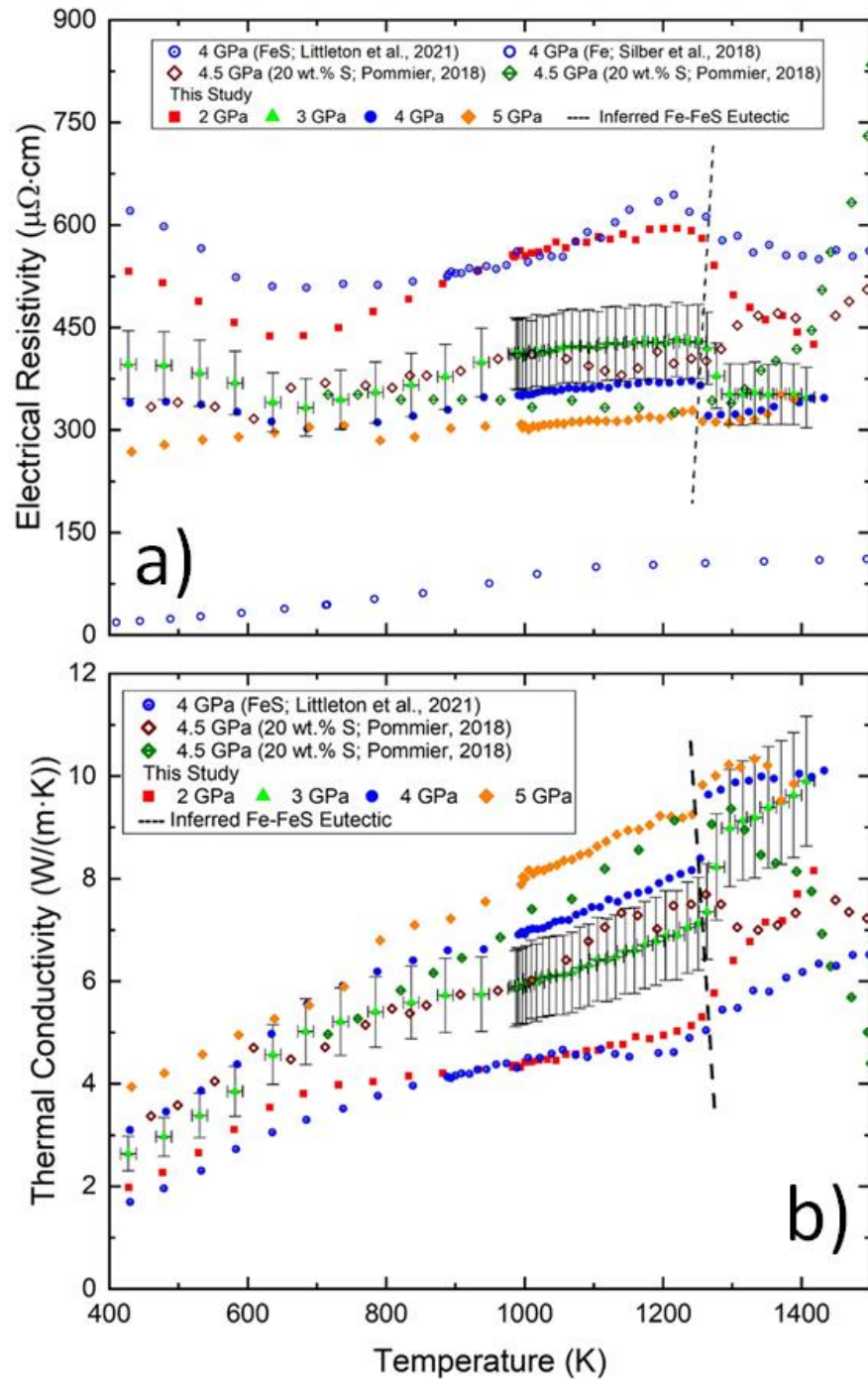


Figure 5.1: (a) Measured electrical resistivity of Fe-FeS at pressures of 2-5 GPa as a function of temperature. Sulphur contents (wt. %) of the samples at each pressure are: 29.56 ± 0.05 (2 GPa); 26.17 ± 0.05 (3 GPa); 25.68 ± 0.07 (4 GPa); 23.76 ± 0.06 (5

GPa). Results of this study are compared to three previous studies and include end-member compositions. The dashed line indicates the transition from solid to molten states and was used to delineate eutectic temperatures; (b) Electronic components of thermal conductivity as a function of temperature of Fe-FeS calculated from the electrical resistivity measurements using the Wiedemann-Franz law and the Sommerfeld value of the Lorenz number. Results of this study are compared to two previous studies. Data of the pure Fe end-member are not shown for scaling purposes ($>12 \text{ W}\cdot\text{m}^{-1}\cdot\text{K}^{-1}$). The dashed line indicates the transition from solid to partially molten states.

The corresponding values of κ calculated via the WFL are expectedly low by comparison to this work. Similar observations and comparisons to Pommier (2018) were made in the FeS investigations by Littleton et al. (2021) in which they suggested that a possible explanation for the rapidly increasing values of ρ was apparent incomplete liquid confinement and reduced thermocouple/electrode chemical integrity. For the 4.5 GPa experiment by Pommier (2018) that utilized molybdenum (Mo) electrodes and Type-C (tungsten (W)-rhenium (Re) alloys) thermocouples, a post-experiment cross-section SEM image of the same sample clearly showed and annotated liquid migration and complete dissolution of the electrodes. We echo the same interpretation as Littleton et al. (2021) for these investigations on Fe-FeS.

A representative post-experiment cross-section is shown in Figures 5.2a and 5.2b. Figure 5.2a shows an image of the cross-section of the 4 GPa pressure cell centered on the sample and Figure 5.2b shows a back-scattered electron image of the same sample. Tabulated electron microprobe results of 15 locations correspond to labeled sites on the Figure 5.2b image. The bulk of the sample retained an Fe-S composition and the bulk of the W disks and arms of the Type-S TC wires retained high chemical purity. After normalizing the Fe and S content values, the microprobe analyses were used to determine an average S-content (wt.% S) of the samples: 29.56 ± 0.05 (2 GPa); 26.17 ± 0.05 (3 GPa); 25.68 ± 0.07 (4 GPa); 23.76 ± 0.06 (5 GPa). For comparison, estimates of the P-dependent eutectic composition of the Fe-FeS system, using the equation reported by

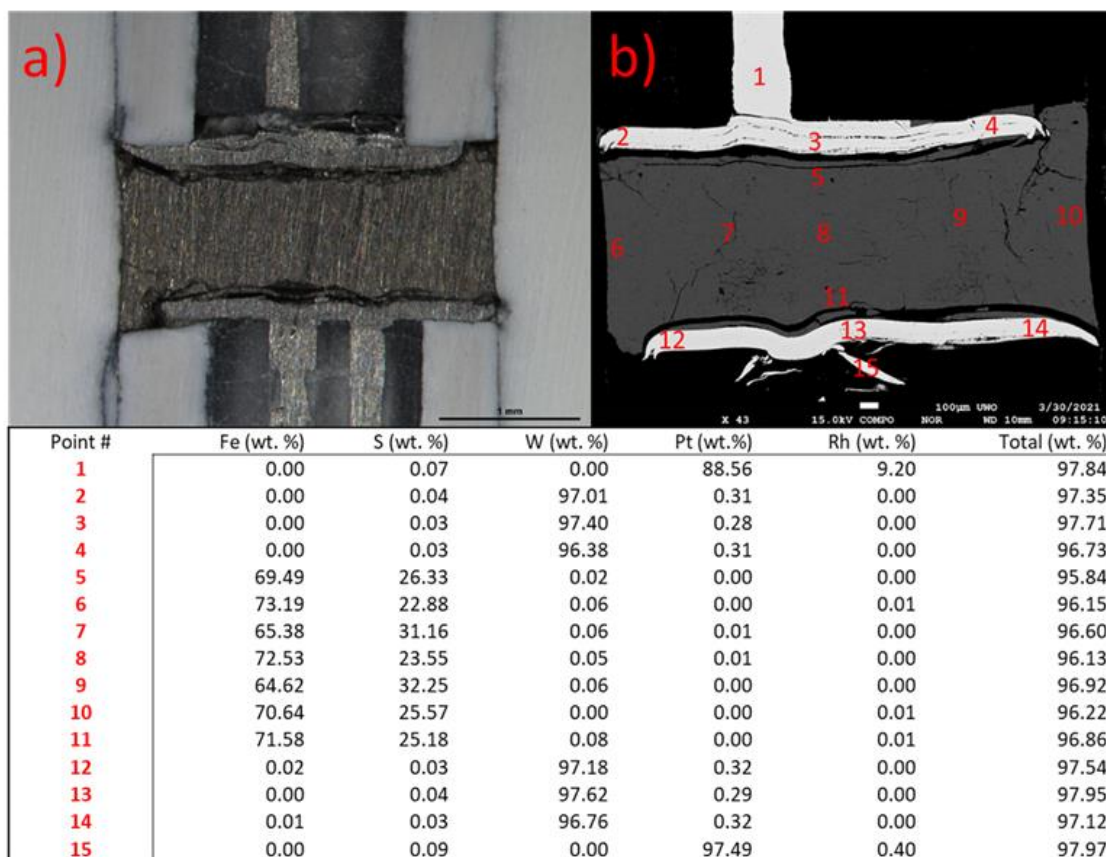


Figure 5.2: (a) Cross-sectional view of the post-experiment 4 GPa pressure cell. Apparent surface lineations of the sample, TC wires, and surrounding BN are due to sanding and lighting. (b) Backscattered electron image of the sample from (a) at a different depth due to additional grinding and polishing required for electron microprobe analysis. Results of the microprobe are tabulated.

Buono and Walker (2015), are (wt. % S): 28.0 (2 GPa); 26.5 (3 GPa); 25.1 (4 GPa); 23.8 (5 GPa) suggesting our sample compositions are eutectic or eutectic-adjacent.

In this study, the abrupt decrease of ρ following the near linear trends is indicative of T exceeding the eutectic T and a state change of the sample from solid to partially liquid. The decrease of ρ at the solidus is consistent with other Fe alloys (e.g. Pommier et al., 2019; Berrada et al., 2020) and FeS (Littleton et al., 2021). Compared to FeS, the decrease is significantly sharper. Although fast heating rate and high measurement frequency were also used here, the difference of the sharpness of this transition is due to a

sample composition in the proximity of the eutectic. An exception, however, are the 2 GPa results that show a broader and gradual decrease similar to FeS. This could be attributed to the composition of the sample being the most S-rich and furthest from the eutectic, resulting in a larger partial melting region. In other words, the more gradual decrease of ρ reflects the gradual production of liquid with increasing T past the eutectic. While previous works have investigated a broader range of S contents (Pommier, 2018; Manthilake et al., 2019), our results are the first well constrained experimental data on near eutectic compositions in the Fe-FeS system.

A line was drawn on Figure 5.1a to estimate the eutectic T at each P where the resistivity trend began to decrease. Immediately left of and right of the line represent the last solid and initial liquid state measurement of the sample, respectively. For the 5 GPa experiment, the results do not show an observable partial melting region. This may indicate that the S content is either very close to or at the eutectic composition. Thus, the measurement immediately to the right of the line represents the initial measurement of a completely liquid state sample. Figure 5.3 compares the eutectic T estimates of this study to prior works at high P. Our results are in good agreement with several prior studies at similar P conditions and indicate that the eutectic T up to 5 GPa does not deviate far from the eutectic at 1 atm. Moreover, our results indicated a negative P-dependency of the eutectic T, a trend also reported by Fei et al. (1997) and Morard et al. (2007) at higher P. However, we note that our P-dependent trend is shallower by comparison. The difference of the trends could be related to the methodology used for determining the eutectic T. Fei et al. (1997) determined eutectic melting on the basis of quenched textures and chemical mapping, while Morard et al. (2007) used *in-situ* x-ray diffraction. Moreover, Buono and Walker (2015) asserted that the presence of hydrogen, from the breakdown of trapped water within the sample material and/or sample enclosure, may be responsible for the significant eutectic T depression in the Fe-FeS system observed by Fei et al. (1997) and Morard et al. (2007).

Estimates of P within the core of Ganymede's range from ~5 GPa at the core-mantle boundary (CMB) to ~11 GPa at its center and T at the CMB span ~1250-2100 K (Sohl et al., 2002; Hauck et al., 2006; Bland et al., 2008; Kimura et al., 2009; Rückriemen et al.,

2018). We adopted the same procedure to calculate adiabatic heat flow (Q_a) at the top of Ganymede's core as Littleton et al. (2021), although for the current study two linear fits to interpolate and extrapolate values of ρ at 5 GPa between 1250-1450 K were used, as shown in the appendices (Appendix B). A positive linear fit (with $(\partial\rho/\partial T)_P > 0 \mu\Omega\cdot\text{cm}/\text{K}$) was used to account for all measurements at T above the estimated eutectic T , while a horizontal linear fit (with $(\partial\rho/\partial T)_P = 0 \mu\Omega\cdot\text{cm}/\text{K}$ and with $\rho = 315 \mu\Omega\cdot\text{cm}$) was used to account for all measurements excluding the highest two temperatures. These were excluded because they may indicate the onset of deteriorating thermocouple integrity and W contamination.

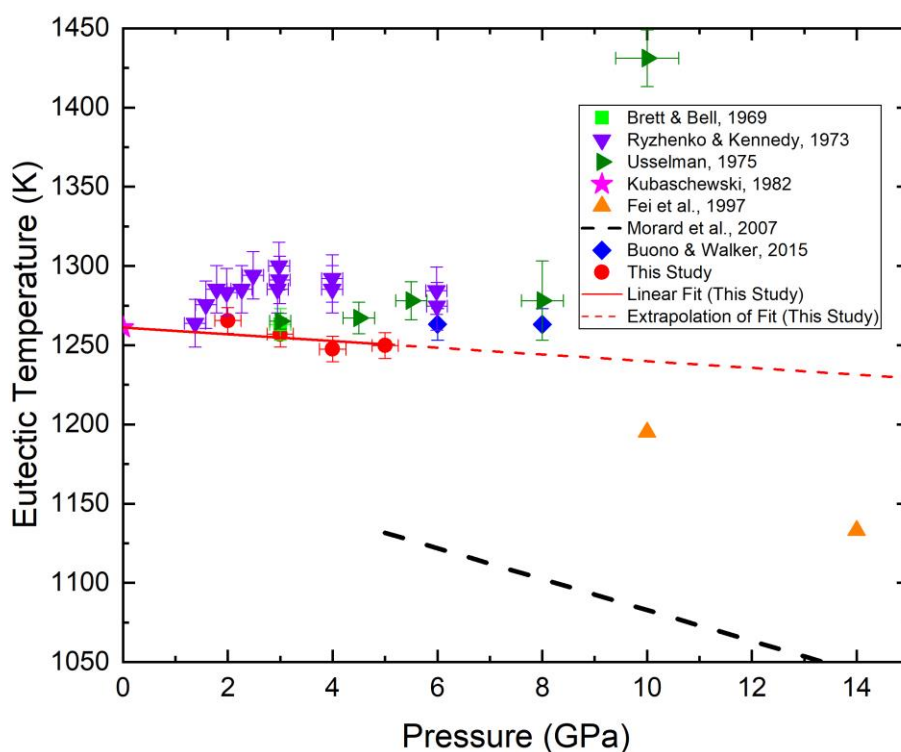


Figure 5.3: Experimentally determined eutectic temperatures of the Fe-FeS system as a function of pressure. The results of this work are compared to several previous works.

Q_a on the core side of the CMB was calculated using Eqn. 5.1 below:

$$Q_a = -4\pi r^2 \kappa \left(\frac{\partial T}{\partial r} \right)_a \quad (5.1)$$

where $(\partial T/\partial r)_a$ is the adiabatic thermal gradient adopted from Breuer et al. (2015). Figure 5.4 shows Q_a at the top of the core with radius varying between 700 and 1200 km and with a CMB T from 1250 to 1450 K and P of 5 GPa alongside estimates of the heat flow through the CMB for comparison. The specified T range was chosen to allow for an entirely molten core. Our estimates of Q_a using a horizontal linear model ranged from ~8 GW for a CMB T of 1250 K and core radius of 700 km up to ~32 GW for a CMB T of 1450 K and core radius of 1200 km. These heat flow estimates are similar in magnitude to those reported by Littleton et al. (2021) for a molten FeS core, which ranged from ~11 GW up to ~37 GW. However, it is important to note that the estimates of this study are for a significantly cooler molten core allowed by a eutectic-adjacent S composition. For instance, if the horizontal linear fit were extrapolated to a core T between 1600 and 1700 K used by Littleton et al. (2021), the lower-bound and upper-bound Q_a in the core would be ~13 GW and ~44 GW, respectively. The heat flow in the core using the positive linear fit is more constrained than the horizontal linear fit, with estimates of Q_a ranging from ~8 GW up to ~28 GW. This result is due to the competing effects of increasing T and ρ , which are directly proportional and inversely proportion to κ , respectively, via the WFL.

Estimates of the heat flux out of the core and through the CMB of Ganymede range from ~1-6 mW/m² (Hauck et al., 2006; Kimura et al., 2009; Rückriemen et al., 2015; 2018). Both the linear and horizontal models showed that thermal convection of a molten Fe-FeS core at relatively low core T is permissible provided the heat flux on the mantle-side of the CMB exceeds ~ 1.5 mW/m². Littleton et al. (2021) showed that thermal convection can carry up to one-third of the heat load to the CMB for a heat transfer of 3 mW/m² through the CMB in a Ganymede core of liquid FeS. The results of this study for a Ganymede core of near eutectic Fe-FeS show a similar heat load proportion that can be carried by thermal convection for our core model, especially when the difference in core T estimates are taken into account. Thus, our results indicate that thermal convection is permissible for the majority of the 1250-1450 K T-range and may be a source of energy

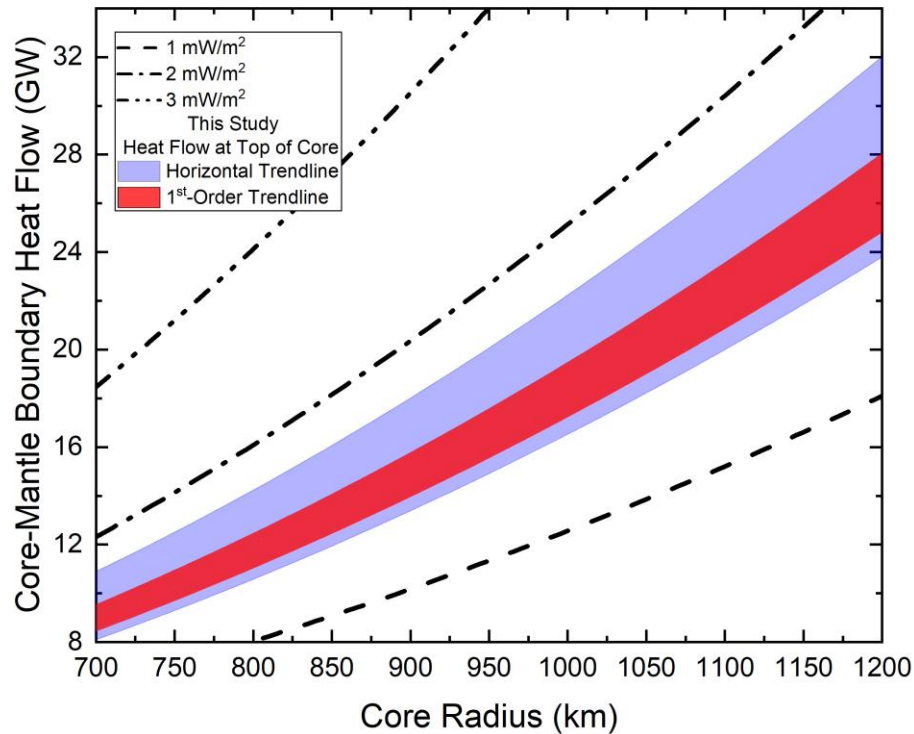


Figure 5.4: Calculated adiabatic heat flow at the core-mantle boundary (CMB) of Ganymede of a fully molten eutectic-adjacent core at 5 GPa. The differently dashed lines each represent different estimates of the heat flow and through the CMB (Hauck et al., 2006; Kimura et al., 2009; Rückriemen et al., 2015; 2018). The shaded regions represent all values of calculated heat flow values on the core-side of the CMB. The lighter blue and darker red shaded regions are calculated values using a horizontal and linear fitting trendline, as shown in the Supporting Information section. The CMB temperature ranges from 1250 K at the bottom to 1450 K at the top of the shaded regions of this study. Propagated uncertainty on the calculations range from ~1 to 1.5% of the reported values.

to power an internal core dynamo to produce the magnetic field of Ganymede. We note that with respect to P and T , these estimates of convective heat load represent a lower-bound. Based on the trends observed in this study and other investigations on the Fe-FeS system (Pommier, 2018), increasing P will result in decreased values of ρ and increased

values of κ and Q_a . Similarly, based on the results of this study, the net effect of increasing T will also result in increased values of κ and Q_a . Acting singly or together, both effects produce a more thermally conductive core and could potentially diminish the effectiveness of, or completely shut down, heat transfer by thermal convection. For instance, extrapolated core heat flow values (~ 13 - 44 GW) of our horizontal linear fit applied to a 1600-1700 K liquid core model (Littleton et al., 2021) suggest that the heat load carried by thermal convection to the CMB can be reduced to one-fifth for a heat transfer of 3 mW/m^2 through the CMB. With respect to S content, these estimates provide information for a middle-ground core composition between the lower- (FeS) and upper- (Fe) bounds. Core thermal conductivity is expected to increase as composition becomes more Fe-rich and decrease as composition becomes more FeS-rich in other core composition models.

We note the absence of consensus regarding the P-dependence of the eutectic T in this system. A linear or non-linear increase (e.g., Usselman, 1975; Boehler, 1996) or decrease (e.g., Fei et al., 1997; Morard et al., 2007; and this study) of the eutectic T can significantly change the lowest-bound T that allows for an entirely molten Fe-FeS core of Ganymede and, consequently, constrains the effectiveness of thermally driven convection as a heat transport mechanism. A higher eutectic T than reported here would result in a core that is more thermally conductive since the lower-bound of Q_a increases and thus decreases reliance on thermally driven convection to power an internal dynamo. Conversely, a lower eutectic T would result in a core that is less thermally conductive since the lower-bound of Q_a decreases and thus increases reliance on thermally driven convection. A CMB pressure of 5 GPa is the lowest expected value. If pressure increases at the CMB, the eutectic composition shifts towards the Fe-end of the binary system and ρ is expected to decrease while κ and Q_a are expected to increase. The uncertain behavior of the eutectic T implies the lower-bound T for either Fe or FeS crystallization regimes is uncertain. Beyond this, it is difficult to precisely describe the extent of the effect of the uncertain eutectic T on both crystallization regimes (bottom-up or top-down) and chemical- or buoyancy-driven convection. This is due to the non-linearity of the liquidus boundaries with increasing P , which marks the onset of crystallization. An increased or

decreased eutectic T may widen or shrink the T range between the liquidus and solidus but may have little to no significant effect on the liquidus T for some compositions.

5.4 Conclusion

The presence of S as an element in the Fe-rich core of Ganymede can allow for an entirely molten core at relatively low core T due to freezing-point depression, while also affecting core transport properties influencing magnetic field generation via an internal dynamo. This study provided measurements of the ρ of Fe-FeS with eutectic-adjacent S-contents in solid and liquid states at P from 2-5 GPa, where the transition from solid to liquid states was inferred from measurements of ρ . The phase transition was used for delineation of the eutectic T of the Fe-FeS system, which showed a small negative P-dependency. Our results are the first well constrained experimental data on near eutectic compositions in this binary system. The electronic component of κ was calculated via the WFL using the measured values of ρ , and subsequently used to estimate Q_a on the core-side of Ganymede's CMB. The results showed that both ρ and κ had intermediate values between the end-members of the system, and that thermal convection may be permissible in the core to transport heat and act as a dynamo energy source.

5.5 References

- Berrada, M., Secco, R.A., Yong, W. and Littleton, J.A.H. 2020. Electrical resistivity measurements of Fe-Si with implications for the early lunar dynamo. *Journal of Geophysical Research – Planets*. 125(7): e2020JE006380. DOI: 10.1029/2020JE006380
- Bland, M.T., Showman, A.P. and Tobie, B. 2008. The production of Ganymede's magnetic field. *Icarus*. 198(2): 384-399. DOI: 10.1016/j.icarus.2008.07.011
- Boehler, R. 1996. Fe-FeS eutectic temperatures to 620 kbar. *Physics of the Earth and Planetary Interiors*. 96(2): 181-186. DOI: 10.1016/0031-9201(96)03150-0
- Brett, R. and Bell, P.M. 1969. Melting relations in the Fe-rich portion of the system Fe-FeS at 30 kb pressure. *Earth and Planetary Science Letters*. 6(6): 479-482. DOI: 10.1016/0012-281 821X(69)90119-8

Breuer, D., Rückriemen, T. and Spohn, T. 2015. Iron snow, crystal floats, and inner-core growth: modes of core solidification and implications for dynamos in terrestrial planets and moons. *Progress in Earth and Planetary Science*. 2(39): 1-26. DOI: 10.1186/s40645-015-0069-y

Buono, A.S. and Walker, D. 2015. H, not O or pressures, causes eutectic T depression in the Fe-FeS system to 8 GPa. *Meteoritics & Planetary Science*. 50(4): 547-554. DOI: 10.1111/maps.12372

Connerney, J.E.P. 2007. Planetary Magnetism. In *Treatise on Geophysics*, Vol. 10. Edited by Tilman Spohn and Gerald Schubert. Elsevier Ltd., Waltham, Mass. pp. 243-280.

Ezenwa, I.C. and Secco, R.A. 2017. Invariant electrical resistivity of Co along the melting boundary. *Earth and Planetary Science Letters*. 474: 120-127. DOI: 10.1016/j.epsl.2017.06.032

Ezenwa, I.C. and Yoshino, T. 2021. Martian core heat flux: Electrical resistivity and thermal conductivity of liquid Fe at martian core P-T conditions. *Icarus*. 360: 114367. DOI: 10.1016/j.icarus.2021.114367

Fei, Y., Bertka, C.M. and Finger, L.W. 1997. High-Pressure Iron-Sulfur Compound, Fe₃S, and Melting Relations in the Fe-FeS System. *Science*. 275(5306): 1621-1623.

Fei, Y., Li, J., Bertka, C.M. and Prewitt, C.T. 2000. Structure type and bulk modulus of Fe₃S, a new iron-sulfur compound. *American Mineralogist*. 85(11-12): 1830-1833. DOI: 10.2138/am-2000-11-1229

Gomi, H. and Yoshino, T. 2018. Impurity Resistivity of fcc and hcp Fe-Based Alloys: Thermal Stratification at the Top of the Core of Super-Earths. *Frontiers in Earth Science*. 6: 217. DOI: 10.3389/feart.2018.00217

Hauck II, S.A., Aurnou, J.M. and Dombard, A.J. 2006. Sulfur's impact on core evolution and magnetic field generation on Ganymede. *Journal of Geophysical Research: Planets*. 111: E09008. DOI: 10.1029/2005JE002557

Hsieh, W-P., Goncharov, A.F., Labrosse, S., Holtgrewe, N., Lobanov, S.S., Chuvashova, I., Deschamps, F. and Lin, J-F. 2020. Low thermal conductivity of iron-silicon alloys at Earth's core conditions with implications for the geodynamo. *Nature Communications*. 11: 3332. DOI: 10.1038/s41467-020-17106-7

Kamada, S., Terasaki, H., Ohtani, E., Sakai, T., Kikegawa, T., Ohishi, Y., Hirao, N., Sata, N. and Kondo, T. 2010. Phase relationships of the Fe-FeS system in conditions up to the Earth's outer core. *Earth and Planetary Science Letters*. 293(1-2): 94-100. DOI: 10.1016/j.epsl.2010.03.011

Kimura, J., Nakagawa, T. and Kurita, K. 2009. Size and compositional constraints of Ganymede's metallic core for driving an active dynamo. *Icarus*. 202(1): 216-224. DOI: 10.1016/j.icarus.2009.02.026

Konôpková, Z., McWilliams, R.S., Gómez-Pérez, N. and Goncharov, A.F. 2016. Direct measurement of thermal conductivity of solid iron at planetary core conditions. *Nature*. 534(7605): 99-101. DOI: 10.1038/nature18009

Kubaschewski, I. 1982. Iron-Sulphur. In *IRON – Binary Phase Diagrams*. Springer-Verlag Berlin Heidelberg GmbH, Düsseldorf, Germany. pp. 125-128.

Kuskov, O.L. and Kronrod, V.A. 2001. Core Sizes and Internal Structure of Earth's and Jupiter's Satellites. *Icarus*. 151(2): 204-227. DOI: 10.1006/icar.2001.6611

Li, J., Fei, Y., Mao, H.K., Hirose, K. and Shieh, S.R. 2001. Sulfur in the Earth's inner core. *Earth and Planetary Science Letters*. 193(3-4): 509-514. DOI: 10.1016/S0012-821X(01)00521-0

Littleton, J.A.H., Secco, R.A. and Yong, W. 2021. Electrical Resistivity of FeS at High Pressures and Temperatures: Implications of Thermal Transport in the Core of Ganymede. *Journal of Geophysical Research: Planets*. 126(5): e2020JE006793. DOI: 10.1029/2020JE006793

Littleton, J.A.H., Secco, R.A., Yong, W. and Berrada, M. 2019. Electrical resistivity and thermal conductivity of W and Re up to 5 GPa and 2300 K. *Journal of Applied Physics*. 125(13): 135901. DOI: 10.1063/1.5066103

Manthilake, G., Chantel, J., Monteux, J., Andrault, D., Bouhifd, M.A., Casanova, N.B., Boulard, E., Guignot, N., King, A. and Itie, J.P. 2019. Thermal Conductivity of FeS and its Implications for Mercury's Long-Sustaining Magnetic Field. *Journal of Geophysical Research: Planets*. 124(9): 2359-2368. DOI: 10.1029/2019JE005979

Morard, G., Andrault, D., Guignot, N., Sanloup, C., Mezouar, M., Petitgirard, S. and Fiquet, G. 2008. In situ determination of Fe-Fe₃S phase diagram and liquid structural properties up to 65 GPa. *Earth and Planetary Science Letters*. 272(3-4): 620-626. DOI: 10.1016/j.epsl.2008.05.028

Morard, G., Sanloup, C., Fiquet, G., Mezouar, M., Rey, N., Poloni, R. and Beck, P. 2007. Structure of eutectic Fe-FeS melts to pressures up to 17 GPa: Implications for planetary cores. *Earth and Planetary Science Letters*. 262(1-2): 128-139. DOI: 10.1016/j.epsl.2007.09.009

Ohta, K., Kuwayama, Y., Hirose, K., Shimizu, K. and Ohishi, Y. 2016. Experimental determination of the electrical resistivity of iron at Earth's core conditions. *Nature*. 534: 95-98. DOI: 10.1038/nature17957

Olson, P. 2016. Mantle control of the geodynamo: Consequences of top-down regulation. *Geochemistry, Geophysics, Geosystems*. 17(5): 1935-1956. DOI: 10.1002/2016GC00633417

Pommier, A. 2018. Influence of sulfur on the electrical resistivity of a crystallizing core in small terrestrial bodies. *Earth and Planetary Science Letters*. 496: 37-46. DOI: 10.1016/j.epsl.2018.05.032

Pommier, A., Leinenweber, K. and Tran, T. 2019. Mercury's thermal evolution controlled by an insulating liquid outermost core?. *Earth and Planetary Science Letters*. 517: 125-134. DOI: 10.1016/j.epsl.2019.04.022

- Pommier, A. 2020. Experimental investigations of the effect of nickel on the electrical resistivity of Fe-Ni and Fe-Ni-S alloys under pressure. *American Mineralogist*. 105(7): 1069-1077. DOI: 10.2138/am-2020-7301
- Ryzhenko, B. and Kennedy, G.C. 1973. The effect of pressure on the eutectic in the system Fe-FeS. *American Journal of Science*. 273(9): 803-810. DOI: 10.2475/ajs.273.9.803
- Rückriemen, T., Breuer, D. and Spohn, T. 2015. The Fe snow regime in Ganymede's core: A deep-seated dynamo below a stable snow zone. *Journal of Geophysical Research: Planets*. 120(6): 1095-1118. DOI: 10.1002/2014JE004781
- Rückriemen, T., Breuer, D. and Spohn, T. 2018. Top-down freezing in a Fe-FeS core and Ganymede's present-day magnetic field. *Icarus*. 307: 172-196. DOI: 10.1016/j.icarus.2018.02.021
- Schubert, G., Zhang, K., Kivelson, M.G. and Anderson, J.D. 1996. The magnetic field and internal structure of Ganymede. *Nature*. 384(6609): 544-545. DOI: 10.1038/384544a018
- Scott, H.P., Williams, Q. and Ryerson, F.J. 2002. Experimental constraints on the chemical evolution of large icy satellites. *Earth and Planetary Science Letters*. 203(1): 399-412. DOI: 10.1016/S0012-821X(02)00850-6
- Secco, R.A. 1995. High p,T physical property studies of Earth's interior: Thermoelectric power of solid and liquid Fe up to 6.4 GPa. *Canadian Journal of Physics*. 73: 287-294. DOI: 10.1139/p95-040
- Silber, R.E., Secco, R.A. and Yong, W. 2017. Constant electrical resistivity of Ni along the melting boundary up to 9 GPa. *Journal of Geophysical Research: Solid Earth*. 122(7): 5064-5081. DOI: 10.1002/2017JB014259
- Silber, R.E., Secco, R.A., Yong, W. and Littleton, J.A.H. 2018. Electrical resistivity of liquid Fe to 12 GPa: Implications for heat flow in core of terrestrial bodies. *Scientific Reports*. 8(1): 1-9. DOI: 10.1038/s41598-018-28921-w

Silber, R.E., Secco, R.A., Yong, W. and Littleton, J.A.H. 2019. Heat Flow in Earth's Core From Invariant Electrical Resistivity of Fe-Si on the Melting Boundary to 9 GPa: Do Light Elements Matter?. *Journal of Geophysical Research: Solid Earth*. 124(6): 5521-5543. DOI: 10.1029/2019JB017375

Sohl, F., Spohn, T., Breuer, D. and Nagel, K. 2002. Implications from Galileo Observations on the Interior Structure and Chemistry of the Galilean Satellites. *Icarus*. 157(1): 101-119. DOI: 10.1006/icar.2002.6828

Stewart, A.J., Schmidt, M.W., van Westrenen, W. and Liebske, C. 2007. Mars: A New Core Crystallization Regime. *Science*. 316(5829): 1323-1325. DOI: 10.1126/science.114054919

Usselman, T.M. 1975. Experimental approach to the state of the core: Part I. The liquidus relations of the Fe-rich portion of the Fe-Ni-S system from 30 to 100 kb. *American Journal of Science*. 275(3): 278-290. DOI: 10.2475/ajs.275.3.278

Yong, W., Secco, R.A., Littleton, J.A.H. and Silber, R.E. 2019. The Iron Invariance: Implications for Thermal Convection in Earth's Core. *Geophysical Research Letters*. 46(20): 11065-11070. DOI: 10.1029/2019GL084485

Chapter 6

6 Conclusion

To explain all nature is too difficult a task for any one man or even for any one age. 'Tis much better to do a little with certainty, & leave the rest for others that come after you, than to explain all things by conjecture without making sure of any thing.

- Sir Isaac Newton

The overarching goal of this thesis was to measure the electrical resistivity of solid and liquid Ag, FeS and Fe-FeS (~24-30 wt.% S) in order to better constrain the heat transport properties of cores of small terrestrial bodies, such as the S-bearing Fe-rich metallic core of Ganymede.

6.1 Silver

The results on Ag were used to test Stacey's hypothesis of resistivity invariance along the P-dependent melting boundary of *d*-band filled pure metals. The results were used to compare the effect of the electronic configuration and band structure of metals, specifically the roles played by filled and partially-filled *d*-bands, on resistivity invariance. Partially filled *d*-bands contribute to electron scattering in transition metals and their effects on ρ along the P-dependent melting boundary need to be understood to test either of Stacey's hypotheses, both of which were intended for application to planetary cores. The ρ of Ag in the solid and liquid state decreased as a function of increasing P and increased as a function of increasing T. The P- and T-dependent melting boundary was inferred from the sharp, large increase in ρ , which gave excellent agreement with previous studies. It was shown that liquid Ag resists an electrical current greater than solid Ag. Along the melting boundary, ρ was observed to decrease as a function of increasing P. This result directly contrasts two hypotheses that suggested invariance of the value of ρ along the melting boundary will be observed for a simple metal, such as Ag, and the hypotheses as written can be discarded. The results were discussed in terms of increasing energy separation between the *4d*-band and conducting *5s*-band of Ag in both solid and liquid states, which are not accounted for in both

hypotheses that were derived from a macroscopic thermodynamical model. Moreover, the possibility for core proxy values obtained at the low-end of the high P scale is not supported by our observations. The κ_e of Ag, calculated using the WFL, increased as a function of increasing P and decreased as a function of increasing T. Liquid Ag was observed to be a poorer thermal conductor than solid Ag.

6.2 Iron Sulphides

This study provides detailed measurements of the ρ of FeS and eutectic-adjacent Fe-FeS in solid and molten states at pressures from 2-5 GPa in a cubic anvil press with well-controlled sample geometry. These resistivity results are the first well constrained experimental data on near eutectic compositions in this important terrestrial core binary system. Similar to the delineation of the melting T in Chapter 2, eutectic temperatures for the Fe-FeS system were inferred from the sharp decrease in ρ and were in good agreement with previous works. Using the values of κ_e obtained from the WFL, the calculated values of Q_a of FeS and Fe-FeS both indicated that thermal convection is permissible in models of a molten core of Ganymede, provided a minimum heat flux out of the core, through the CMB, of ~ 1.5 -2 mW/m². Thus, thermally-driven convection could be an on-going process in tandem with chemically- or buoyancy-driven convection (i.e. Fe snowing or FeS floatation) to power an internal dynamo that generates the satellite's dipolar magnetic field.

6.3 Suggested Future Works

While the description of ρ invariance along the melting boundary given by either of Stacey's hypotheses does not appear to withstand scrutiny by experimental methods and observations of this work and others (e.g. McWilliams et al., 2015; Ezenwa and Secco, 2017; Ezenwa et al., 2017; Silber et al., 2017, 2018; Yong et al., 2019; Berrada et al., 2018), the concept of ρ invariance still remains a possibility and requires a more accurate description of the phenomenon of electron scattering under antagonistic effects of high P and T. This statement is justified based on observations of high purity Zn (Ezenwa and Secco, 2017), Pt (McWilliams et al., 2015) and Fe (Silber et al., 2018; Yong et al., 2019). The results of Zn support both hypothesis of ρ invariance along the melting boundary as

described by Stacey and Anderson (2001) and Stacey and Loper (2007). The results of Pt support the earlier hypothesis, but not the latter. Lastly, the results of Fe support neither hypothesis; however, invariance is observed under certain conditions and may provide insight into additional constraints that need to be taken into account in a newer iteration of an invariance hypothesis that must be founded in a description of electronic structure and electron scattering mechanisms. Specifically, Fe was observed to have ρ invariance along the melting boundary only at P where the face-centered cubic phase of Fe was the stable solid phase up to melting. It has not been shown whether this behaviour would persist with the higher pressure hexagonal-close-packed phase as the stable solid phase prior to melting. Much higher P experiments are required. Alternatively, it may not be possible to establish a hypothesis with a universal description and instead may require descriptions on a metal-by-metal basis. Regardless, more high P-T measurements of ρ on both metals previously investigated and metals not yet investigated should be performed to address this outstanding issue. There is much to be done in the area of ρ and κ property determine for application to thermal modelling of terrestrial-like planetary bodies in our solar system. However, an even greater challenge appearing on the horizon is for similar studies to be carried out at the even greater P,T conditions of terrestrial-type exoplanets where the internal pressures are an order of magnitude larger than in Earth.

Higher P-T experiments measuring ρ of FeS and Fe-FeS directly are needed to fully address the transport properties of Ganymede's core, and are needed to begin addressing cores of larger terrestrial bodies that also contain S, such as Mercury (~2-6 wt.% S) and Mars (~10-20 wt.% S). To achieve this while using a relatively large powder sample volume, an octahedral cell design for use in a multi-anvil press implementing the same or similar four-wire electrical resistance technique (e.g. Yong et al., 2019) needs to be developed. Only a few S-content compositions of the Fe-FeS system have been studied and therefore, there are many opportunities to contribute to a thorough systematic study investigating the effect of increasing (or decreasing) S content on ρ in both the solid and liquid states within the Fe-FeS system at high P-T conditions. A sample preparation methodology should be developed that results in a sample composition exactly at, or closer to, 36.5 wt.% S (FeS). The commercially available FeS powder that was purchased for experiments in Chapter 3 had a slightly less than the ideal composition since it was

not stoichiometrically FeS, resulting in several hundreds of degrees with a solid+liquid sample state. A purer sample, with respect to stoichiometry, would greatly aid in constraining ρ of solid and liquid FeS. Lastly, direct measurements of κ would help constrain the L value in the WFL, as well as determine whether the WFL is valid to use for FeS and Fe-FeS at high P-T conditions.

For a more realistic evaluation of terrestrial S-bearing Fe-rich cores, experimental investigations of ρ and κ at high P-T conditions for other than binary alloying systems are required since there is likely more than one lighter impurity element present. A reasonable next step is to investigate the ternary alloying systems of Fe-S-X, where X is an additional light element candidate. These candidates may include Si, O, C, and H. Moreover, investigations of the Fe-S-H system will help constrain the effect of H on eutectic melting. Minor amounts of H have been suggested to be responsible for the significant freezing/melting-point depression observed at P approaching core conditions of larger terrestrial cores (Buono and Walker, 2015). This will also require simultaneous investigations of H-free Fe-S at the same conditions. The thermal and physical state of S-bearing Fe-rich cores may change significantly if H is found to be responsible for currently reported Fe-FeS eutectic temperatures at high P.

6.4 References

- Berrada, M., Secco, R.A. and Yong, W. 2018. Decreasing electrical resistivity of gold along the melting boundary up to 5 GPa. *High Pressure Research*. 38(4): 367-376. DOI: 10.1080/08957959.2018.1493476
- Buono, A.S. and Walker, D. 2015. H, not O or pressures, causes eutectic T depression in the Fe-FeS system to 8 GPa. *Meteoritics & Planetary Science*. 50(4): 547-554. DOI: 10.1111/maps.12372
- Ezenwa, I.C. and Secco, R.A. 2017. Constant electrical resistivity of Zn along the melting boundary up to 5 GPa. *High Pressure Research*. 37(3): 319-333. DOI: 10.1080/08957959.2017.1340473

Ezenwa, I.C., Secco, R.A., Yong, W., Pozzo, M. and Alfè, D. 2017. Electrical resistivity of solid and liquid Cu up to 5 GPa: Decrease along the melting boundary. *Journal of Physics and Chemistry of Solids*. 110: 386-393. DOI: 10.1016/j.jpcs.2017.06.030

McWilliams, R.S., Konôpková, Z. and Goncharov, A.F. 2015. A flash heating method for measuring thermal conductivity at high pressure and temperature: Application to Pt. *Physics of Earth and Planetary Interiors*. 247: 17-26. DOI: 10.1016/j.pepi.2015.06.002

Silber, R.E., Secco, R.A. and Yong, W. 2017. Constant electrical resistivity of Ni along the melting boundary up to 9 GPa. *Journal of Geophysical Research: Solid Earth*. 122(7): 5064-5081. DOI: 10.1002/2017JB014259

Silber, R.E., Secco, R.A., Yong, W. and Littleton, J.A.H. 2018. Electrical resistivity of liquid Fe to 12 GPa: Implications for heat flow in core of terrestrial bodies. *Scientific Reports*. 8(1): 1-9. DOI: 10.1038/s41598-018-28921-w

Yong, W., Secco, R.A., Littleton, J.A.H. and Silber, R.E. 2019. The Iron Invariance: Implications for Thermal Convection in Earth's Core. *Geophysical Research Letters*. 46(20): 11065-11070. DOI: 10.1029/2019GL084485

Appendices

Appendix A: Supporting Information for Chapter 3

A.1 Pressure Cell Design

The P transmitting medium was a 3.175 cm edge length pyrophyllite cube that was sectioned in to top and bottom components with equivalent cross-sectional thicknesses of 1.016 cm and a middle component with a cross-sectional thickness of 1.143 cm. The top and bottom components contained a graphite sleeve running the thickness of the section with an outer and inner diameter of 0.831 cm and 0.699 cm, respectively. Sized to the inner diameter of the graphite sleeve were a zirconia disk and pyrophyllite plug with thicknesses of 0.102 cm and 0.914 cm, respectively. Similarly, the middle component contained a graphite sleeve running the thickness of the section with identical outer and inner diameters as those in the top and bottom components. The graphite sleeve was tightly enclosed by a cylindrical zirconia annulus with an outer diameter of 1.067 cm. Running the thickness of the section and sized to the inner diameter of the graphite sleeve was a rod of boron nitride with a 0.279 cm hole drilled through the center length-wise. A pair of linear channels orientated perpendicular to each other were milled along the square faces of the middle section with one on each side. Each channel was 0.102 cm deep by 0.112 cm wide and ran the entire edge length of the square face while cutting through the center.

Two boron nitride cylinders with a diameter of 0.279 cm and length of 0.381 cm had a 0.157 cm diameter hole drilled through the center of the circular faces. Two four-hole alumina tubes with a diameter of 0.157 cm were cut to a length of 0.356 cm. A 0.025 cm void space created by length differences between the sheathed alumina tube inside of a boron nitride cylinder was intentional and accounted for wire thickness. Specifically, 0.025 cm diameter platinum (Pt) wires and platinum alloyed with 10 wt.% rhodium (Pt-Rh) wires were each threaded into both alumina tubes prior to emplacement into the boron nitride. At the end corresponding to the anticipated void space, the wires were bent into a hook and inserted straight-end first into the alumina tubes. The wires continued to

be threaded into the tubes until the end of the hooks aligned into an unoccupied hole. One boron nitride cylinder was placed into the boron nitride hole of the middle section and pushed into the section until there was a 0.102 cm gap between the cylinder and the surface of the square face. One alumina tube containing a pair of Pt and Pt-Rh wires was inserted into the cylinder, with the hook-ends deepest in the section. A 0.102 cm diameter, single-hole ceramic tube was placed around each straight-end of the Pt/Pt-Rh wires that protruded out from the square face. The sheathed wires were bent into edge length channels of the same face. Excess sheath material extruding from middle section at either end of the channel was removed so that the ends of the sheath truncated at the ends of the channel. Alumina cement was next applied to fill the 0.102 cm gap and allowed to harden for approximately 30 minutes.

The middle section was filled from the remaining open-hole boron nitride face. A circular tungsten (W) disk with diameter of approximately 0.229 cm and thickness of 0.010 cm was dropped into the boron nitride hole and gently hammered upon. The hammering was necessary for two reasons: i) ensure the malleable Pt/Pt-Rh wires are flush along the boron nitride cylinder surface; and ii) create a level platform and seal for powder emplacement, ensuring powder does not fall into the holes of the alumina tubes. FeS was poured into the boron nitride and gently pressed upon to ensure as tight packing as possible. This process was done incrementally while ensuring minimal amounts of powder sticks to the walls of the boron nitride hole. Once approximately 0.178 cm of powder was packed, a second W disk was placed on top and level with the FeS sample, followed by the insertion of the second boron nitride cylinder into the boron nitride hole. Similarly, the cylinder was pushed into the section until there was a 0.102 cm gap between the cylinder and the surface of the square face. A gentle stream of compressed air was used to blow away any powder that may have been agitated and displaced on top of the second W disk during assembly. The second alumina tube bearing Pt/Pt-Rh wires was inserted into the boron nitride cylinder, with wire sheathing, bending into channels along the square face, and alumina cement procedures the same as for the first tube-wire emplacement were applied.

Figure 2.2a and 2.2b show a fully assembled cubic P cell placed graphite-face down on the bottom axial anvil before and after an experiment. The cube was then rotated such that each lateral face aligned parallel to a lateral anvil. Shown in Fig. 2.2a are the square face aligned 0.508 cm diameter holes through a pair of opposing pyrophyllite corners of each section. Two 3.175 cm long pyrophyllite pin rods, with a diameter to match the size of the holes, were inserted to maintain alignment of the three sections. Also shown in Fig. 2.2a are small, circular copper (Cu) foil pieces (0.010 cm thickness) that have been pierced to allow the protruding Pt/Pt-Rh wires to be threaded through. The ends of the wires are bent and flattened against the Cu foil. The Cu foils served to enhance the spatial contact and maintain electrical continuity between the opposing anvils and each wire arm. The perimeter surface area of the cube was coated in iron (III) oxide to increase friction between the cube and anvils during compression.

Compression of the P cell helps establish and improve three important electrical contacts: i) three co-axial graphite sleeves; ii) each pair of Pt/Pt-Rh wires and W disks; and iii) W disks and the FeS powder sample. The alignment of the three sections maintained by the pyrophyllite pin rods, significantly increased the chance of mechanical contact between all three graphite sleeves during compression. In turn, a controlled high alternating current can be passed through the axial anvils. This allowed graphite to act as a resistor and be used to heat the sample via ohmic dissipation. The zirconia annulus and caps effectively formed a cylindrical thermally insulating envelope around the sample that helped to ensure heat was retained at the center and T remained as homogenous as possible (i.e. to help reduce thermal gradient) (Schloessin and Lenson, 1989). The chemical and thermal stability of boron nitride was expected to prevent reactions with either the sample or Pt/Pt-Rh wires at high T.

A.2 Electron Microprobe Analyses of Additional Experiments

The following figures (Fig. A.1-A.3) show images and elemental analyses of post-experiment samples of the 2, 3, and 5 GPa experiments, respectively.

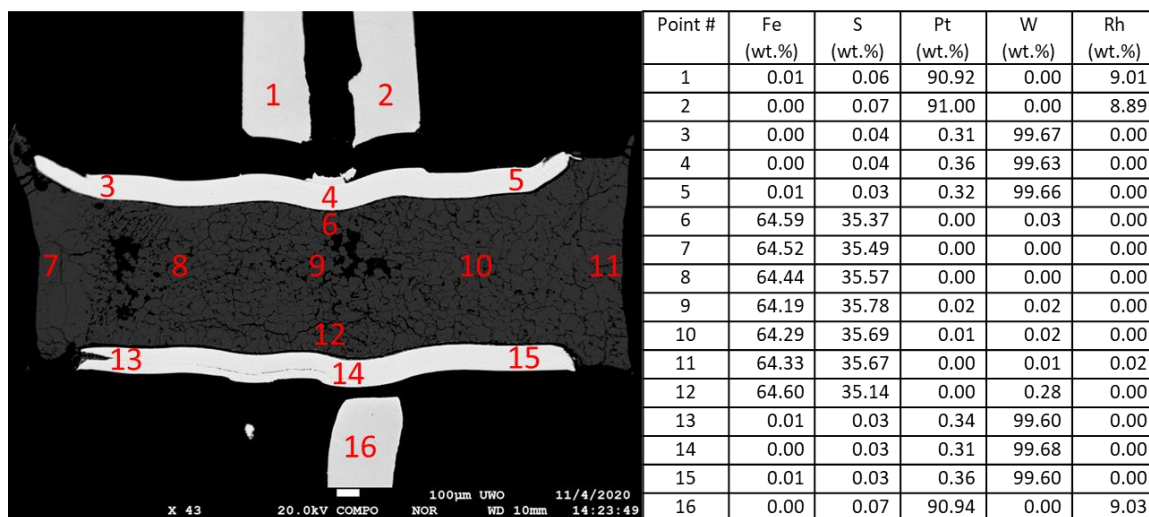


Figure A.1: Back-scattered electron image of the post-experiment 2 GPa pressure cell. Results of the microprobe have been tabulated and normalized. Instances of negative normalized values have been set to 0.00 wt.%.

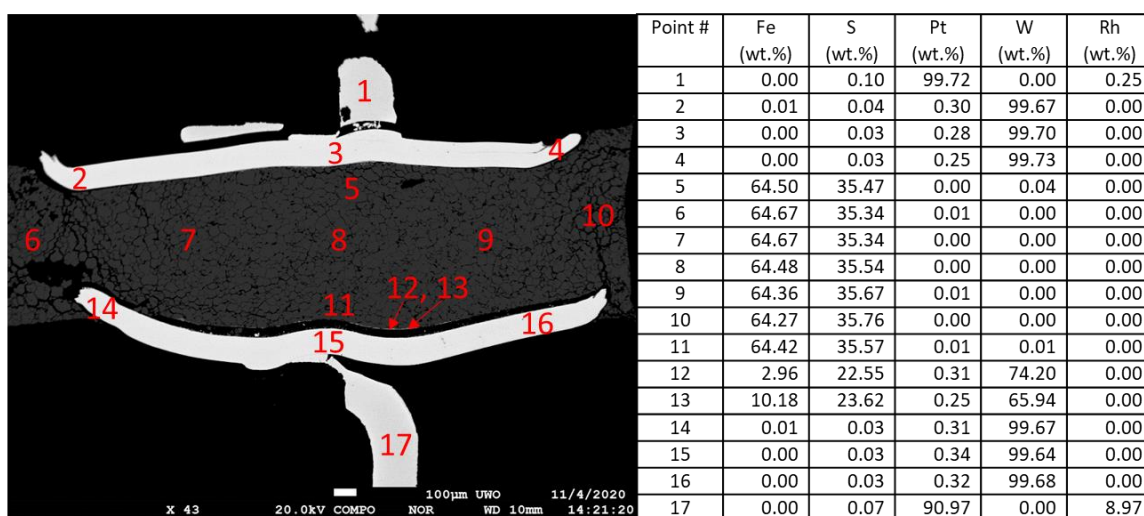


Figure A.2: Back-scattered electron image of the post-experiment 3 GPa pressure cell. Results of the microprobe have been tabulated and normalized. Instances of negative normalized values have been set to 0.00 wt.%.

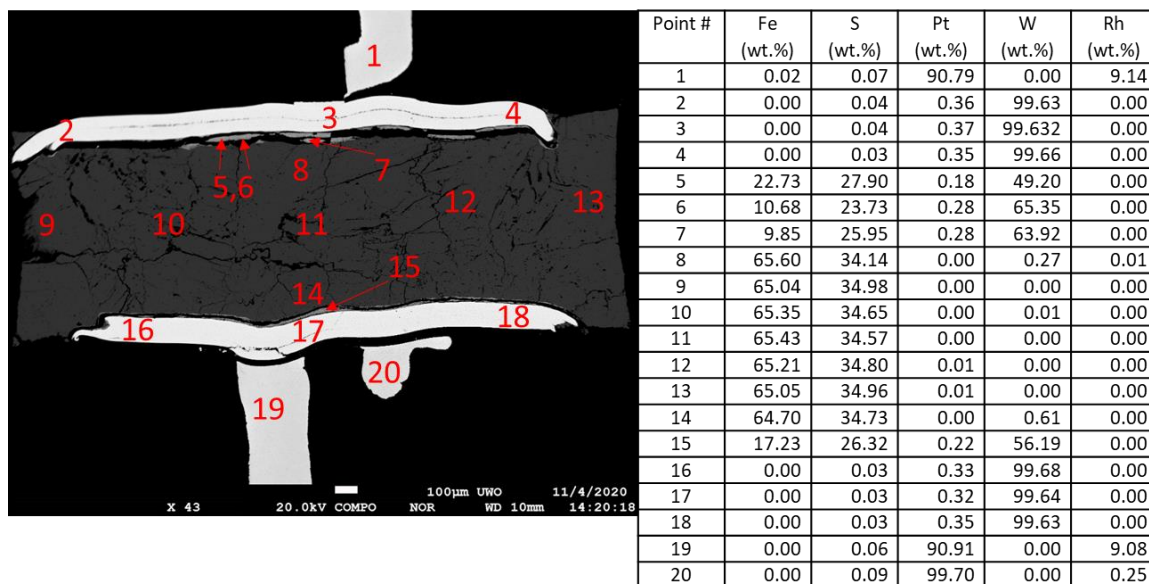


Figure A.3: Back-scattered electron image of the post-experiment 5 GPa pressure cell. Results of the microprobe have been tabulated and normalized. Instances of negative normalized values have been set to 0.00 wt.%.

A.3 Electrical Resistivity Interpolation of 5 GPa Data: 1600-1700 K

The following figure (Fig. A.4) shows the values and function used to interpolate the value of electrical resistivity at temperatures between 1600 K and 1700 K. The interpolated values were used to calculate the adiabatic conductive heat flow at the top of the core of Ganymede.

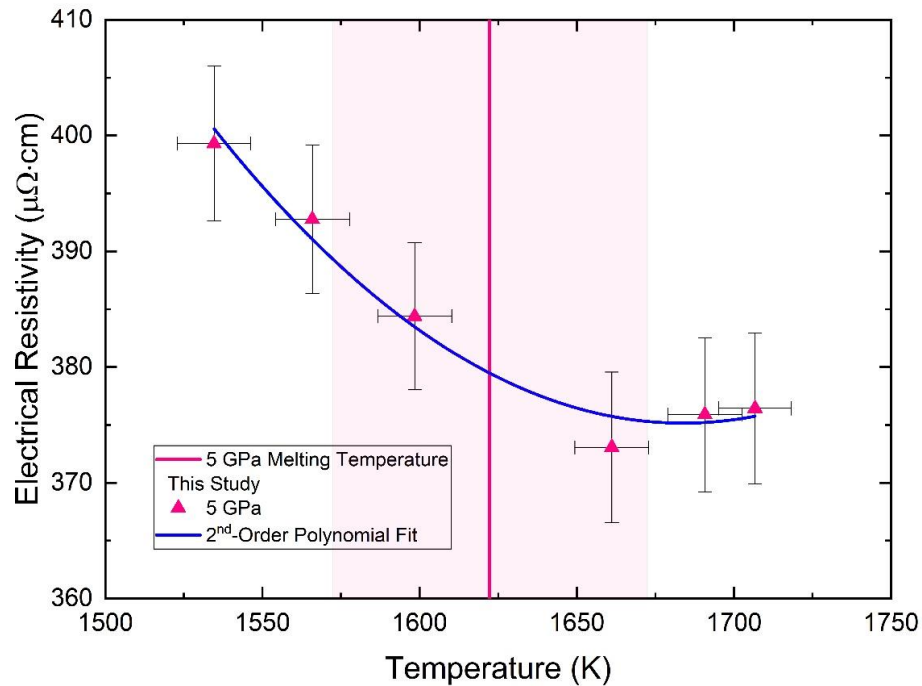


Figure A.4: A second-order polynomial was fitted to six measurements of the 5 GPa experiment. The polynomial fit was used to interpolate the values of electrical resistivity for temperatures from 1600 K and 1700 K. The interpolated values were used to calculate the adiabatic conductive heat flow for the core of Ganymede described in the main text. Estimate of the FeS melting temperature at 5 GPa, shown by the shaded region, was taken from Boehler (1992) with an uncertainty of ± 50 K.

Appendix B: Supporting Information for Chapter 4

B.1 Electrical Resistivity Interpolation of 5 GPa Data: 1250-1450 K

The following figure (Fig. B.1) shows the values and function used to interpolate the value of electrical resistivity at temperatures between 1250 K and 1450 K. The interpolated and extrapolated values were used to calculate the adiabatic conductive heat flow at the top of the core of Ganymede.

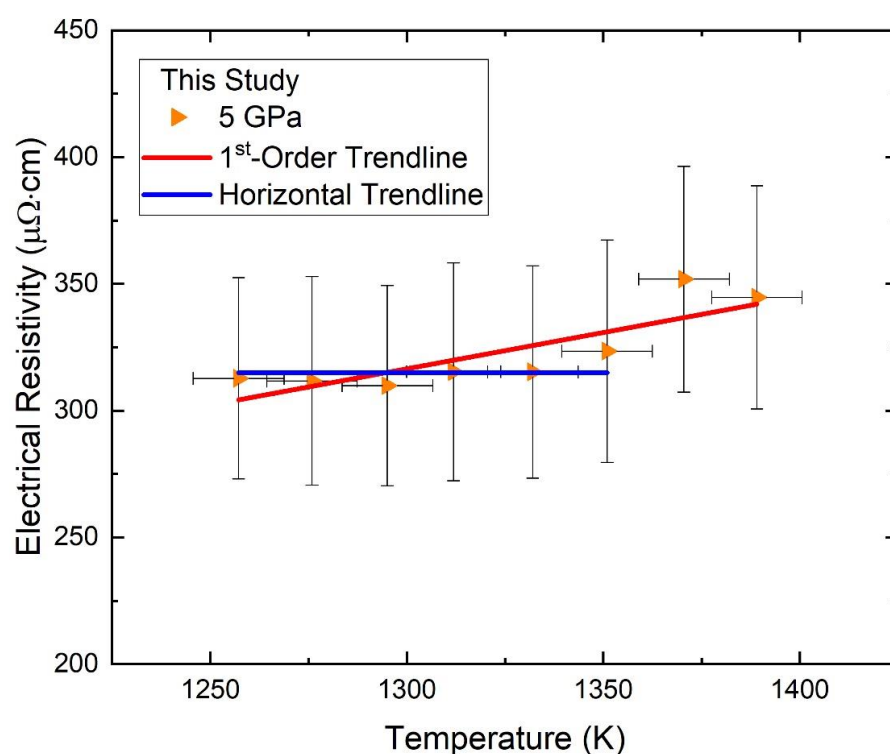


Figure B.1: A first-order polynomial (red) was fitted to eight measurements and a horizontal line ($315 \mu\Omega\cdot\text{cm}$; blue) was fitted to six measurements of the 5 GPa experiment. Both fits were used to interpolate and extrapolate the values of electrical resistivity for temperatures from 1250 K and 1450 K. The values obtained from these fits were used to calculate the adiabatic conductive heat flow for the core of Ganymede described in the main text.

Appendix C: Selected Prior Cell Designs and Unsuccessful Results

C.1 Silver

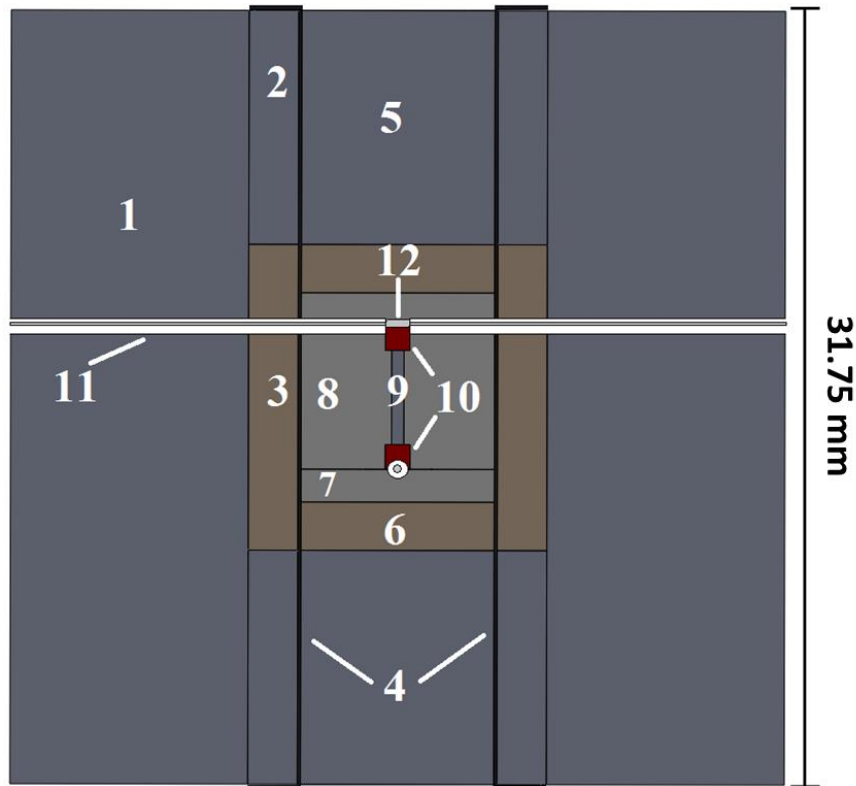


Figure C.1: Cross-section of an assembled cube using the first cell design. The thermocouple is not to scale to emphasize location and shape. 1) Pyrophyllite cube; 2) Pyrophyllite sleeve; 3) Zirconia sleeve; 4) Niobium furnace; 5) Pyrophyllite plug; 6) Zirconia cap; 7) Boron nitride cap; 8) Boron nitride sample container; 9) Silver wire sample; 10) Rhenium plugs; 11) Ceramic tube; 12) Thermocouple.

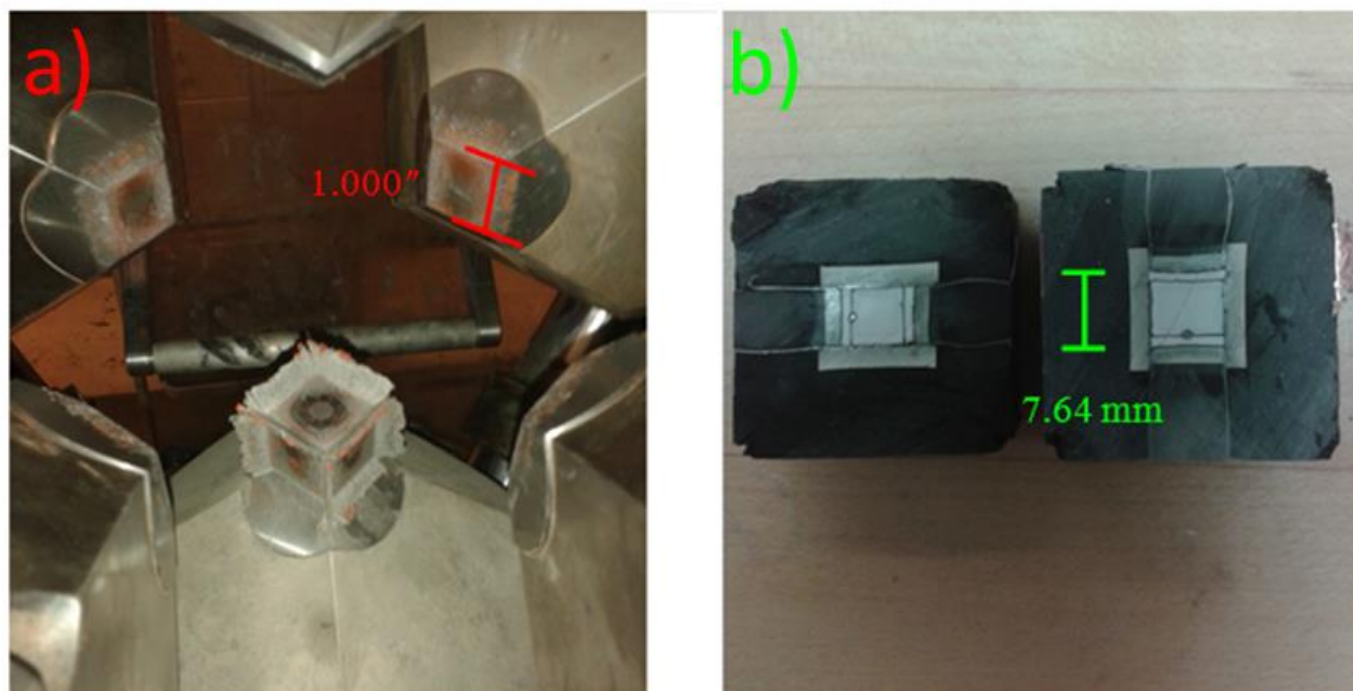


Figure C.2: a) Post-experiment view of a pressure cell showing well-formed gaskets – just prior to cell extraction. b) A cube that has been cut open using a Buehler Isomet 1000 Precision Saw.

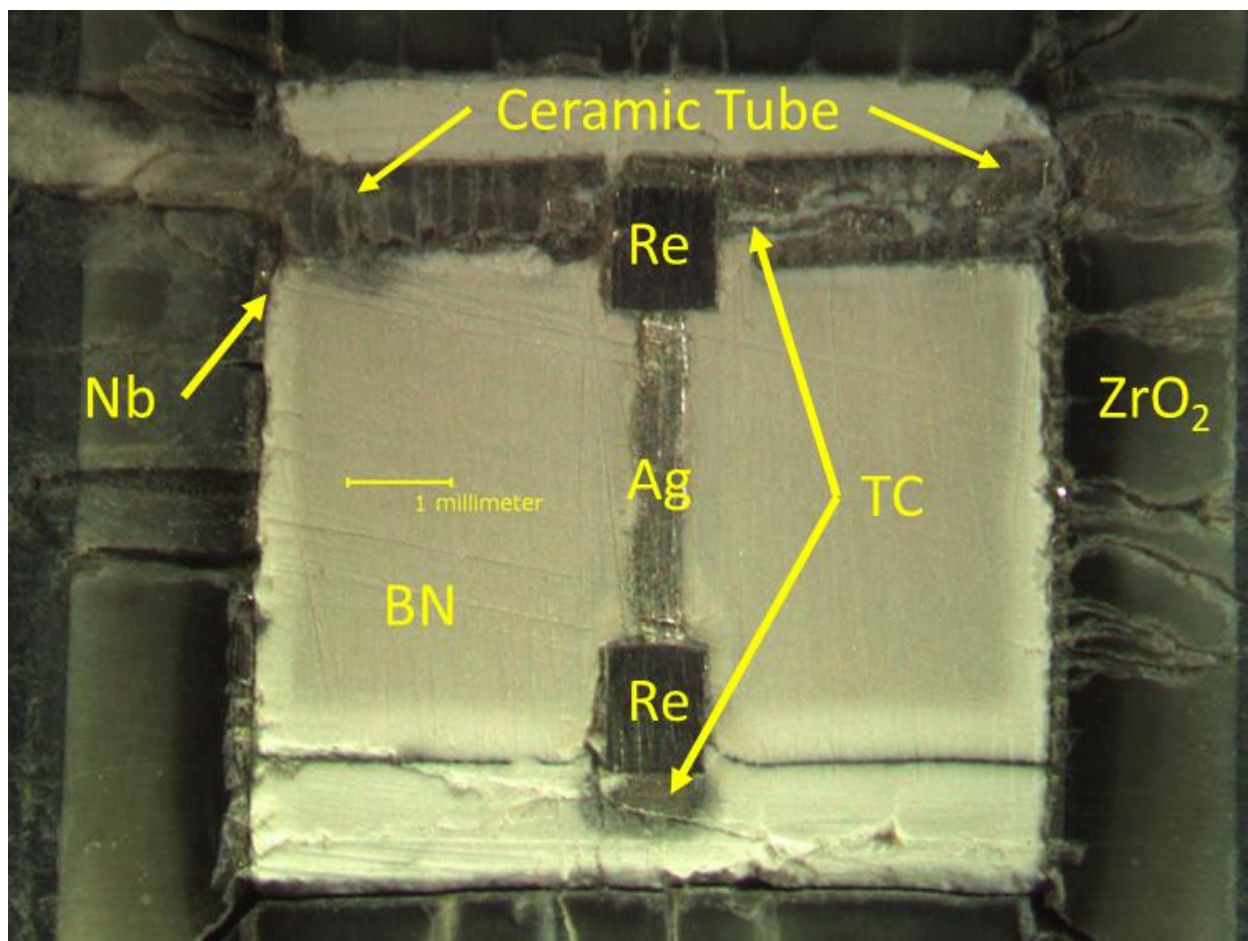


Figure C.3: Cross-section of a recovered 4 GPa experiment (~1600 K) using the cell design shown in Fig. C.1: Zirconia sleeve (ZrO₂); Niobium furnace (Nb); Boron nitride sample container (BN); Silver wire sample (Ag); 10 Rhenium plugs (Re); Thermocouple (TC).

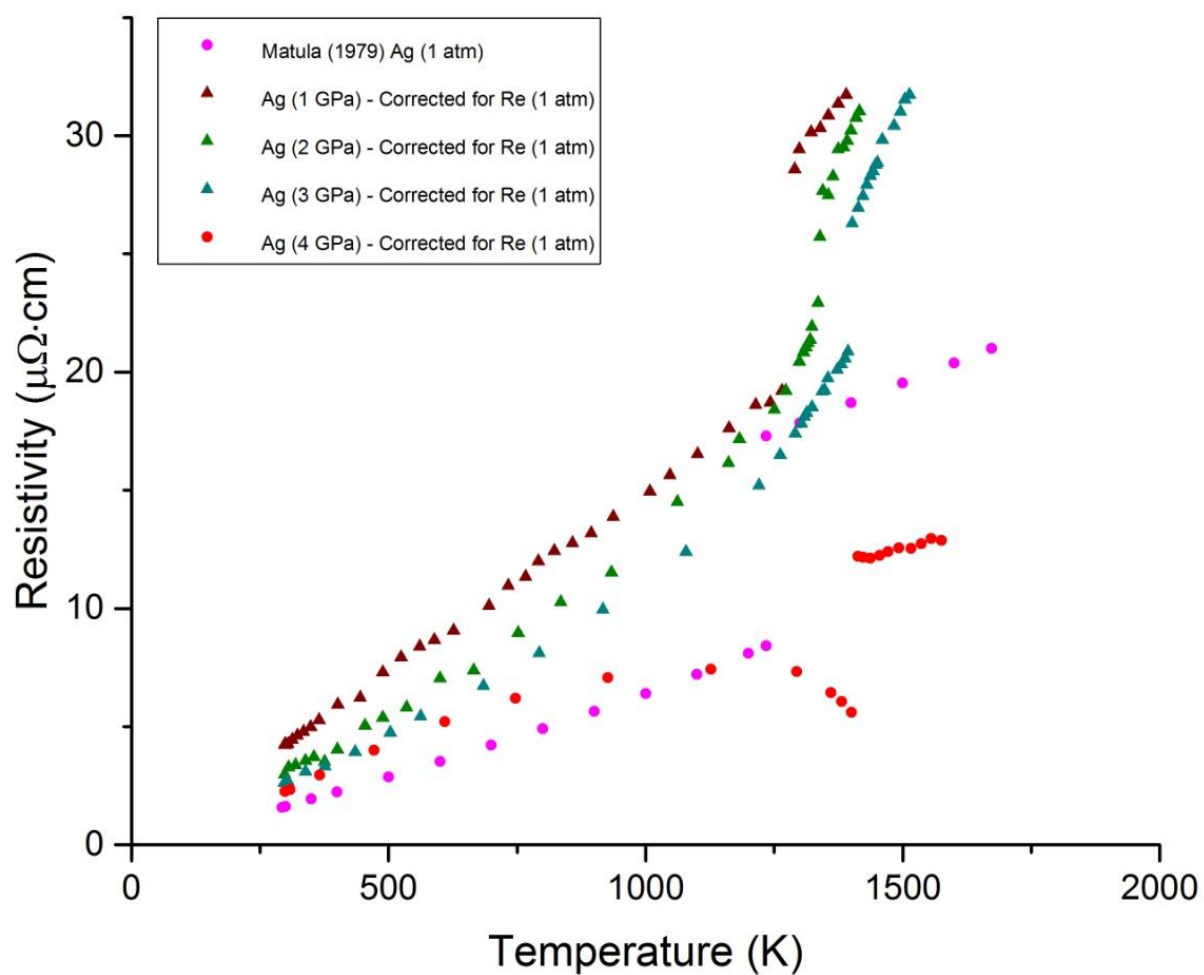


Figure C.4: Electrical resistivity of Ag as a function of temperature at pressures of 1, 2, 3 and 4 GPa utilizing the first cubic cell design, compared with 1 atm data.

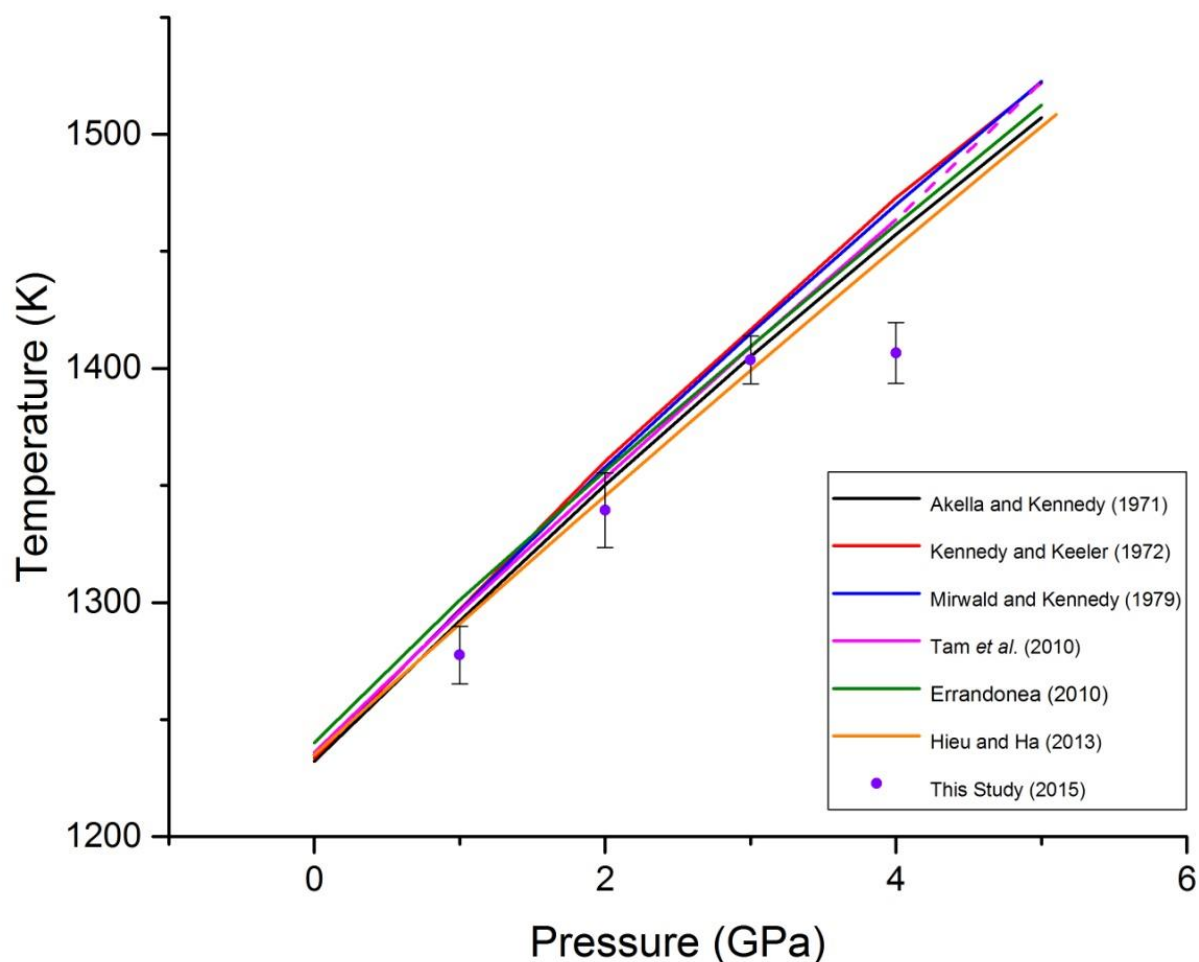


Figure C.5: Plot of melting temperatures of Ag as a function of pressure using the first cubic cell design. The lines represent experimental and theoretical melting temperatures from the literature compared with the observed melting points of Ag from experiments using the first cubic cell design. The bottoms and tops of the error bars indicate the highest measured temperature in the solid phase and the lowest measured temperature in the liquid phase, respectively. The experimental data from this study (indigo circles) are the averages of the bottom and top temperatures.

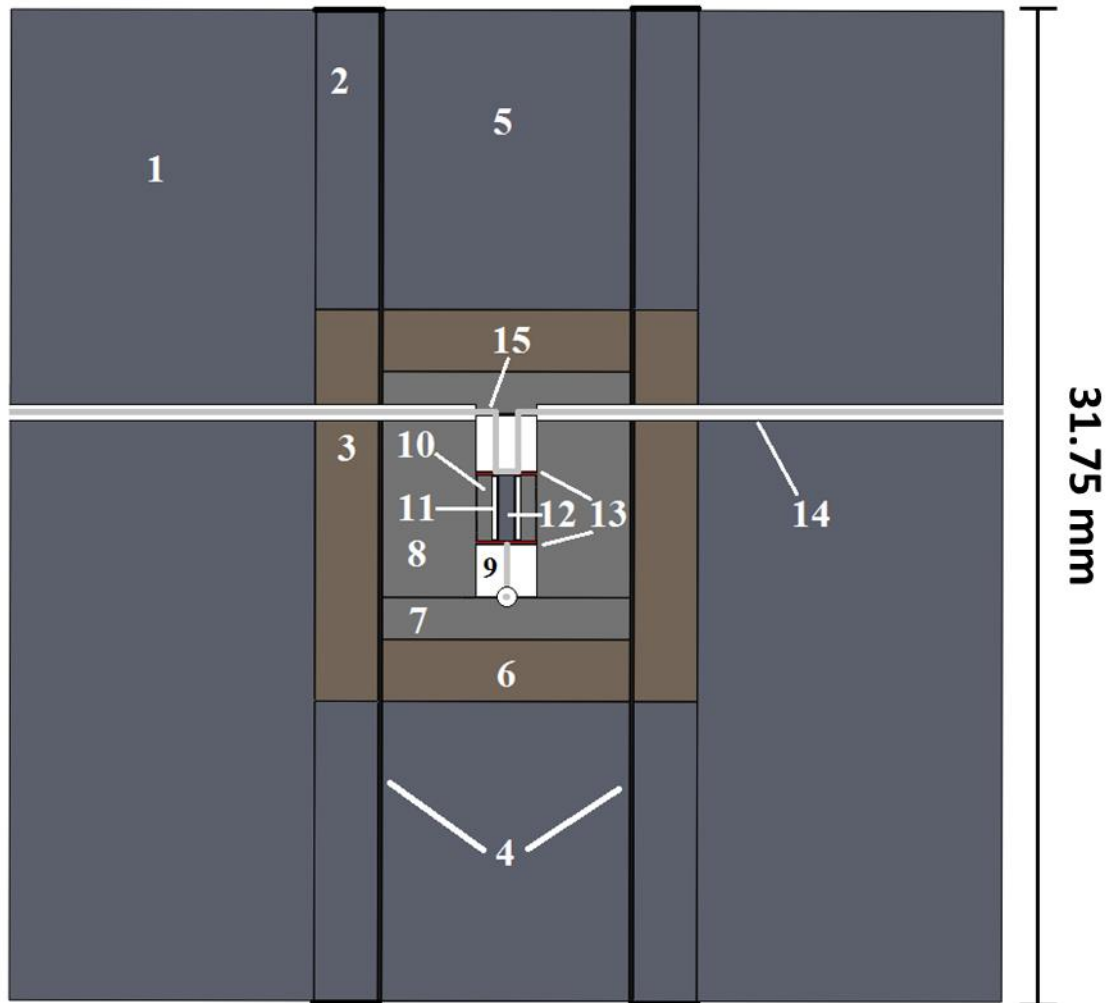


Figure C.6: Cross-section of an assembled cube using the second cell design. The thermocouple and Re foils are not to scale to emphasize location and shape. 1) Pyrophyllite cube; 2) Pyrophyllite sleeve; 3) Zirconia sleeve; 4) Niobium furnace; 5) Pyrophyllite plug; 6) Zirconia cap; 7) Boron nitride cap; 8) Boron nitride sample container; 9) Two-hole ceramic tube; 10) Boron nitride capsule; 11) Silver-bearing Ceramic tube; 12) Silver wire sample; 13) Re foils; 14) Ceramic Tube; 15) Thermocouple.

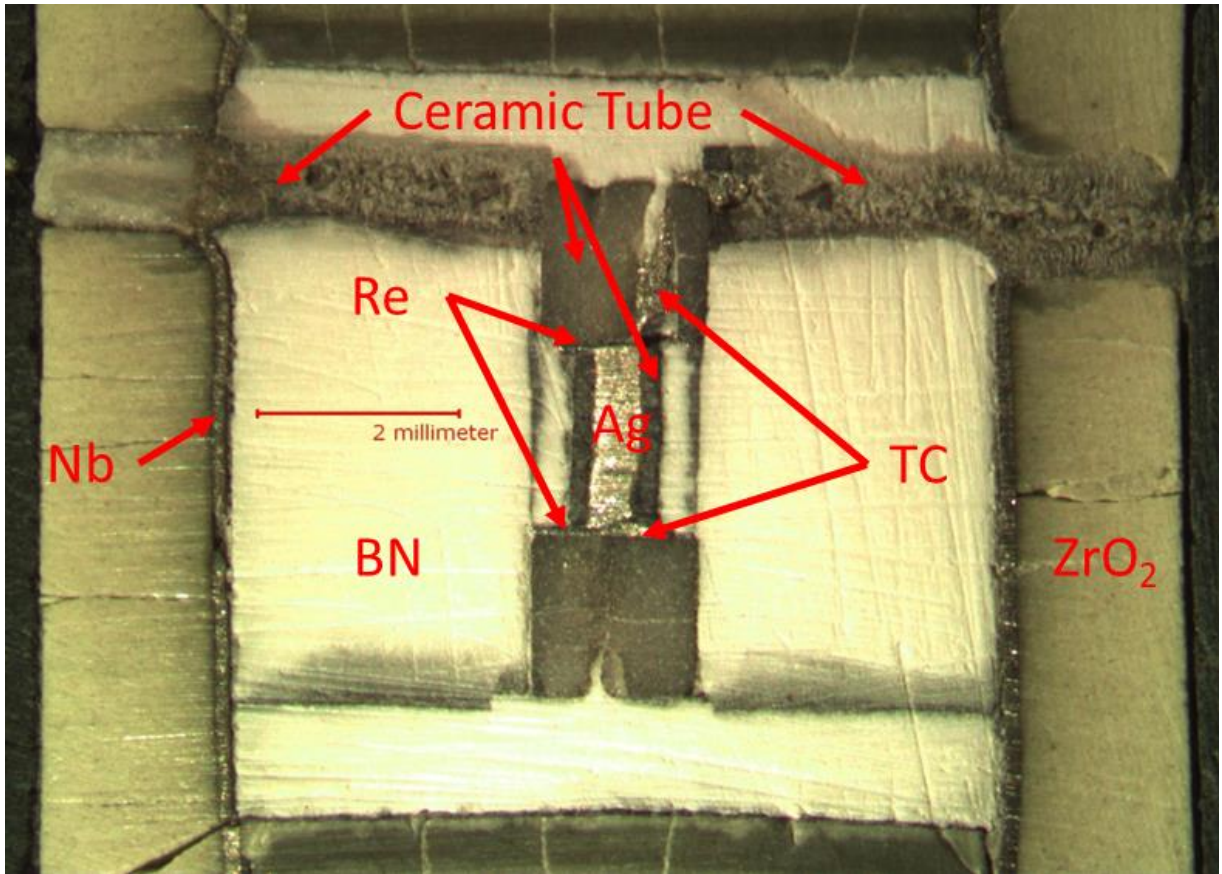


Figure C.7: Cross-section of a recovered 2 GPa experiment (~1383 K) using the cell design shown in Fig. C.6: Zirconia sleeve (ZrO₂); Niobium furnace (Nb); Boron nitride sample container (BN); Silver wire sample (Ag); 10 Rhenium disks (Re); Thermocouple (TC).

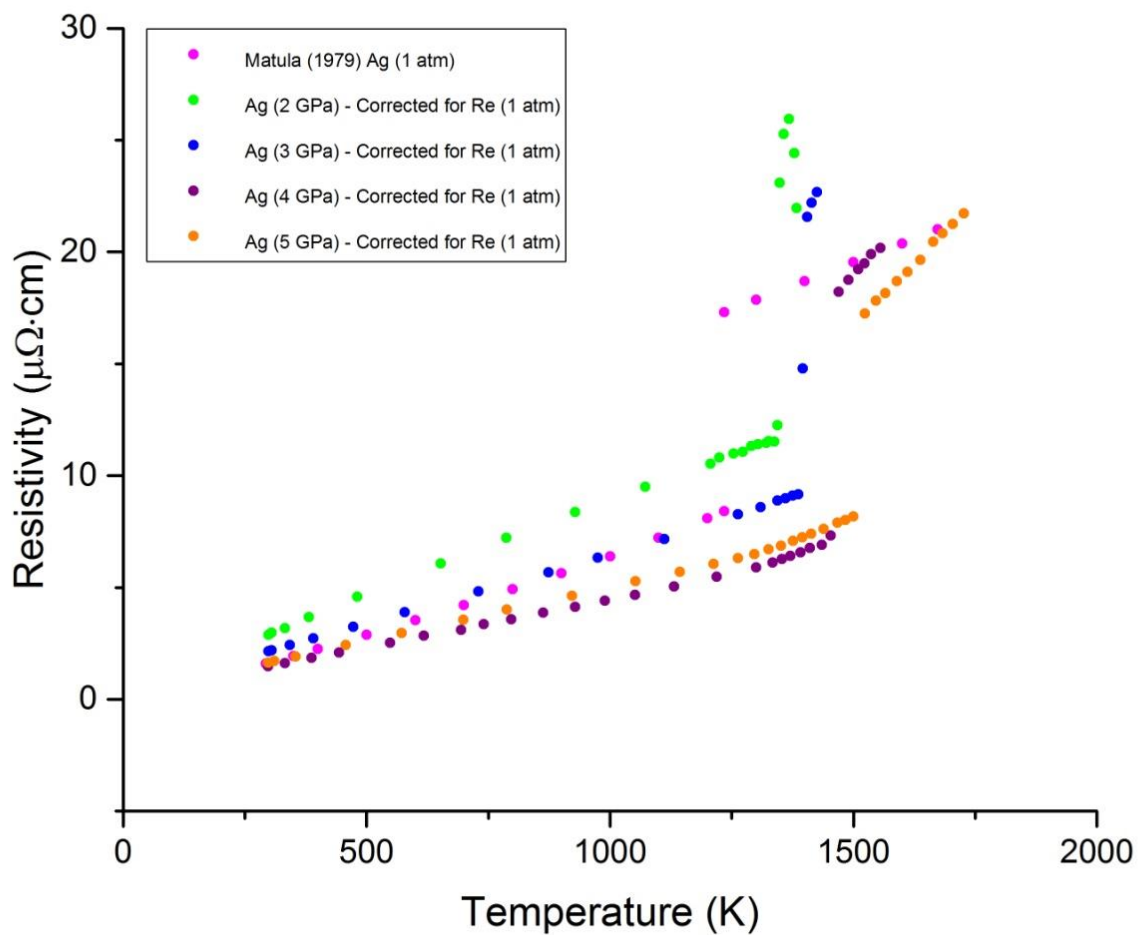


Figure C.8: Electrical resistivity of Ag as a function of temperature at pressures of 2, 3, 4 and 5 GPa utilizing the second cubic cell design, compared with 1 atm data.

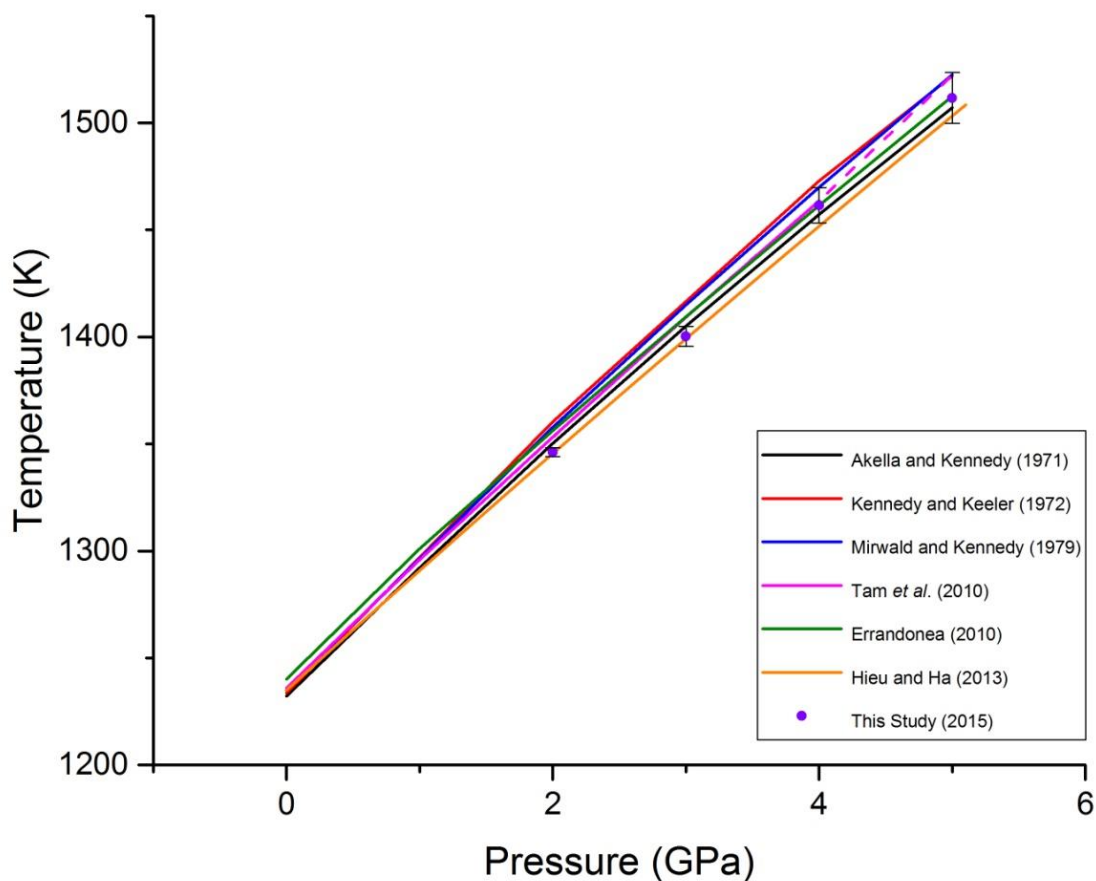


Figure C.9: Plot of melting temperatures of Ag as a function of pressure using the second cubic cell design. The lines represent experimental and theoretical melting temperatures from the literature compared with the observed melting points of Ag from experiments using the first cubic cell design. The bottoms and tops of the error bars indicate the highest measured temperature in the solid phase and the lowest measured temperature in the liquid phase, respectively. The experimental data from this study (indigo circles) are the averages of the bottom and top temperatures.

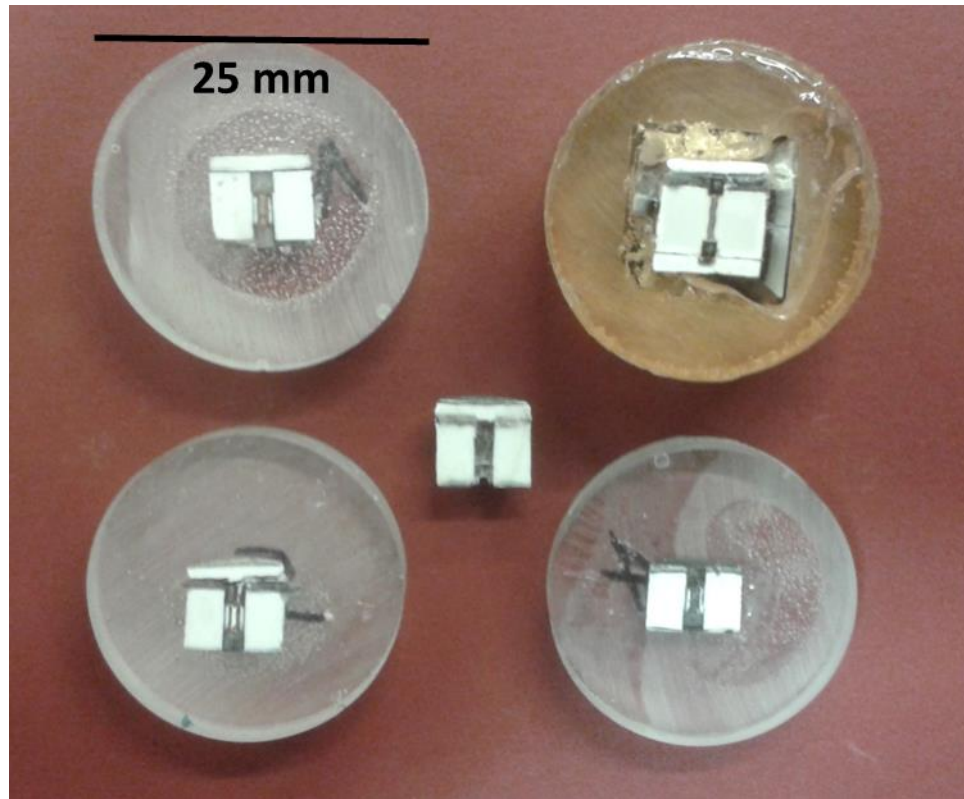


Figure C.10: Image of recovered experiments prepared in epoxy disks for EPMA.

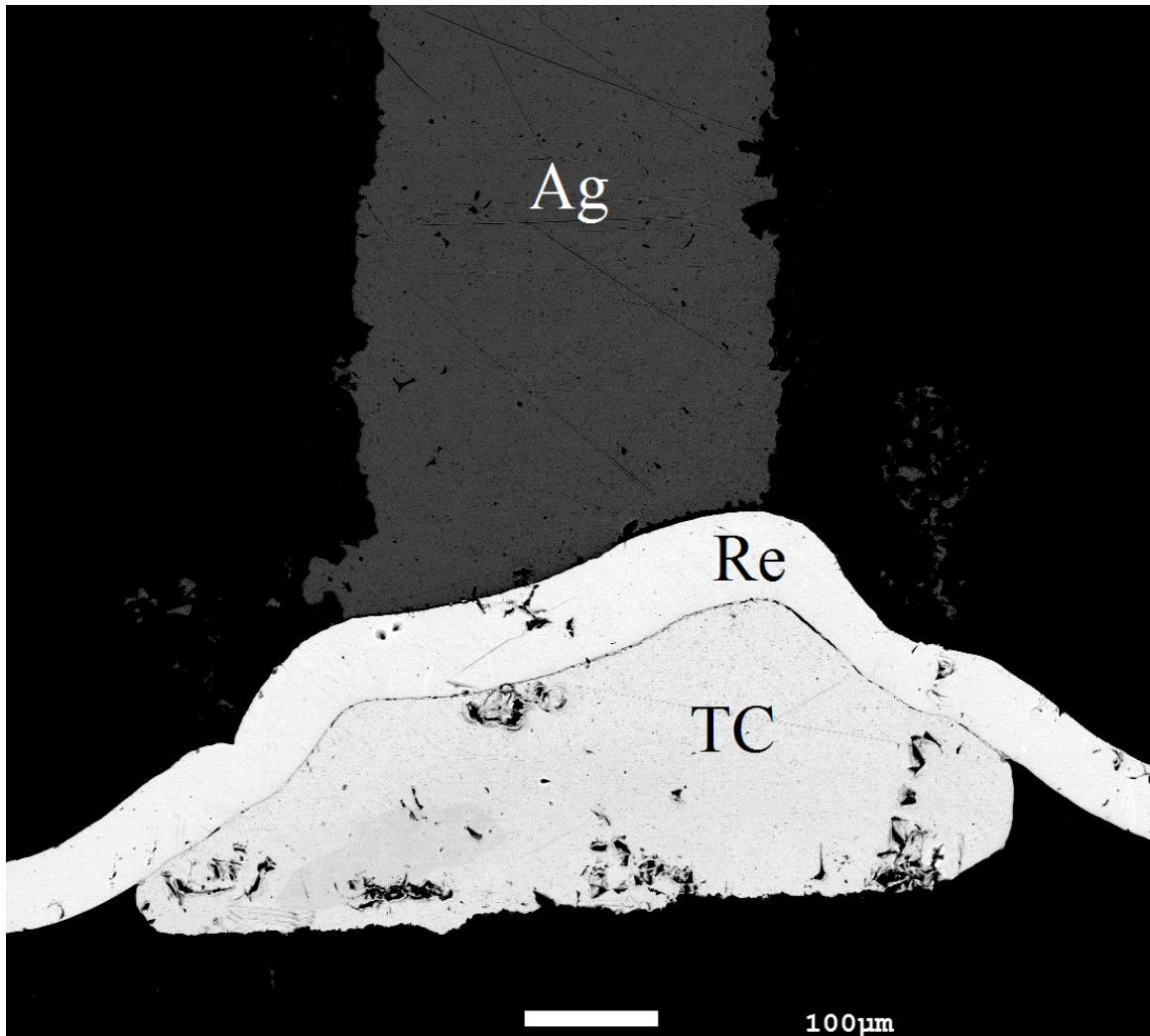


Figure C.11: Backscattered electron image of a recovered experiment from 4 GPa and ~1557 K. Type-S thermocouple (TC), Re foil, Ag wire sample components are labeled. Boundaries between metallic components are well-defined and lacking diffusion.

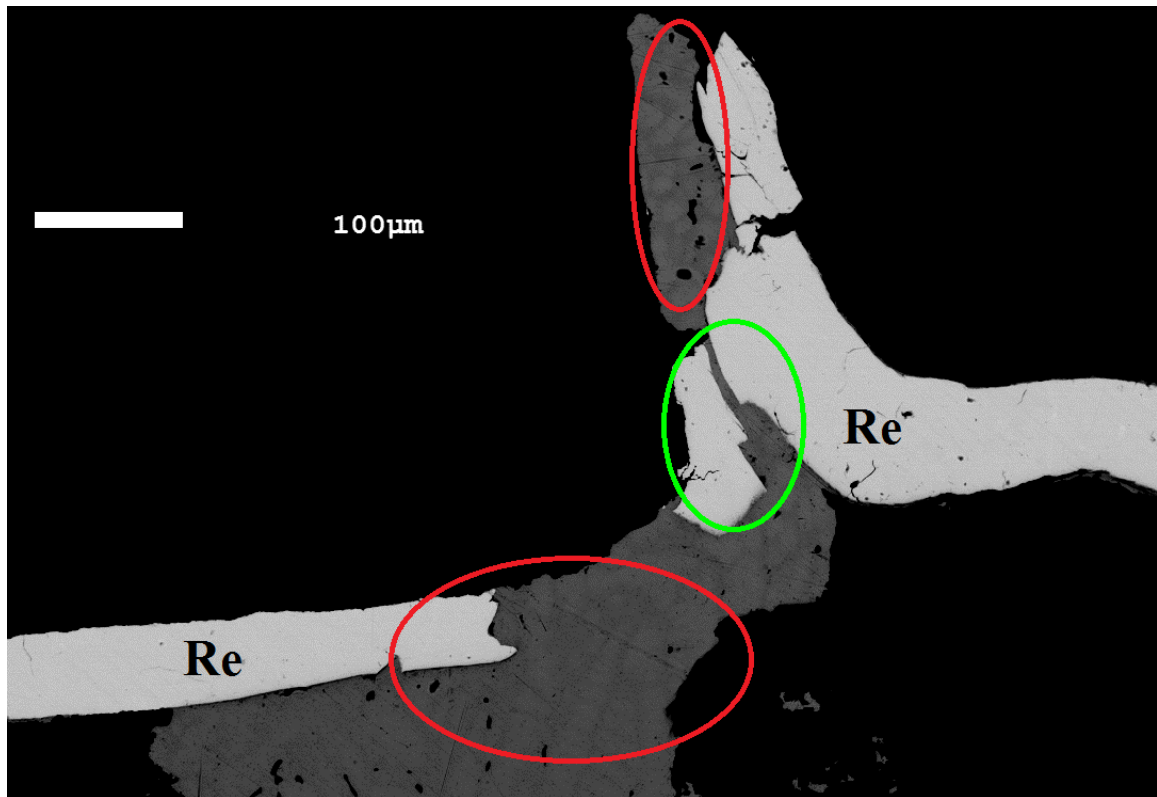


Figure C.12: Backscattered electron image of a recovered experiment from 4 GPa and ~1557 K with Re foil component labeled. The green circle encompasses an area of the Re foil that broke under pressure. This allowed liquid Ag (grey) to migrate to and contact the Type-S thermocouples (not shown – removed during sanding/polishing). Pt diffusion into Ag is observed by the mottled Ag wire sample, indicated within the red circles.

C.2 Iron sulphide

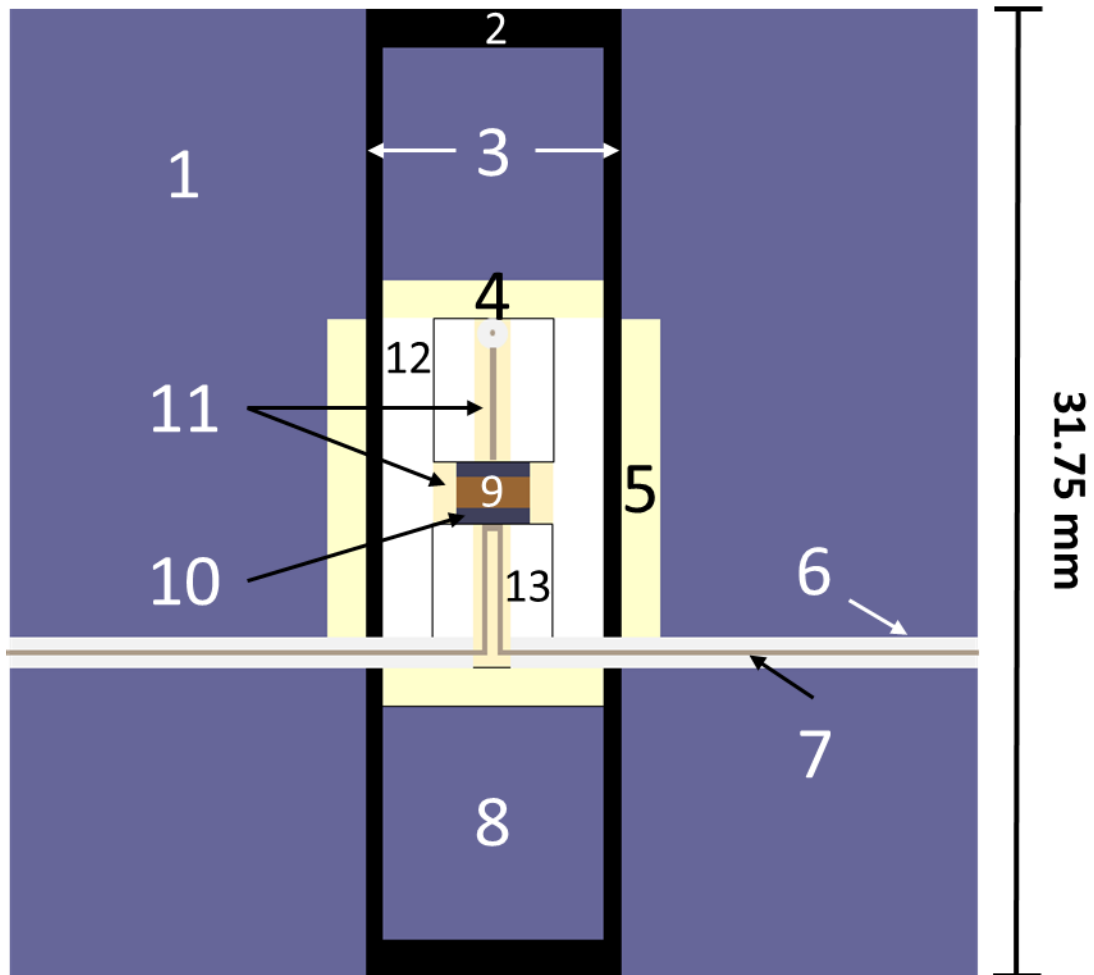


Figure C.13: Illustration of the cross-section of the first cubic pressure cell used in iron sulphide (FeS) experiments. 1) Pyrophyllite cube; 2) Graphite cap; 3) Graphite sleeve furnace; 4) Zirconia Cap; 5) Zirconia sleeve; 6) Mullite tube; 7) Type-S thermocouple; 8) Pyrophyllite plug; 9) FeS powder sample; 10) Tungsten caps; 11) Alumina tube; 12) Large boron nitride sleeve; 13) Small boron nitride sleeve.

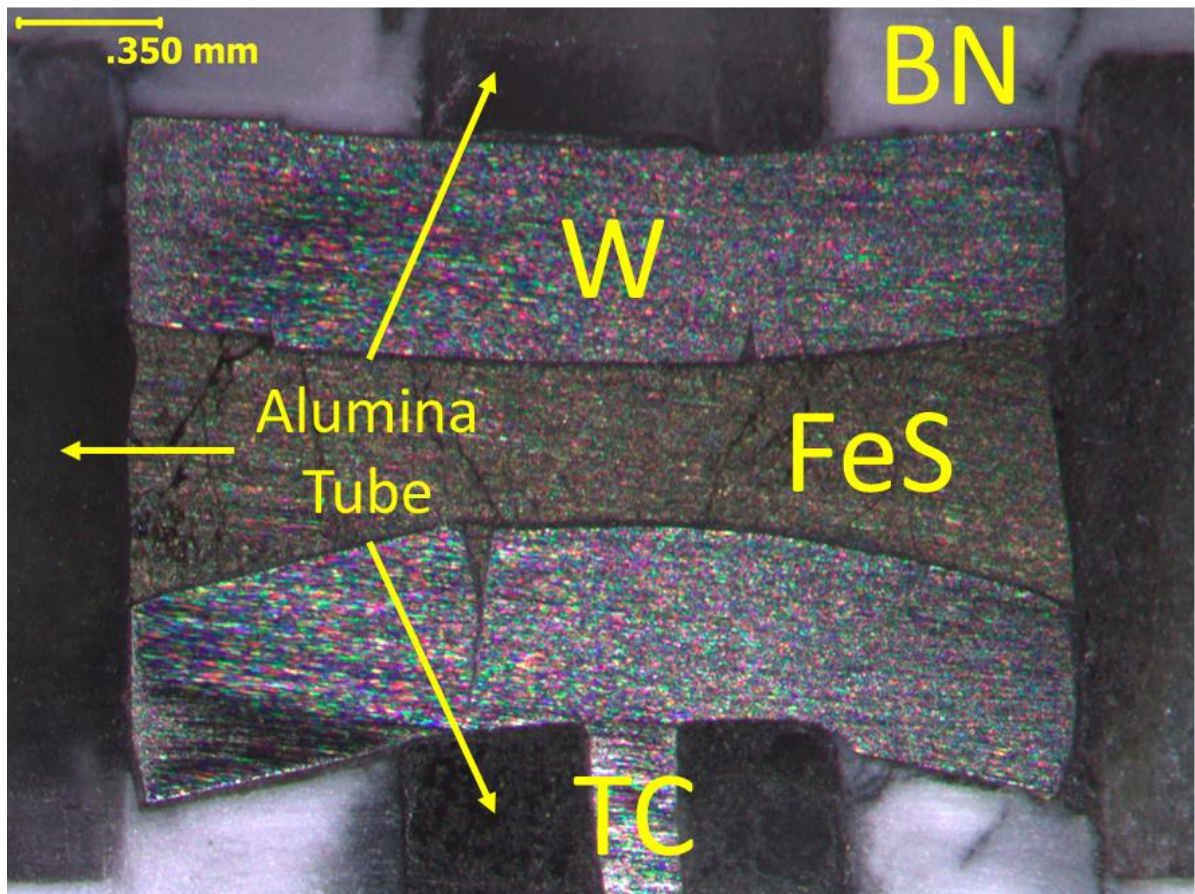


Figure C.14: Cross-section of a sample and disks recovered from a 2 GPa experiment (~1692 K) using the cell design in Fig. C.13: Tungsten (W) plugs/caps; iron sulphide (FeS) sample; Type-S thermocouple (TC) arm; boron nitride (BN).

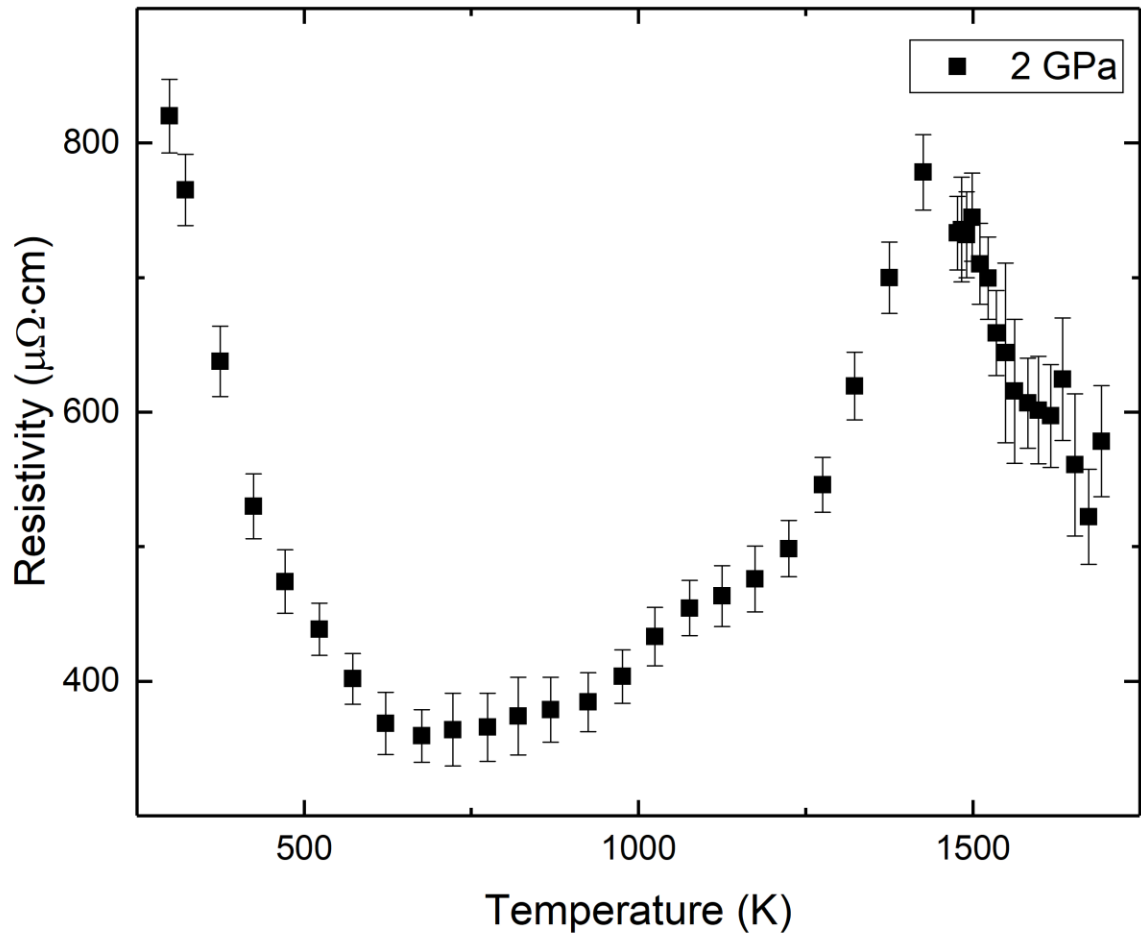


Figure C.15: Electrical resistivity of FeS as a function of temperature at 2 GPa utilizing the cell design in Fig. C.13.

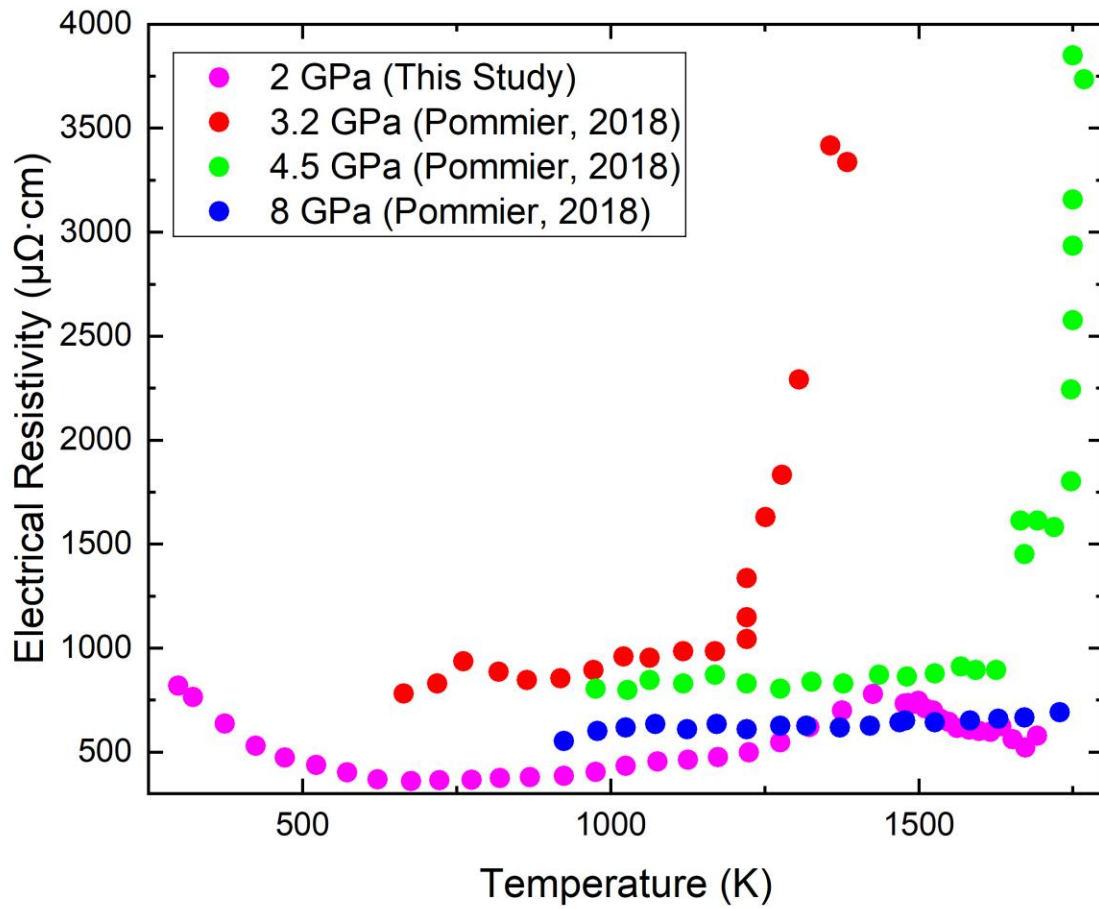


Figure C.16: Comparison of the resistivity of FeS at 2 GPa in Fig. C.14 to Pommier (2018).

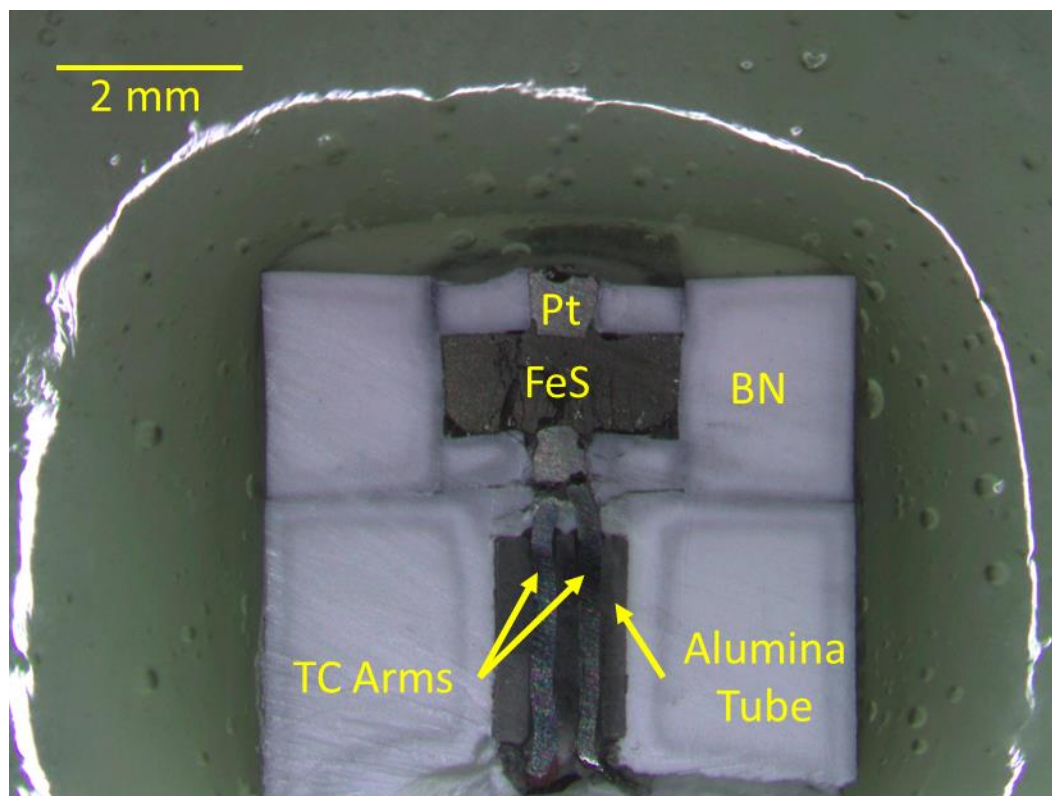


Figure C.17: Cross-section of a recovered 2 GPa experiment (~1671 K) using a modified cell design compared to Fig. C.13 embedded in epoxy. The second (upper) thermocouple and all other components were lost during grinding and polishing. The modification to the previous design includes replacing the single-holed alumina tube with boron nitride (BN) and the thick tungsten disks/caps with small platinum (Pt) plugs in the center of thin BN caps. Type-C thermocouples (TC) were used.

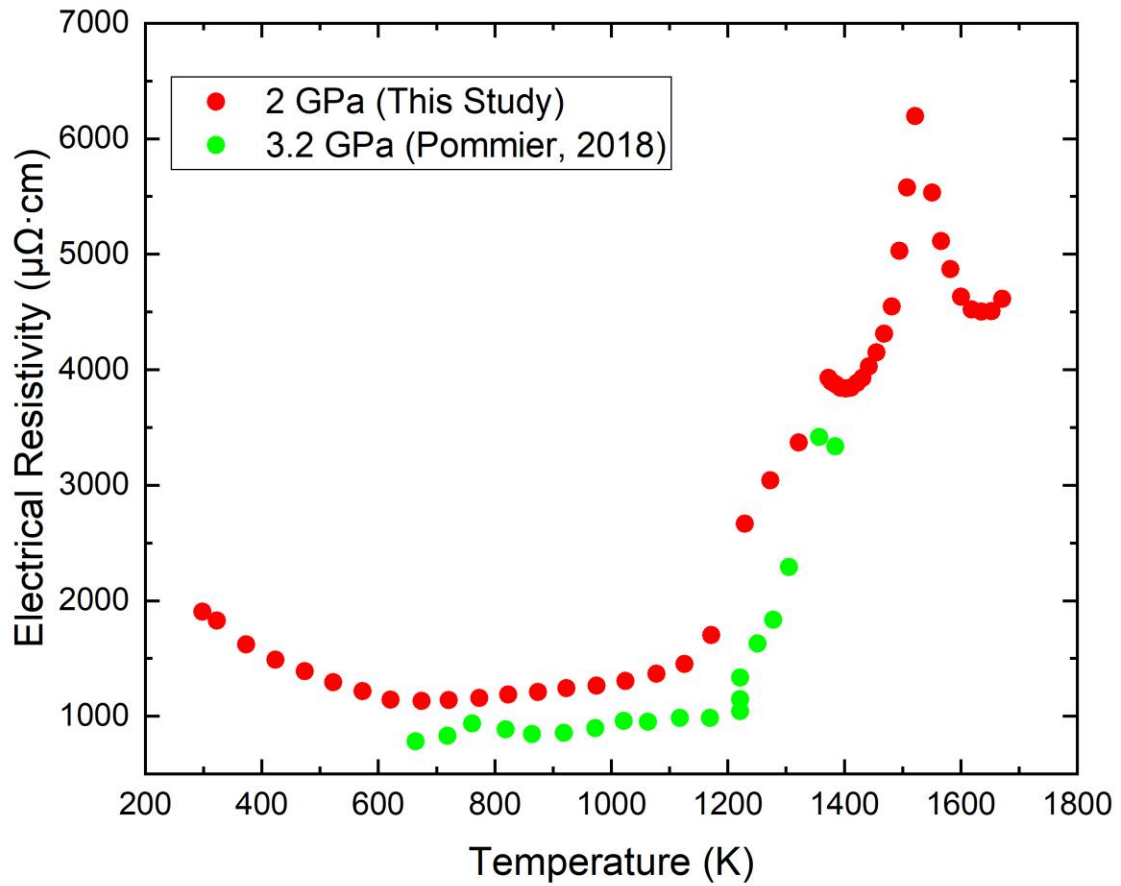


Figure C.18: Comparison of the electrical resistivity of FeS at 2 GPa (~1671 K) from the experiment shown in Fig. C.17, to Pommier (2018).

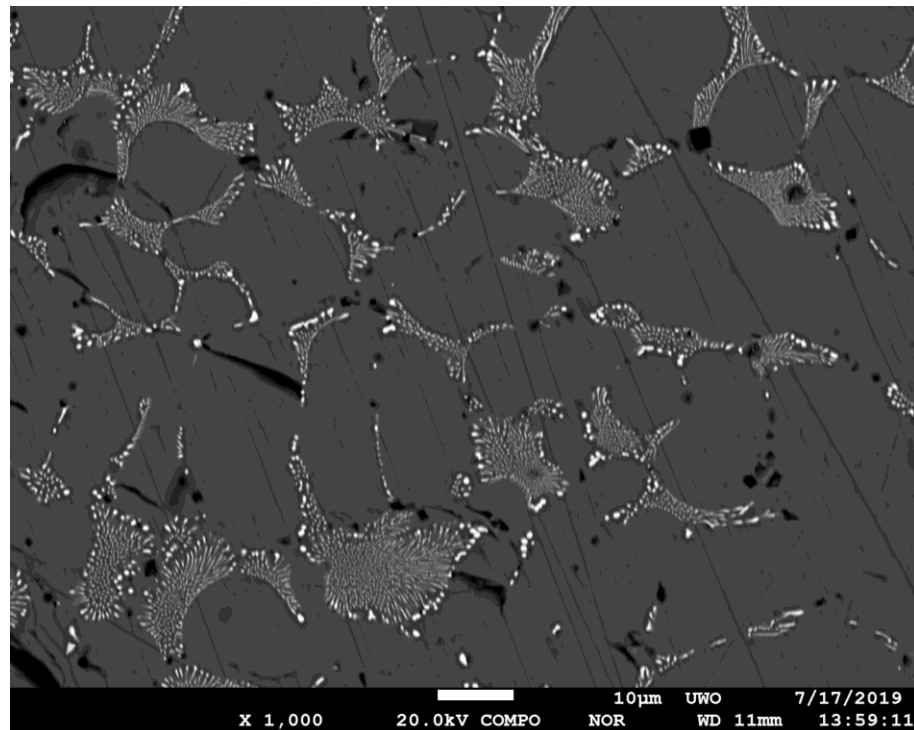
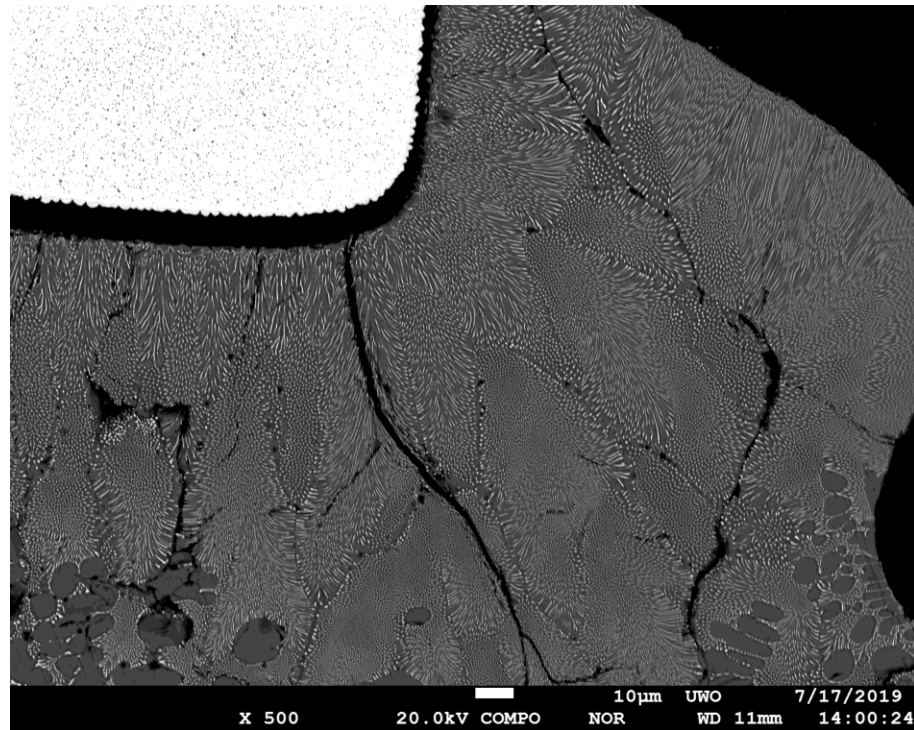
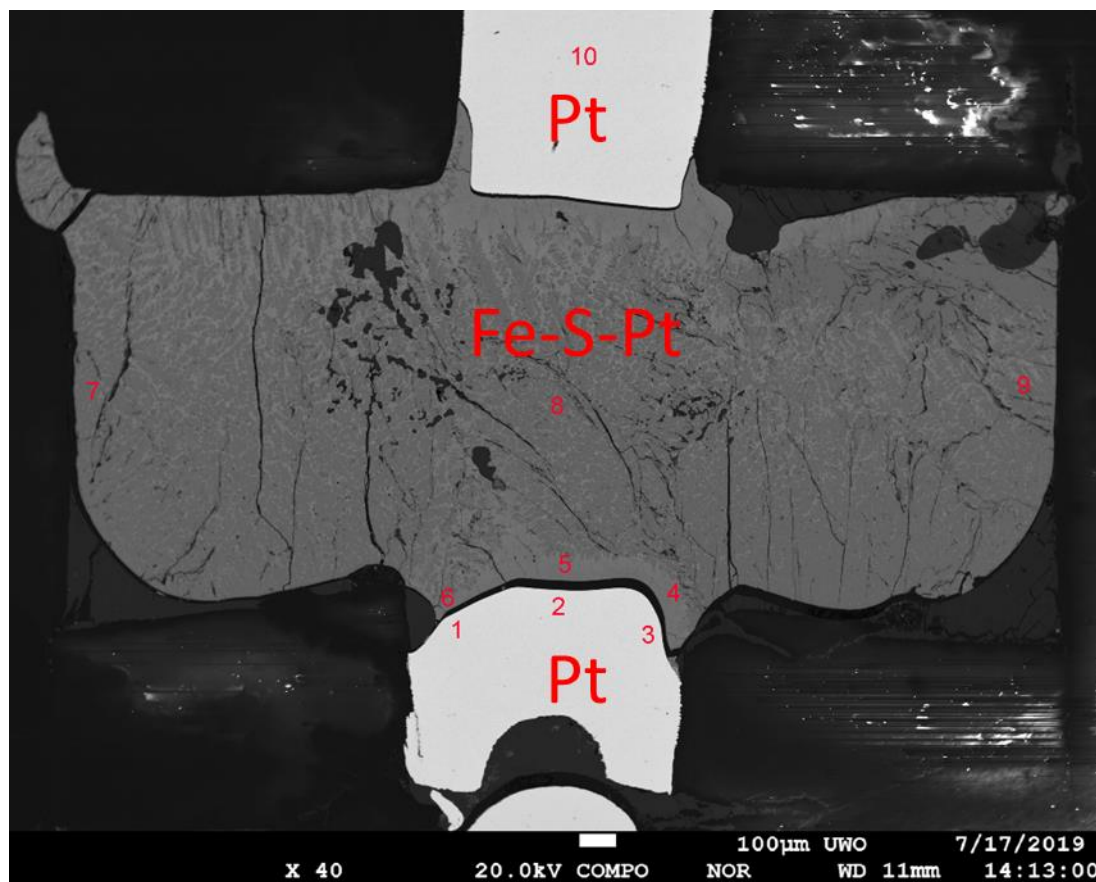


Figure C.19: Backscattered electron images of the recovered experiment shown in Fig. C.17 focused on the sample. Clearly observed are Fe-S-Pt (light grey) textures of the FeS sample (dark grey) due to diffusion of Pt (white).



Point	Comment	Si(Mass%)	Fe(Mass%)	S(Mass%)	Pt(Mass%)	W(Mass%)	Re(Mass%)	Total(Mass%)
1	FeS_01	nd	0.004	0.105	98.818	nd	nd	98.927
2	FeS_02	nd	0.01	0.108	99.206	nd	nd	99.324
3	FeS_03	nd	nd	0.093	99.385	nd	nd	99.478
4	FeS_04	nd	53.274	31.269	15.962	nd	nd	100.505
5	FeS_05	nd	53.287	31.441	15.266	nd	nd	99.994
6	FeS_06	nd	52.271	30.872	16.886	0.023	nd	100.052
7	FeS_07	nd	58.657	34.712	6.839	nd	nd	100.208
8	FeS_08	nd	59.166	35.005	4.23	0.006	nd	98.407
9	FeS_09	nd	54.608	32.697	13.613	0.023	nd	100.941
10	FeS_10	nd	nd	0.088	99.261	nd	nd	99.349
nd - not detected								

Figure C.20: Back-scattered electron image of the post-experiment 2 GPa (~1671 K) pressure cell shown in Fig. C.17. Results of the microprobe are given in the table.

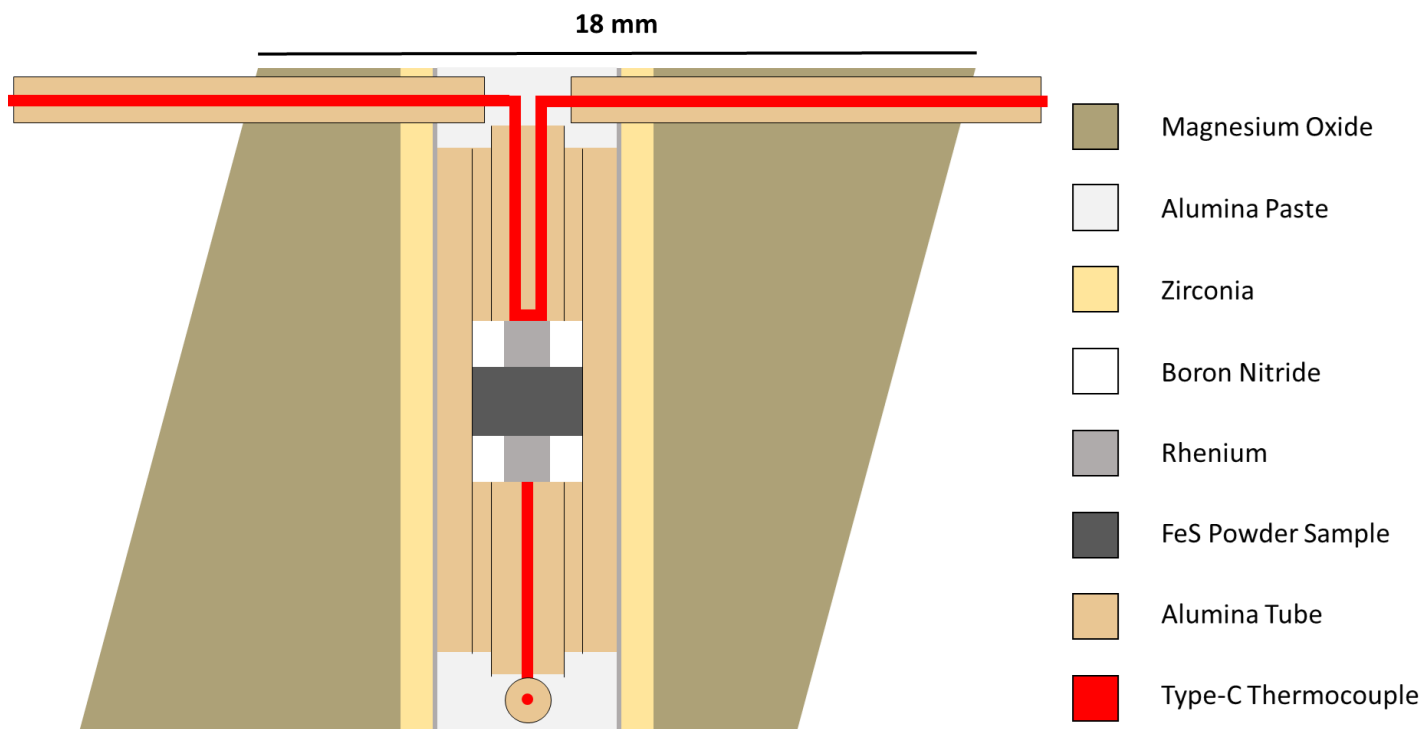


Figure C.21: Illustration of the cross-section of a multi-anvil octahedral pressure cell used for FeS experiments.

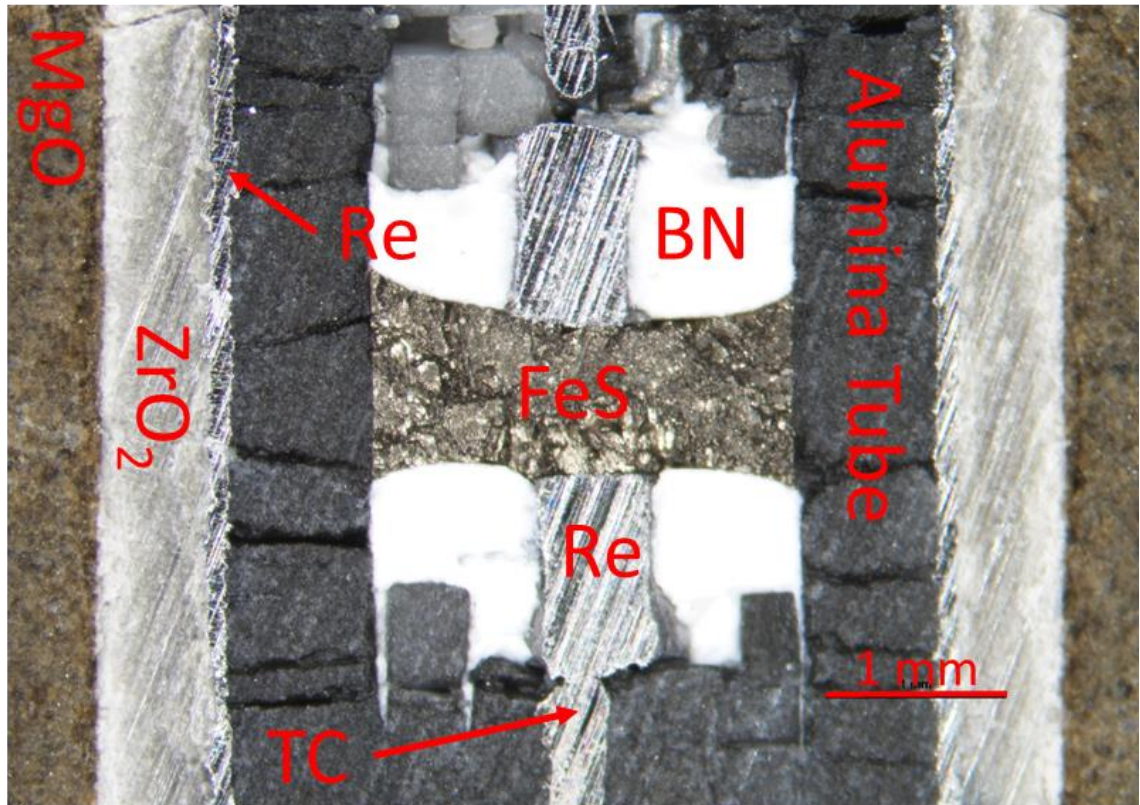


Figure C.22: Cross-section of a recovered 4 GPa experiment (~1772 K) using the cell design in Fig. C.21 focused on the sample: Rhenium (Re) plugs and furnace; iron sulphide (FeS) sample; Type-C thermocouple (TC) arm; boron nitride (BN) disks/caps; Zirconia (ZrO₂) sleeve; Magnesium oxide (MgO) pressure cell medium.

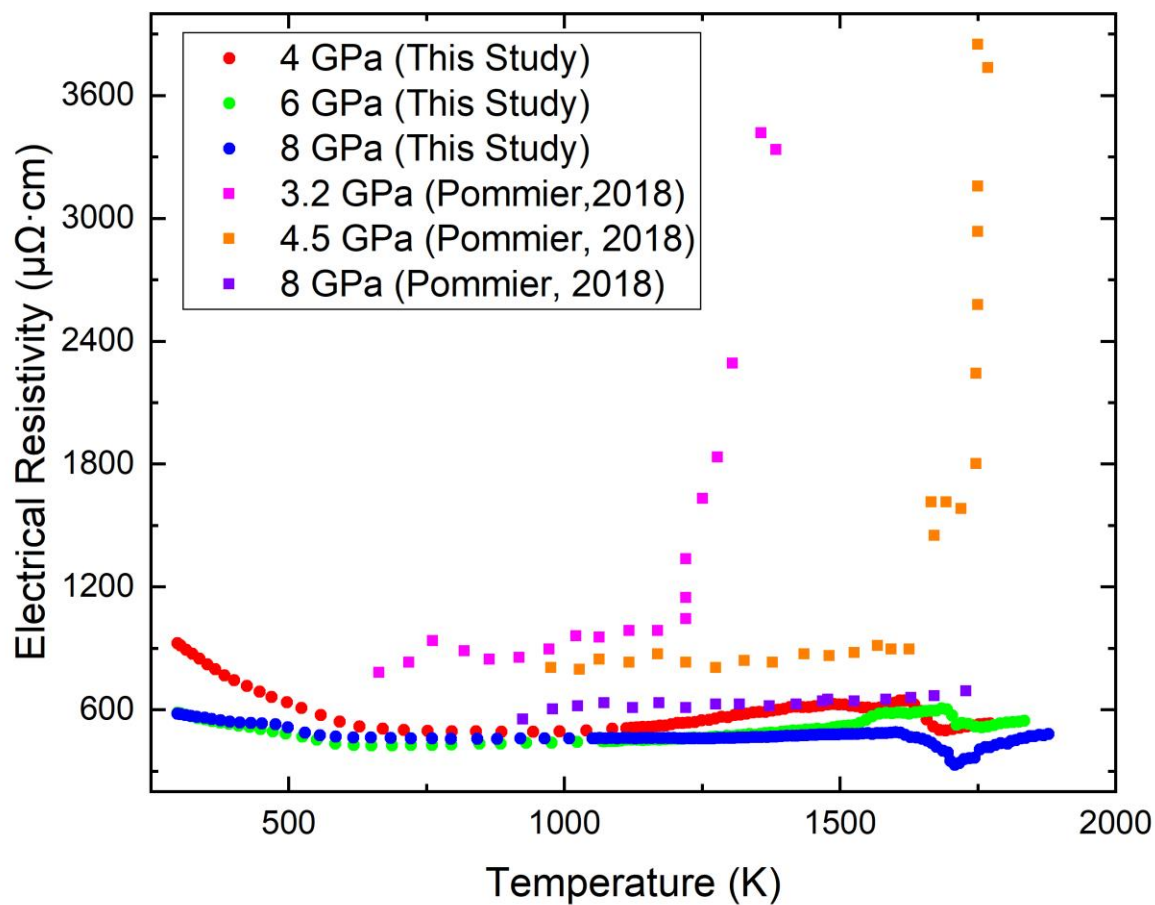


Figure C.23: Electrical resistivity of FeS using the multi-anvil cell design shown in Fig. C.21 with comparison to Pommier (2018).

Copyright Permission

This Agreement between Western University -- Joshua Littleton ("You") and John Wiley and Sons ("John Wiley and Sons") consists of your license details and the terms and conditions provided by John Wiley and Sons and Copyright Clearance Center.

License Number	5133081005247
License date	Aug 20, 2021
Licensed Content Publisher	John Wiley and Sons
Licensed Content Publication	Journal of Geophysical Research: Planets
Licensed Content Title	Electrical Resistivity of FeS at High Pressures and Temperatures: Implications of Thermal Transport in the Core of Ganymede
Licensed Content Author	Joshua A. H. Littleton, Richard A. Secco, Wenjun Yong
Licensed Content Date	May 11, 2021
Licensed Content Volume	126
Licensed Content Issue	5
Licensed Content Pages	18
Type of use	Dissertation/Thesis
Requestor type	Author of this Wiley article
Format	Print and electronic
Portion	Full article

Will you be translating?	No
Title	Heat Flow in the Core of Ganymede: High Pressure-Temperature Electrical Resistivity Measurements of Solid and Liquid Ag and Fe-S Alloys
Institution name	Western University
Expected presentation date	Sep 2021
Requestor Location	Western University 1151 Richmond Street N. London, ON N6A 5B7 Canada Attn: Western University
Publisher Tax ID	EU826007151
Total	0.00 CAD

TERMS AND CONDITIONS

This copyrighted material is owned by or exclusively licensed to John Wiley & Sons, Inc. or one of its group companies (each a "Wiley Company") or handled on behalf of a society with which a Wiley Company has exclusive publishing rights in relation to a particular work (collectively "WILEY"). By clicking "accept" in connection with completing this licensing transaction, you agree that the following terms and conditions apply to this transaction (along with the billing and payment terms and conditions established by the Copyright Clearance Center Inc., ("CCC's Billing and Payment terms and conditions"), at the time that you opened your RightsLink account (these are available at any time at <http://myaccount.copyright.com>).

Terms and Conditions

- The materials you have requested permission to reproduce or reuse (the "Wiley Materials") are protected by copyright.
- You are hereby granted a personal, non-exclusive, non-sub licensable (on a stand-alone basis), non-transferable, worldwide, limited license to reproduce the Wiley Materials for the purpose specified in the licensing process. This license, **and any CONTENT (PDF or image file) purchased as part of your order**, is for a one-time use only and limited to any maximum distribution number specified in the license. The first instance of republication or reuse granted by this license must be completed within two years of the date of the grant of this license (although copies prepared before the end date may be distributed thereafter). The Wiley Materials shall not be used in any other manner or for any other purpose, beyond what is granted in the license. Permission is granted subject to an appropriate acknowledgement given to the author, title of the material/book/journal and the publisher. You shall also duplicate the copyright notice that appears in the Wiley publication in your use of the Wiley Material. Permission is also granted on the understanding that nowhere in the text is a previously published source acknowledged for all or part of this Wiley Material. Any third party content is expressly excluded from this permission.
- With respect to the Wiley Materials, all rights are reserved. Except as expressly granted by the terms of the license, no part of the Wiley Materials may be copied, modified, adapted (except for minor reformatting required by the new Publication), translated, reproduced, transferred or distributed, in any form or by any means, and no derivative works may be made based on the Wiley Materials without the prior permission of the respective copyright owner. **For STM Signatory Publishers clearing permission under the terms of the STM Permissions Guidelines only, the terms of the license are extended to include subsequent editions and for editions in other languages, provided such editions are for the work as a whole in situ and does not involve the separate exploitation of the permitted figures**

or extracts, You may not alter, remove or suppress in any manner any copyright, trademark or other notices displayed by the Wiley Materials. You may not license, rent, sell, loan, lease, pledge, offer as security, transfer or assign the Wiley Materials on a stand-alone basis, or any of the rights granted to you hereunder to any other person.

- The Wiley Materials and all of the intellectual property rights therein shall at all times remain the exclusive property of John Wiley & Sons Inc, the Wiley Companies, or their respective licensors, and your interest therein is only that of having possession of and the right to reproduce the Wiley Materials pursuant to Section 2 herein during the continuance of this Agreement. You agree that you own no right, title or interest in or to the Wiley Materials or any of the intellectual property rights therein. You shall have no rights hereunder other than the license as provided for above in Section 2. No right, license or interest to any trademark, trade name, service mark or other branding ("Marks") of WILEY or its licensors is granted hereunder, and you agree that you shall not assert any such right, license or interest with respect thereto
- NEITHER WILEY NOR ITS LICENSORS MAKES ANY WARRANTY OR REPRESENTATION OF ANY KIND TO YOU OR ANY THIRD PARTY, EXPRESS, IMPLIED OR STATUTORY, WITH RESPECT TO THE MATERIALS OR THE ACCURACY OF ANY INFORMATION CONTAINED IN THE MATERIALS, INCLUDING, WITHOUT LIMITATION, ANY IMPLIED WARRANTY OF MERCHANTABILITY, ACCURACY, SATISFACTORY QUALITY, FITNESS FOR A PARTICULAR PURPOSE, USABILITY, INTEGRATION OR NON-INFRINGEMENT AND ALL SUCH WARRANTIES ARE HEREBY EXCLUDED BY WILEY AND ITS LICENSORS AND WAIVED BY YOU.
- WILEY shall have the right to terminate this Agreement immediately upon breach of this Agreement by you.
- You shall indemnify, defend and hold harmless WILEY, its Licensors and their respective directors, officers, agents and employees, from and against any actual or

threatened claims, demands, causes of action or proceedings arising from any breach of this Agreement by you.

- IN NO EVENT SHALL WILEY OR ITS LICENSORS BE LIABLE TO YOU OR ANY OTHER PARTY OR ANY OTHER PERSON OR ENTITY FOR ANY SPECIAL, CONSEQUENTIAL, INCIDENTAL, INDIRECT, EXEMPLARY OR PUNITIVE DAMAGES, HOWEVER CAUSED, ARISING OUT OF OR IN CONNECTION WITH THE DOWNLOADING, PROVISIONING, VIEWING OR USE OF THE MATERIALS REGARDLESS OF THE FORM OF ACTION, WHETHER FOR BREACH OF CONTRACT, BREACH OF WARRANTY, TORT, NEGLIGENCE, INFRINGEMENT OR OTHERWISE (INCLUDING, WITHOUT LIMITATION, DAMAGES BASED ON LOSS OF PROFITS, DATA, FILES, USE, BUSINESS OPPORTUNITY OR CLAIMS OF THIRD PARTIES), AND WHETHER OR NOT THE PARTY HAS BEEN ADVISED OF THE POSSIBILITY OF SUCH DAMAGES. THIS LIMITATION SHALL APPLY NOTWITHSTANDING ANY FAILURE OF ESSENTIAL PURPOSE OF ANY LIMITED REMEDY PROVIDED HEREIN.
- Should any provision of this Agreement be held by a court of competent jurisdiction to be illegal, invalid, or unenforceable, that provision shall be deemed amended to achieve as nearly as possible the same economic effect as the original provision, and the legality, validity and enforceability of the remaining provisions of this Agreement shall not be affected or impaired thereby.
- The failure of either party to enforce any term or condition of this Agreement shall not constitute a waiver of either party's right to enforce each and every term and condition of this Agreement. No breach under this agreement shall be deemed waived or excused by either party unless such waiver or consent is in writing signed by the party granting such waiver or consent. The waiver by or consent of a party to a breach of any provision of this Agreement shall not operate or be construed as a waiver of or consent to any other or subsequent breach by such other party.
- This Agreement may not be assigned (including by operation of law or otherwise) by you without WILEY's prior written consent.

- Any fee required for this permission shall be non-refundable after thirty (30) days from receipt by the CCC.
- These terms and conditions together with CCC's Billing and Payment terms and conditions (which are incorporated herein) form the entire agreement between you and WILEY concerning this licensing transaction and (in the absence of fraud) supersedes all prior agreements and representations of the parties, oral or written. This Agreement may not be amended except in writing signed by both parties. This Agreement shall be binding upon and inure to the benefit of the parties' successors, legal representatives, and authorized assigns.
- In the event of any conflict between your obligations established by these terms and conditions and those established by CCC's Billing and Payment terms and conditions, these terms and conditions shall prevail.
- WILEY expressly reserves all rights not specifically granted in the combination of (i) the license details provided by you and accepted in the course of this licensing transaction, (ii) these terms and conditions and (iii) CCC's Billing and Payment terms and conditions.
- This Agreement will be void if the Type of Use, Format, Circulation, or Requestor Type was misrepresented during the licensing process.
- This Agreement shall be governed by and construed in accordance with the laws of the State of New York, USA, without regards to such state's conflict of law rules. Any legal action, suit or proceeding arising out of or relating to these Terms and Conditions or the breach thereof shall be instituted in a court of competent jurisdiction in New York County in the State of New York in the United States of America and each party hereby consents and submits to the personal jurisdiction of such court, waives any objection to venue in such court and consents to service of process by registered or certified mail, return receipt requested, at the last known address of such party.

WILEY OPEN ACCESS TERMS AND CONDITIONS

Wiley Publishes Open Access Articles in fully Open Access Journals and in Subscription journals offering Online Open. Although most of the fully Open Access journals publish

open access articles under the terms of the Creative Commons Attribution (CC BY) License only, the subscription journals and a few of the Open Access Journals offer a choice of Creative Commons Licenses. The license type is clearly identified on the article.

The Creative Commons Attribution License

The Creative Commons Attribution License (CC-BY) allows users to copy, distribute and transmit an article, adapt the article and make commercial use of the article. The CC-BY license permits commercial and non-

Creative Commons Attribution Non-Commercial License

The Creative Commons Attribution Non-Commercial (CC-BY-NC) License permits use, distribution and reproduction in any medium, provided the original work is properly cited and is not used for commercial purposes.(see below)

Creative Commons Attribution-Non-Commercial-NoDerivs License

The Creative Commons Attribution Non-Commercial-NoDerivs License (CC-BY-NC-ND) permits use, distribution and reproduction in any medium, provided the original work is properly cited, is not used for commercial purposes and no modifications or adaptations are made. (see below)

Use by commercial "for-profit" organizations

Use of Wiley Open Access articles for commercial, promotional, or marketing purposes requires further explicit permission from Wiley and will be subject to a fee.

Further details can be found on Wiley Online Library
<http://olabout.wiley.com/WileyCDA/Section/id-410895.html>

Chapter 3: Littleton, J.A.H., Secco, R.A. and Yong, W. 2018. Decreasing electrical resistivity of silver along the melting boundary up to 5 GPa. *High Pressure Research*. 38(2): 99-106. DOI: 10.1080/08957959.2018.1435786

This is an Accepted Manuscript version of the following article, accepted for publication in *High Pressure Research*. It is deposited under the terms of the Creative Commons Attribution-NonCommercial License (<http://creativecommons.org/licenses/by-nc/4.0/>), which permits non-commercial re-use, distribution, and reproduction in any medium, provided the original work is properly cited.

Chapter 5: Littleton, J.A.H., Secco, R.A. and Yong, W. 2021. Thermal Convection in the Core of Ganymede Inferred from Liquid Eutectic Fe-FeS Electrical Resistivity at High Pressures. *Crystals*. 11(8): 875. DOI: 10.3390/cryst11060705

For all articles published in MDPI journals, copyright is retained by the authors. Articles are licensed under an open access Creative Commons CC BY 4.0 license, meaning that anyone may download and read the paper for free. In addition, the article may be reused and quoted provided that the original published version is cited. These conditions allow for maximum use and exposure of the work, while ensuring that the authors receive proper credit.

No special permission is required to reuse all or part of article published by MDPI, including figures and tables. For articles published under an open access Creative Common CC BY license, any part of the article may be reused without permission provided that the original article is clearly cited. Reuse of an article does not imply endorsement by the authors or MDPI.

In exceptional circumstances articles may be licensed differently. If you have specific condition (such as one linked to funding) that does not allow this license, please mention this to the editorial office of the journal at submission. Exceptions will be granted at the discretion of the publisher.

Curriculum Vitae

Name: Joshua Andrew Henry Littleton

Post-secondary Education and Degrees: Ph.D. in Geophysics
The University of Western Ontario (Western University)
London, Ontario, Canada
2016-2021

B.Sc. Honors Specialization in Geophysics + Major in Geology
The University of Western Ontario (Western University)
London, Ontario, Canada
2010-2016

Honours and Awards: Geophysics Travel Scholarship
2020-2021

Alexander Graham Bell Canada Graduate Scholarship (NSERC) -
Doctoral
2019-2021

Collett Graduate Scholarship (KEGS)
2019-2020

Robert and Ruth Lumsden Fellowship in Science
2019-2020

Queen Elizabeth II Graduate Scholarship in Science and
Technology
2017-2018, 2018-2019

Western Graduate Research Scholarship
2016-2017, 2017-2018, 2018-2019

Faculty of Science Graduate Student Teaching Award
2017-2018

Ontario Graduate Scholarship
2016-2017

Misasa International Student Internship Program 2016 Award
2016

Charles M. Carmichael Prize in Earth Sciences

2015-2016

Undergraduate Student Research Award (NSERC)

2014-2015, 2015-2016

London Police Services Board Award

2010-2011, 2011-2012, 2012-2013, 2013-2014, 2014-2015

**Related Work
Experience**

Graduate Research Assistant

The University of Western Ontario (Western University)

2016-2021

Graduate Teaching Assistant

The University of Western Ontario (Western University)

2016-2021

Undergraduate Research Assistant (Earth Sciences Department)

The University of Western Ontario (Western University)

2015-2016

Undergraduate Research Assistant (Chemistry Department)

The University of Western Ontario (Western University)

2014

Publications:

11. **Littleton, J.A.H.**, Secco, R.A. and Yong, W. 2021. Thermal convection in the core of Ganymede inferred from liquid eutectic Fe-FeS electrical resistivity at high pressures. *Crystals*. 11(8): 875. DOI: 10.3390/cryst11080875

10. **Littleton, J.A.H.**, Secco, R.A. and Yong, W. 2021. Electrical resistivity of FeS at high pressures and temperatures: Implications of thermal transport in the core of Ganymede. *Journal of Geophysical Research: Planets*. 126(5): e2020JE006793. DOI: 10.1029/2020JE006793

9. Berrada, M., Secco, R.A., Yong, W. and **Littleton, J.A.H.** 2020. Electrical resistivity measurements of Fe-Si with implications for the early lunar dynamo. *Journal of Geophysical Research: Planets*. 125(7): e2020JE006380. DOI: 10.1029/2020JE006380

8. Berrada, M., **Littleton, J.A.H.** and Secco, R.A. 2020. Smartphones and Gravitational Acceleration II: Applications. *The Physics Teacher*. 58(7): 473-476. DOI: 10.1119/10.0002064

7. Berrada, M., **Littleton, J.A.H.** and Secco, R.A. 2020. Smartphones and Gravitational Acceleration I: Overview. *The Physics Teacher*. 58(7): 470-472. DOI: 10.1119/10.0002063

6. **Littleton, J.A.H.**, Secco, R.A., Yong, W. and Berrada, M. 2019. Electrical resistivity and thermal conductivity of W and Re up to 5 GPa and 2300 K. *Journal of Applied Physics*. 125(13): 135901. DOI: 10.1063/1.5066103
5. Yong, W., Secco, R.A., **Littleton, J.A.H.** and Silber, R.E. 2019. The iron invariance: Implications for thermal convection in Earth's core. *Geophysical Research Letters*. 46(20): 11065-11070. DOI: 10.1029/2019GL084485
4. Silber, R.E., Secco, R.A., Yong, W. and **Littleton, J.A.H.** 2019. Heat flow in Earth's core from invariant electrical resistivity of Fe-Si on the melting boundary to 9 GPa: Do light elements matter?. *Journal of Geophysical Research: Solid Earth*. 124(6): 5521-5543. DOI: 10.1029/2019JB017375
3. **Littleton, J.A.H.** and Secco, R.A. 2018. An indoor magnetic exploration survey. *The Physics Teacher*. 56(8): 544-547. DOI: 10.1119/1.5064569
2. Silber, R.E., Secco, R.A., Yong, W. and **Littleton, J.A.H.** 2018. Electrical resistivity of liquid Fe to 12 GPa: Implications for heat flow in cores of terrestrial bodies. *Scientific Reports*. 8(1): 10758. DOI: 10.1038/s41598-018-28921-w
1. **Littleton, J.A.H.**, Secco, R.A. and Yong, W. 2018. Decreasing electrical resistivity of silver along the melting boundary up to 5 GPa. *High Pressure Research*. 38(2): 99-106. DOI: 10.1080/08957959.2018.1435786